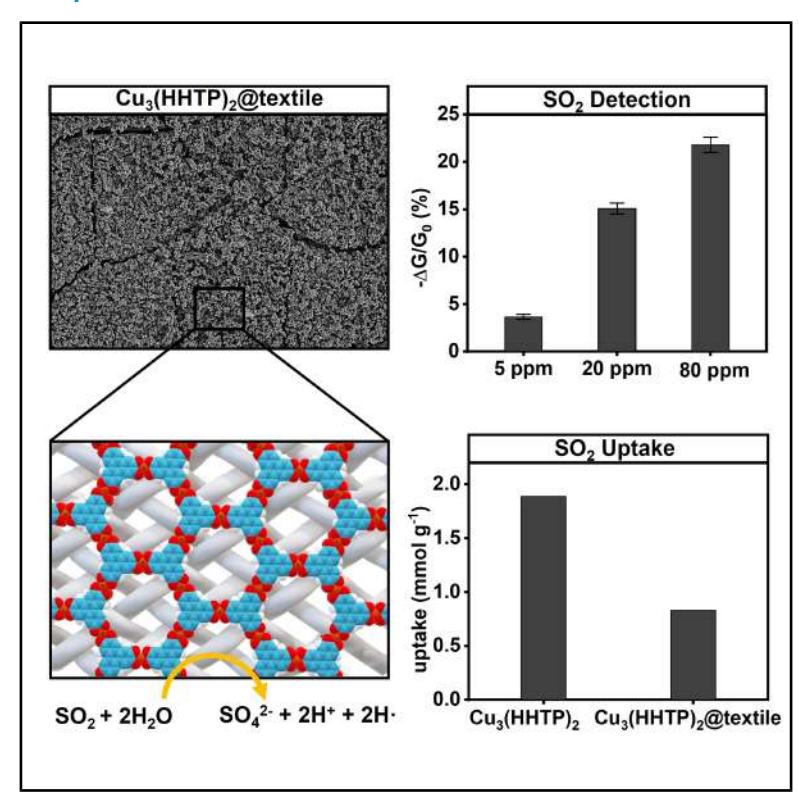
Chem

Scalable templated fabrication of Cu-based MOF on textiles for simultaneous sensing, filtration, and detoxification of SO₂

Graphical abstract



Highlights

- Scalable fabrication of MOF-based smart electronic textiles up to 100 cm² dimension
- MOF/textile devices for simultaneous sensing and filtration of SO₂
- Partial chemical conversion of SO₂ into less-toxic sulfate via redox reactions with MOF

Authors

Zhuoran Zhong, Patrick Damacet, Elí Sánchez-González, ..., Giovanni Barcaro, Ilich A. Ibarra, Katherine A. Mirica

Correspondence

giovanni.barcaro@pi.ipcf.cnr.it (G.B.), argel@unam.mx (I.A.I.), katherine.a.mirica@dartmouth.edu (K.A.M.)

In brief

We address the challenge of developing multifunctional devices for SO₂ monitoring and removal by integrating a conductive metal-organic framework (MOF), Cu₃(HHTP)₂, into textiles via a scalable templated fabrication method. The resulting MOF/textile device is the first example capable of simultaneously sensing and filtering SO₂, with sub-ppm sensing capabilities and high SO₂ adsorption capacity via partially redox reaction pathways. This work demonstrates a scalable strategy for fabricating multifunctional MOF-based textiles, offering smart material solutions for air quality monitoring and personal protection.



Zhong et al., 2025, Chem 11, 102580 October 9, 2025 © 2025 Elsevier Inc. All rights are reserved, including those for text and data mining, Al training, and similar technologies. https://doi.org/10.1016/j.chempr.2025.102580



Chem



Article

Scalable templated fabrication of Cu-based MOF on textiles for simultaneous sensing, filtration, and detoxification of SO₂

Zhuoran Zhong,¹ Patrick Damacet,¹ Elí Sánchez-González,² Aileen M. Eagleton,¹ Nataliia Vereshchuk,¹ Ravint Wongratanaphisan,¹ Jamison T. Anderson,¹ Sofia Goncalves,¹ Gregory W. Peterson,³ Brandon Blount,⁴ Susanna Monti,⁵ Giovanni Barcaro,6,* Ilich A. Ibarra,²,* and Katherine A. Mirica¹,7,*

THE BIGGER PICTURE As smart electronic textiles (e-textiles) rapidly emerge as a transformative technology in advanced functional materials, a significant gap remains in developing multifunctional devices for air quality management and monitoring. This study addresses this challenge by demonstrating the first example of simultaneous sulfur dioxide (SO₂) sensing and filtration using a copper-based hexahydroxytriphenylene (Cu₃(HHTP)₂) metal-organic framework (MOF) incorporated into polyester textiles via a scalable templated fabrication method. First, the prepared MOF/textile composites meet the Occupational Safety and Health Administration's (OSHA) permissible exposure limit (PEL) with sub-ppm sensing capabilities, while offering high SO₂ adsorption capacity and device regenerability. Second, this work provides valuable fundamental insights into the interactions between MOF and SO₂ through a combination of experimental and computational studies, revealing the pathway by which SO2 is converted into less-toxic sulfate species. This understanding will contribute to future research on MOF-based air pollutant remediation. Third, the scalable fabrication method up to 100 cm² dimension lays the groundwork for the production of largearea MOF/textile devices. The scalability enhances the potential for widespread use of MOF materials in wearable sensors and personal protective equipment (PPE), where timely detection and filtration of harmful gases are crucial. Ultimately, this research establishes the scientific basis for the integration of functional MOFs into next-generation smart textiles, with promising applications in environmental monitoring, health protection, and air remediation.

SUMMARY

This paper describes the scalable fabrication of smart electronic textiles (e-textiles) capable of simultaneous sensing, filtration, and detoxification of sulfur dioxide (SO₂). The templated method converts pre-deposited copper metal into copper hydroxide, followed by conversion into a copper-based hexahydroxytriphenylene metal-organic framework (MOF) (Cu₃(HHTP)₂), to afford a large-area ($10 \times 10 \text{ cm}^2$) conductive coating (sheet resistance = 0.1– $0.3 \text{ M}\Omega$). The resulting e-textiles achieve sensing (theoretical limit of detection [LOD] of 0.43 ppm), filtration (adsorption uptake of $1.9 \text{ and } 0.83 \text{ mmol g}^{-1}$ for MOF powder and MOF/textile, respectively, at 1 bar and 298 K), and detoxification (redox conversion of SO₂ gas into solid sulfate) due to the selective material-analyte interactions. This scalable method for generating e-textiles is a promising approach for the fabrication of smart membrane materials with multifunctional performance characteristics.

¹Department of Chemistry, Burke Laboratory, Dartmouth College, Hanover, NH 03755, USA

²Laboratorio de Fisicoquímica y Reactividad deSuperficies (LaFReS), Instituto de Investigaciones en Materiales, Universidad Nacional Autónoma de México, 04510 Ciudad de México, Mexico

³DEVCOM Chemical Biological Center, 8198 Blackhawk Road, Aberdeen Proving Ground, Aberdeen, MD 21010-5424, USA

⁴Leidos, Inc., Abingdon, MD 21009, USA

⁵CNR-ICCOM, Institute of Chemistry of Organometallic Compounds, Area della Ricerca, Pisa 56124, Italy

⁶CNR-IPCF, Institute for Chemical and Physical Processes, Area della Ricerca, Pisa 56124, Italy

⁷Lead contact

^{*}Correspondence: giovanni.barcaro@pi.ipcf.cnr.it (G.B.), argel@unam.mx (I.A.I.), katherine.a.mirica@dartmouth.edu (K.A.M.) https://doi.org/10.1016/j.chempr.2025.102580





INTRODUCTION

Air pollution is one of the most significant environmental health risks that considerably impacts the economy by causing diseases and premature deaths, while damaging ecosystems, flora, and fauna, as well as water and soil quality. Environmental safety agencies have established comprehensive guidelines and mandated strict protection of workers' health against air pollutants. However, one of the main challenges for effective protection and decontamination of toxic gases in the air is that toxic atmospheric substances, such as sulfur dioxide (SO₂), can come from various natural, industrial, and household sources, complicating emission regulations and challenging the protective equipment of the workers.³⁻⁶ As such, when unregulated or unanticipated, these gaseous pollutants are notorious for causing acute and chronic health effects in human beings, including respiratory issues, neurological diseases, and even death. Moreover, the detrimental effects of toxic air pollutants occur at extremely low concentrations (ppb to ppm levels). For instance, the legal airborne permissible exposure limit (PEL) of SO₂ is 5 ppm, averaged over an 8-h work shift, with 100 ppm being immediately dangerous to life or health (IDLH). The demanding health issues of air pollutants set a high benchmark for innovations in air quality management and personal protective equipment (PPE).8,9

Current gas monitors, sensors, analyzers, and filters are unable to meet the targets of (1) seamless integration of active sensing materials on diverse substrates, (2) simultaneous ppm-to-ppb detection and detoxification of multiple pollutants in the air, and (3) smart wearable/portable devices that are lightweight, flexible, resistant, and reusable. 10-12 At the same time, the burgeoning textile technology with metal-organic frameworks (MOFs) is foreseen as a promising direction to fabricate smart textiles and advance state-of-the-art wearable devices. 13-15 The multifaceted functions of MOFs can be achieved and tailored by controlling compositions of building units, crystal structures, topologies. pore sizes, and surface chemistry. 16,17 Moreover, the bottom-up assembly of MOFs is customizable to various substrates. 13,18 Fibers, 13,14,19-23 yarns, 24 fabrics, 18,25-29 and polymer substrates^{30,31} have been selected to fabricate MOF-based multifunctional textiles. Woven, 18,26 non-woven, 20,32 natural, 19,33-36 and synthetic^{28,37-41} fabrics including silk, cellulose cotton, viscose rayon, wood-pulp fiber, polypropylene, polyethylene terephthalate, polyester, and nylon have been employed to support MOF growth. Several methods of MOF/textile composites that have been reported in the literature include the in situ growth of MOF on the textile and the restructuring of pre-deposited metal or metal oxide-based precursors into MOFs. 13 Solvothermal 22,25 and layer-by-layer²⁹ techniques constitute established methods for in situ growth and modification to form robust MOF coatings with strong interfacial contacts on fibers and fabrics. 13 However, most solvothermal methods are only applicable to cellulosebased substrates, 42 limiting the scope of substrates employed. The layer-by-layer method usually gives rise to controlled loading of MOFs on surfaces but often limit the crystallinity and result in fragments of MOF layers.43 In contrast, restructuring of metal and/or metal oxide into a MOF allows straightforward coordination of MOFs on precoated textiles with a metal/metal oxide

thin film. ^{18,21,28,31,39} This emerging approach is beneficial for attaining uniform, robust, and conformal MOF films, but is limited by the adoption of expensive and specialized equipment with limited scalability, such as atomic layer deposition (ALD), or thermal evaporation (TE). Although some specific examples using hot-pressing, ^{44,45} electrospinning, ^{46,47} and three-dimensional (3D) printing methods showed promise in large-area and time-efficient production of MOF/textile composites, promoting scalable MOF production on textiles and making such methods accessible and compatible with existing devices requires significant advancements.

In pursuit of unlocking a smart MOF/textile device for broad personal protection covering simultaneous sensing, filtration, and detoxification of toxic gases, the scalable and efficient integration of two-dimensional (2D) conductive MOFs on textiles is a promising strategy for simultaneously realizing electronic detection 18,22,25,30 and multiple functionalities that have been reported in non-conductive MOFs, including air remediation, 32,47 chemical warfare agent decontamination, 48,49 UV protection, 29 drug delivery,²⁷ antimicrobial,³⁵ and self-cleaning⁵⁰ abilities. Beyond the intrinsic benefits of MOFs, such as the tunable pore structures, bottom-up approaches, high surface area, and tunable active sites, integrating conductive MOFs into textile matrices capitalizes on the properties of these materials for low-power, electronically transduced chemiresistive sensing, 51,52 which is difficult to achieve in non-conductive MOF/textile systems. Although strategies applying MOFs with tunable metal and ligand sites to interact with SO2 constitute an active area of research for the detection and filtration of SO₂, 5,53-58 there has been no research on simultaneous sensing and filtering of SO₂ by utilizing conductive MOFs or MOF/textile devices.

Herein, we report a scalable method for the generation of a conductive 2D MOF on commercially available textiles of large swatch sizes (Figure 1) to achieve simultaneous detection, filtration, and detoxification of SO₂. We employ a two-step templated method to convert copper (Cu) metal to Cu(OH)₂ template and subsequently to the Cu₃(HHTP)₂ (HHTP = 2,3,6,7,10,11-hexahydroxytriphenylene) MOF on polyester fabrics. The resulting electronic textiles (e-textiles), prepared with sizes up to 10 cm \times 10 cm, achieve MOF loadings of 5.05 mg per cm² and conductivities ranging from 0.033 to 0.10 S m⁻¹. The Cu₃(HHTP)₂@textile devices function as chemiresistive sensors for SO₂, exhibiting partially reversible responses to 2-100 ppm SO₂ in N₂ and air and sub-ppm theoretical limits of detection (LOD) (average LOD of 0.15 ppm in N₂ and 0.43 ppm in air). The bulk MOF powder and MOF/textile composite also demonstrate the capability to uptake and filter SO2, with an adsorption capacity of 1.9 mmol g⁻¹ for Cu₃(HHTP)₂ powder, 0.83 mmol g⁻¹ for Cu₃(HHTP)₂@textile at room temperature under 1 bar. The MOF and e-textiles also resist SO2 breakthrough with capacities of 0.62 and 0.87 mmol g⁻¹ under dry and humid conditions for the MOF, respectively, and 0.15 and 0.26 mmol g⁻¹ under dry and humid conditions for the MOF/textile composite. A rigorous spectroscopic investigation involving Raman spectroscopy, diffuse reflectance infrared Fourier transform spectroscopy (DRIFTS), attenuated total reflectance infrared spectroscopy (ATR-IR), X-ray photoelectron spectroscopy (XPS), and electron paramagnetic resonance (EPR) spectroscopy, as well as powder X-ray





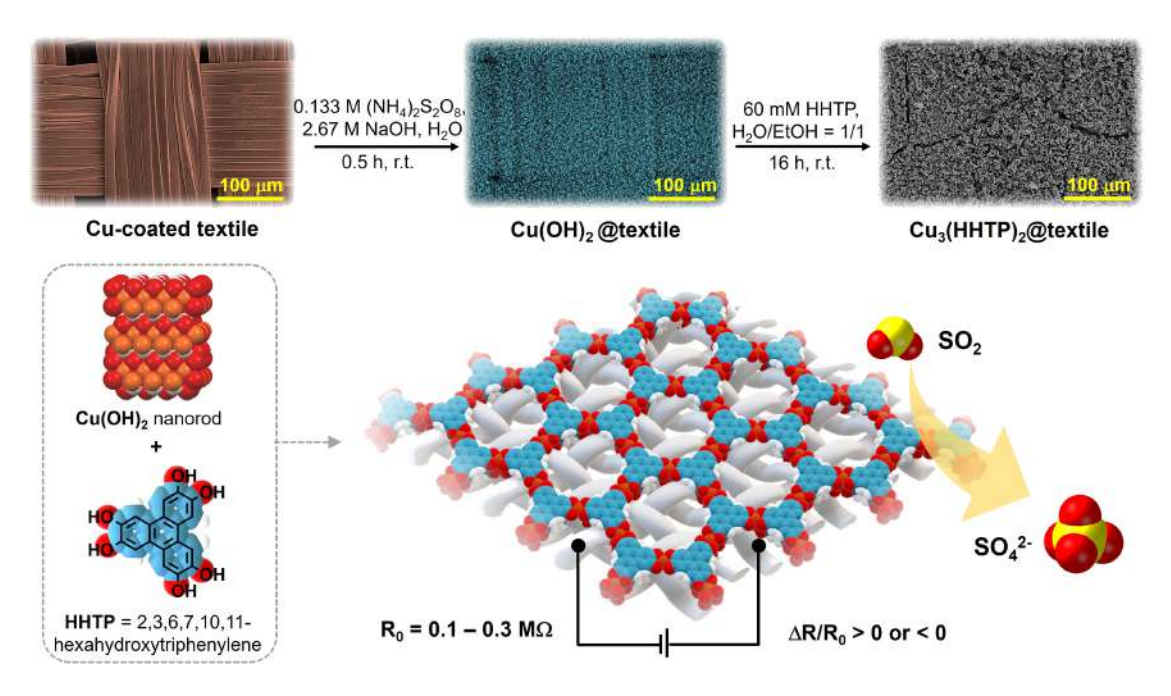


Figure 1. Preparation of $Cu_3(HHTP)_2$ @textile using the two-step templated method for simultaneous sensing, filtration, and detoxification of SO_2

diffraction (PXRD) measurements reveal that the interaction between SO_2 and $Cu_3(HHTP)_2$ involves the formation of sulfate species accompanied by the partial reduction of Cu(II) into Cu(I) in the MOF/textile composite. Hierarchical atomistic multi-scale reactive molecular dynamics (RMD) simulations and quantum chemistry (QC) calculations illustrate the structural and dynamical features of the MOF on textiles, and disclose interaction and reactive scenarios of the $SO_2/H_2O/Cu_3(HHTP)_2$ system, using model sizes at different scale lengths that facilitate comparison with the experimental characterization. Taken together, our studies highlight a novel scalable methodology for e-textile fabrication, unprecedented performance for simultaneous SO_2 sensing, filtration, and detoxification, and new fundamental insights into material-analyte interactions for guiding future design of multifunctional materials.

RESULTS AND DISCUSSION

Device synthesis and characterization

Scalable MOF/textile composites were prepared using the two-step templated method by converting commercially available Cu coating on woven polyester swatches into $\text{Cu}(\text{OH})_2$ template $(\text{Cu}(\text{OH})_2\text{@textile})$ and subsequently into $\text{Cu}_3(\text{HHTP})_2$ MOF on the textile $(\text{Cu}_3(\text{HHTP})_2\text{@textile})$, as illustrated in Figures 1 and S1.

The characteristic PXRD peaks corresponding to $\text{Cu}(\text{OH})_2$ and $\text{Cu}_3(\text{HHTP})_2$ proved the successful integration of these materials onto textiles (Figure 2A). To ensure complete conversion in the two-step templated method, we optimized the effect of reaction time and concentrations of reagents in the stepwise transformation (Figures S2–S4). According to PXRD results, a nearly complete conversion of Cu to $\text{Cu}(\text{OH})_2$ on 1.5 cm \times 1.5 cm textile swatches was achieved with a reaction duration of 0.5 h, using

10 mL of 2.67 M NaOH and 0.133 M (NH₄)₂S₂O₈ stock solution following a reported method (Figure S2). The optimized conditions to reach full conversion from Cu(OH)₂ to Cu₃(HHTP)₂ involve using a 60 mM HHTP (0.090 mmol) solution in 1.5 mL H₂O/EtOH (1:1 v/v) co-solvent for 1.5 cm \times 1.5 cm textile swatches, with a reaction time of 20 h in ambient air (Figures S3 andS4). Scanning electron microscopy (SEM) and energy dispersive X-ray spectroscopy (EDX) analyses of Cu (OH)₂@textile showed fine nanowire morphology (Figures 2B, S5, and S6), while Cu₃(HHTP)₂@textile formed spherical clusters of rod-like crystals (Figures 2B, S7, and S8), with a thickness of Cu₃(HHTP)₂ layer of around 7 μ m (Figure S9).

We assessed the yield of the transformation by measuring the concentration of copper cation (Cu²⁺) and calculating the yield and weight percent of products in each step (Figure S10; Table S1). A yield of 45% ± 4% for the first step and a yield of $59\% \pm 3\%$ for the second reaction were found. Additionally, the weight percentage of Cu-containing species on textiles was calculated based on the inductively coupled plasma mass spectrometry (ICP-MS) result, giving 33 ± 1 wt % Cu metal in the original Cucoated textile, 22 \pm 2 wt % Cu(OH)2 in Cu(OH)2@textile, and 38 \pm 3 wt % Cu₃(HHTP)₂ in Cu₃(HHTP)₂@textile (Table S1). Tracking the transformation of Cu(OH)2 to Cu(HHTP)2 by PXRD, 2-point probe, and mass change of the e-textile over time revealed the initial formation of copper(I) oxide (Cu₂O) during the first 2-12 h of the reaction, which was subsequently consumed to form Cu₃(HHTP)₂ (Figure S11). We reasoned that Cu(OH)₂ was reduced to Cu₂O by HHTP ligand in the absence of sufficient O₂ diffused from air into the reaction medium at the early stage of the reaction. 60 By measuring the mass change of textiles throughout the reaction, we determined the mass of Cu₃(HHTP)₂ per surface area over time, which increased rapidly until the appearance of Cu₂O



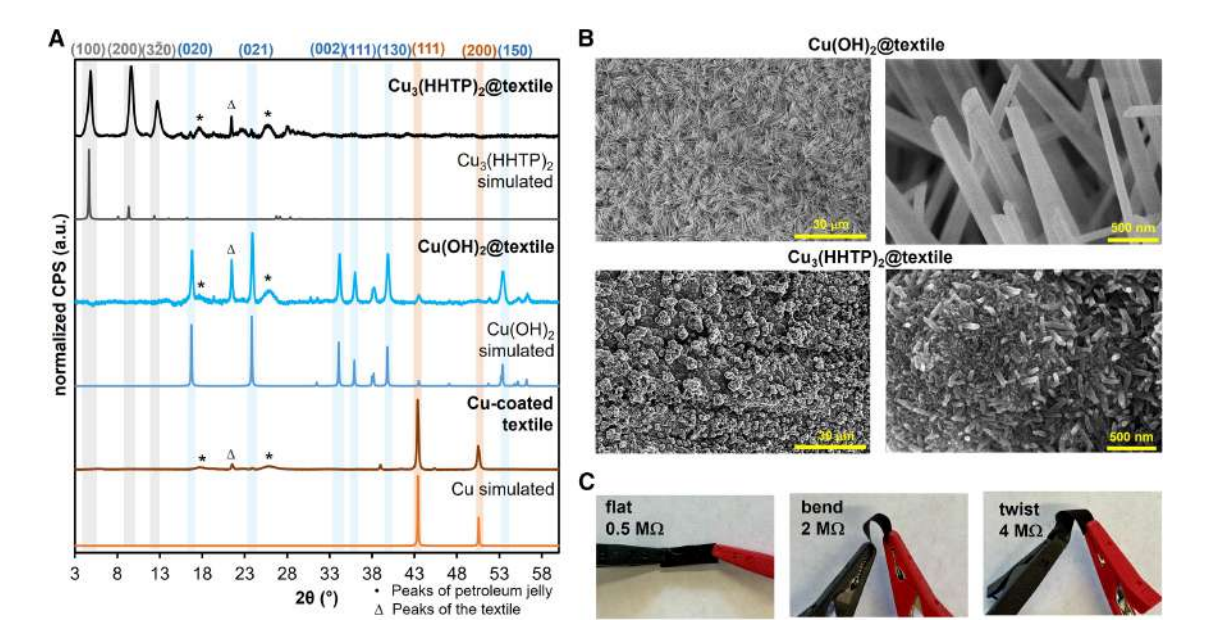


Figure 2. Characterizations of the MOF/textile composites

(A) PXRD spectra of Cu(OH)₂@textile and Cu₃(HHTP)₂@textile. Gray shading highlights characteristics Cu₃(HHTP)₂ diffraction peaks, blue shading shows Cu(OH)₂ diffraction peaks, and orange shading shows Cu diffraction peaks. The star symbol marks the diffraction peaks of petroleum jelly used for immobilizing the textile swatches on the PXRD sample holder, and the triangle symbol marks the diffraction peaks of the polyester fabric.

(B) Representative SEM images of Cu(OH)₂@textile and Cu₃(HHTP)₂@textile.

(C) Resistance of $Cu_3(HHTP)_2$ @textile as flattened out, bent, and twisted. The dimensions of the textile devices are 1.5 cm \times 0.5 cm.

intermediate, then increased slowly to reach the maximum mass per area of 5.05~mg MOF per cm 2 in 48 h (Figure S12; Table S2). The sheet resistance of the textile swatches ($1.5~\text{cm} \times 1.5~\text{cm}$) during the transformation showed a good correlation with the progress of the reaction (Figure S12; Table S3).

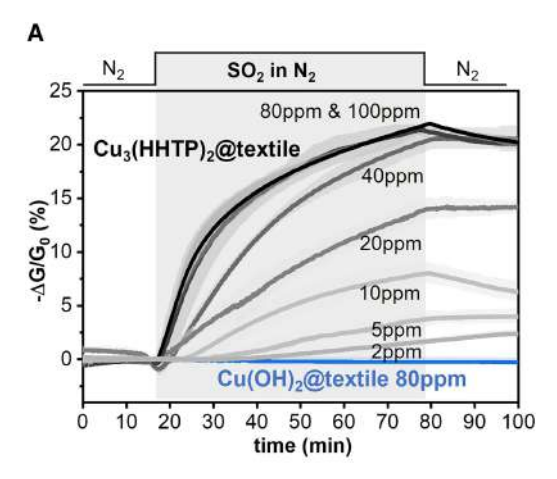
The integrated MOF/textile devices exhibited good stability against mechanical manipulation, maintaining resistance upon physical stresses such as twisting or bending (Figure 2C). Furthermore, a Scotch tape test revealed moderate adhesion of Cu₃(HHTP)₂ onto the textile devices. Cu₃(HHTP)₂@textile devices lost 9.6% ± 3.2% of their initial mass upon the tape test, while Cu(OH)2@textiles and Cu-coated textiles exhibited remarkably lower mass losses of 3.0% \pm 0.7% and 1.5% \pm 0.9%, respectively (Figures S13 and S14). These results indicate that the pristine Cucoated textile has robust chemical adhesion between Cu coating and the polyester swatch, as the textile is fabricated through electroless plating of copper via a heterogeneous oxidation-reduction reaction at the solid-liquid interface. ⁶¹ However, the bonding of the semiconductor coatings on the polyester substrate weakened during the two-step templated synthesis from Cu to Cu(OH)2 and Cu₃(HHTP)₂ as evidenced by the increased mass loss percentages in the tape test. Specifically, we hypothesize that the interactions between the Cu₃(HHTP)₂ MOF and polyester include hydrogen-bonding, van der Waals, and dipole-dipole interactions. Brunauer-Emmett-Teller (BET) surface area analysis using N₂ at 77 K showed that the surface area of the Cu-coated textile of 0.23 m²/g increased to 6.70 and 10.10 m²/g for Cu(OH)₂@textile and Cu₃(HHTP)₂@textile, respectively (Figure S15). These results demonstrate that the assembly of porous MOFs on textiles enhances the surface area and adsorption capacity of the textile devices. Thermal gravimetric analysis (TGA) measurements confirmed a small amount of aqua ligands (8 wt %) bound to the MOF/textile after drying (Figure S16). We also note that the preparation of Cu₃(HHTP)₂ from Cu(OH)₂ is not limited to textile substrates and can be achieved with bulk Cu(OH)₂ using a similar solvothermal method (Figures S17–S19).

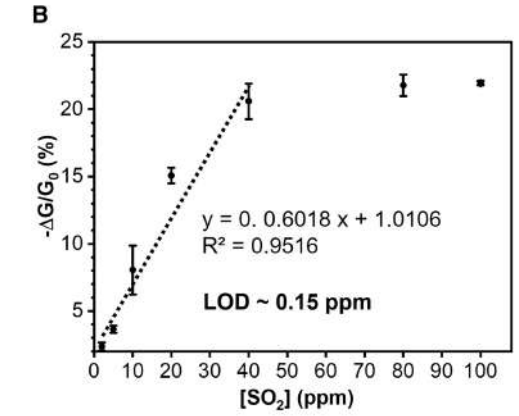
Chemiresistive sensing

Cu₃(HHTP)₂@textile showed excellent chemiresistive sensing performances, low LOD, and efficient adsorption uptake of SO₂. Cu₃(HHTP)₂@textile devices showed a concentrationdependent increase in chemiresistive response in the range of 2 to 80 ppm SO₂ in dry N₂ (Figure 3A). At SO₂ concentrations of 80 ppm and above, the e-textile sensors exhibited saturation. Notably, the response of the e-textile to 5 ppm SO₂ satisfies the PEL by the OSHA. Overall, the increase in resistance was attributed to the reduced concentrations of the charge carriers within the p-type Cu₃(HHTP)₂ semiconductor. ^{18,30,43,62} Cu (OH)2@textile and Cu-coated textile failed to exhibit any detectable responses toward SO₂, suggesting that only the MOF served as the SO₂ sensing material at the examined concentrations on textiles (Figures S20 and S21). In the three-cycle dosing experiments, the sensing responses of Cu₃(HHTP)₂@textile diminished after repeated cycling, suggesting a partially reversible material-analyte interaction responsible for the dosimetric nature of the response. Based on the linear normalized response $(-\Delta G/G_0)$ over the analyte concentration range of 2-40 ppm (Figure 3B), the theoretical LOD of Cu₃(HHTP)₂@textile toward SO₂ was determined to be 0.43 ppm (Table S4; Figure S22). Bulk Cu₃(HHTP)₂ powder drop-casted on the interdigitated









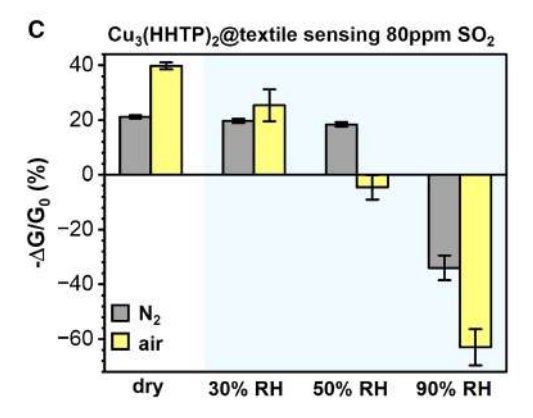


Figure 3. Chemiresistive sensing of $\text{Cu}_3(\text{HHTP})_2@\text{textile}$ devices

(A) The sensing responses of $Cu_3(HHTP)_2$ @textile devices with 2, 5, 10, 20, 40, 80, and 100 ppm SO_2 in N_2 atmosphere compared with the invisible sensing response of $Cu(OH)_2$ @textile. The time period includes a baseline in the delivery gas at a flow rate of 0.5 L/min before analyte exposure (1,000 s) and exposure to target gas mixed with the delivery gas (60 min), which was then followed by device recovery in the delivery gas at a flow rate of 0.5 L/min.

(B) Linear range of maximum change in normalized conductance ($-\Delta G/G_0$) versus SO $_2$ concentration (5–100 ppm) for Cu $_3$ (HHTP) $_2$ @textile devices in N $_2$ atmosphere.

(C) Representative sensing responses of $Cu_3(HHTP)_2$ @textile devices with 80 ppm SO_2 in N_2 , air, humid N_2 (RH = 30%, 50%, and 90%), and humid air (RH = 30%, 50%, and 90%) atmospheres. The gray bars represent SO_2

gold electrode exhibited a similar response magnitude toward 80 ppm SO_2 as the MOF/textile composite, while $Cu(OH)_2$ deposited on interdigitated electrodes showed no sensing response toward SO_2 , confirming that the MOF material plays the dominant role in SO_2 detection (Figure S23).

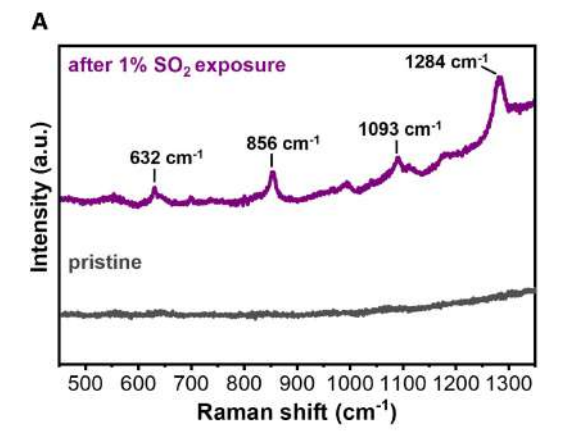
The exposure of Cu₃(HHTP)₂@textile to 80 ppm SO₂ in air generated a higher response of 41% than the response of 23% in N₂ (Figures 3C and S20H). The response also showed a linear dependence on concentrations at 5-80 ppm, leading to a theoretical LOD down to 0.89 ppm (Figures S24-S26; Table S5). We observed good selectivity for SO₂ over CO₂, with no response for Cu₃(HHTP)₂@textile devices under 400 ppm CO₂ (Figure S27). On the other hand, the detection of SO₂ in humid N₂ and air (40,000 ppm H₂O, relative humidity [RH] = 90%, gas temperature = 30°C) demonstrated negative sensing-response changes, where the normalized responses for the first cycle were -38% and -67% in humid N_2 and air (Figures S20I and S20J). As $Cu_3(HHTP)_2$ exhibits p-type behavior with SO₂ in dry N₂ and air, ^{20,22,31} the opposite sensing responses observed in humid N₂ and air suggest that the co-presence of H₂O and SO₂ alters the charge transfer process in Cu₃(HHTP)₂@textile significantly. A non-linear sensing-response trend was also observed for SO2 concentrations ranging from 2-80 ppm in humid N_2 (RH = 90%) (Figures S28 and S29), suggesting a change in the sensing mechanism of the composite toward SO₂ under elevated humid conditions. To deconvolute the sensing behavior of Cu₃(HHTP)₂@textile with SO₂-H₂O mixture, we performed sensing experiments with 40,000 ppm H₂O vapor (RH = 90%) in the absence of SO2 under both N2 and air atmospheres (Figure S30). We observed negative sensingresponse changes of -330% and -50% in N_2 and air, respectively. The increased conductivity of Cu₃(HHTP)₂ under exposure to H₂O vapor suggests that H₂O promotes favorable charge transfer within the MOF.⁶³ Our results also indicate that when SO₂ and H₂O coexist, H₂O plays a dominant role in chemiresistive sensing, leading to increased conductivity and the opposite sensing response of the MOF/textile in SO₂-H₂O systems.

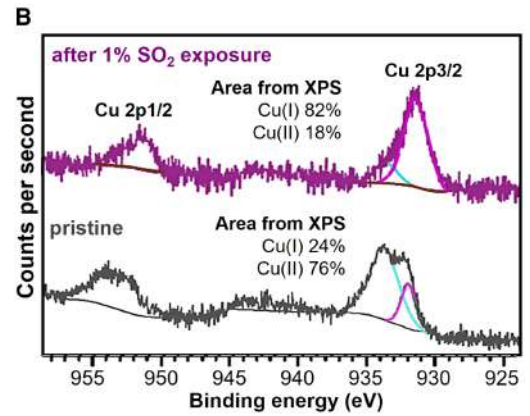
To further evaluate the SO_2 -sensing performance of the e-textile under varying humidity levels, we tested $Cu_3(HHTP)_2$ @textile at a constant SO_2 concentration in N_2 and air with humidity levels ranging from 0% to 90% (Figures 3C and S31–S34). The chemiresistive responses to 80 ppm SO_2 were found to be 19%–22% under 0%–50% N_2 humidity and 25%–40% under 0%–30% air humidity. Since the responses turned negative approaching 90% humidity levels, we modified the surface of $Cu_3(HHTP)_2$ @textile with hydrophobic properties to improve the sensing capability under higher humidity levels, (Figures S35–S38). After low-pressure vapor phase deposition of fluoroalkyl silane, the modified e-textile (termed $Cu_3(HHTP)_2$ @textile-F) turned hydrophobic, with a water surface contact angle of 131° (Figure S39). $Cu_3(HHTP)_2$ @textile-F retained reliable chemiresistive sensing

sensing responses in N_2 , and the yellow bars represent SO_2 sensing responses in air.

Error bars represent the standard deviations from the mean based on 3-4 replicates.







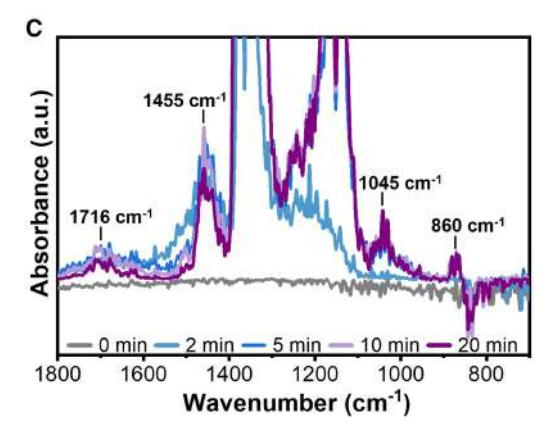


Figure 4. Spectroscopic investigation of material-analyte interactions (A) Raman spectroscopic investigation on Cu₃(HHTP)₂@textile before and after 1% SO₂ in N₂ for 0.5 h.

(B) XPS analysis on Cu 2p region for $Cu_3(HHTP)_2$ @textile before and after 1% SO_2 in N_2 for 0.5 h.

(C) DRIFTS plotted as difference spectra on Cu₃(HHTP)₂ powder exposed to 1% SO₂ in N₂ at different time intervals of exposure.

performances in high humidity levels, exhibiting response changes of 8%–21% under 0%–90% N_2 humidity and 35%–53% under 0%–50% air humidity (Figures S40–S43). Taken together, we conducted the first systematic investigation of $Cu_3(HHTP)_2$ @textile sensing toxic gas in diverse humid environments, highlighting its potential applicability in real-world conditions.

The regenerability of the Cu₃(HHTP)₂@textile sensors was assessed through washing or heating treatments of the textile devices following a 1-h exposure of 80 ppm SO₂ (Figure S44A). After immersing in water for 1 h, the e-textiles retained 77% of the initial sensing response for 80 ppm SO₂ (Figures S44B and S45A-S45C). 55% of the sensing response maintained after heating at 70°C for 1 h (Figures S44D and S45D-S45F). In contrast, only 26% of the sensing response remained after purging with N₂ for 1 h (Figures S44C and S20F). The resistances of the textile devices also recovered to 1–2.5 $M\Omega$ after consecutive treatments of SO₂ and washing/heating (Figure S45E). PXRD results of the e-textile after sensing and washing/heating treatments showed two new diffraction peaks at 36° and 42° 2θ corresponding to the formation of Cu₂O. MOF crystallinity decreased partially after the recovery processes because of the decreased (100) diffraction peak intensity (Figure S44F).

Spectroscopic investigation of the mechanism

Spectroscopic investigations on the mechanism of MOF-SO₂ interactions were conducted on Cu₃(HHTP)₂@textile and Cu₃(HHTP)₂ powder. After dosing with 1% SO₂ in N₂ for 0.5 h, Cu₃(HHTP)₂@textile showed characteristic Raman bands at 1,284, 1,093, and 632 cm⁻¹, corresponding to the asymmetric stretch (ν 3), symmetric stretch (ν 1), and asymmetric bend (ν 4) of the solid-state sulfate (Figure 4A). 64,65 While similar results were attained for bulk Cu₃(HHTP)₂ powder, Cu(OH)₂@textile did not exhibit any Raman bands, consistent with the sensing experiment with Cu(OH)₂@textile that no response was observed (Figure S46). The adsorption of S-containing species onto Cu₃(HHTP)₂@textile was further confirmed by EDX-SEM, which showed an increase in the S element ratio from 0 to 1.1 wt % after SO₂ dosing (Figure S47). XPS spectra of Cu₃(HHTP)₂@textile before and after exposure to 1% SO2 in N2 for 0.5 h further confirmed both the adsorption and oxidation of SO₂, apparent by the emergence of a new S 2p emission band at 168.9 eV corresponding to S-O of sulfate, while no S 2p peaks were observed in the pristine sample (Figures S48 and S49). Moreover, after deconvolution of the Cu 2p3/2 emission lines, a redox transition of Cu-metal ions in the MOF was found as the Cu(I) peak area increased from 24% to 82% after interacting with SO₂ (Figure 4B). The redox transformation from Cu(II) to Cu(I) was also confirmed through PXRD analysis, where we observed the emergence of two diffraction peaks at 36° and 42° 2θ corresponding to the formation of Cu₂O (Figure S50). The (100) diffraction peak intensity of Cu₃(HHTP)₂ dropped while (200) and (320) peaks did not change as shown in Figure S50A, indicating a partial loss of MOF crystallinity on the textile. The increased resistance from 0.2–0.5 to 1–5 $M\Omega$ can be attributed to cumulative effects of the redox transition from Cu(II) to Cu(I), the formation of sulfate and proton species, and the change of MOF crystallinity as shown in PXRD and SEM after sensing 80 ppm SO₂ (Figures S51 and S52). No changes in PXRD or resistance change was observed in Cu(OH)₂@textile device before and after SO₂ exposure.

By exposing Cu₃(HHTP)₂ powder to 1% SO₂ in the DRIFTS experiment, we monitored the DRIFTS difference spectra over exposure time and found five spectra features (Figure 4C). First, the background absorbance decreased across a broad range





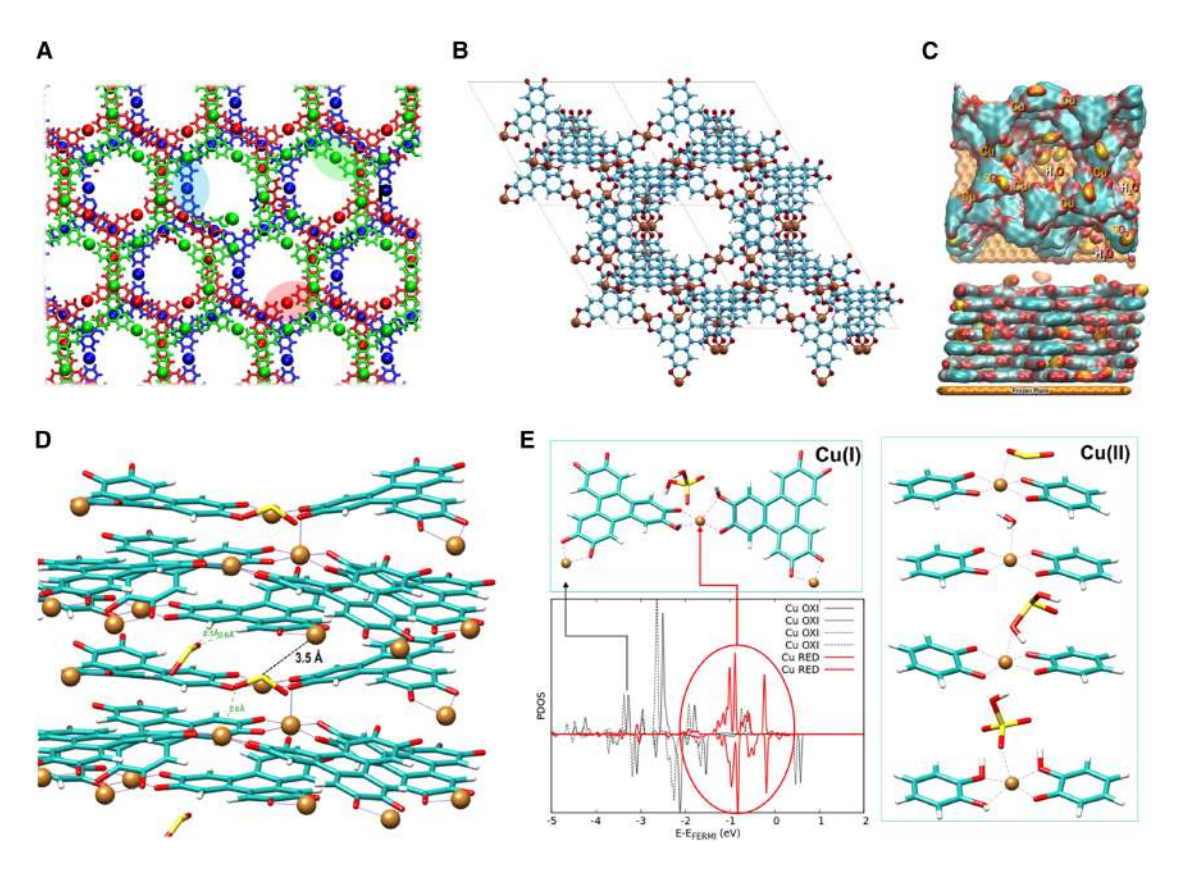


Figure 5. Theoretical calculations and simulations on material-analyte interactions

(A) RMD structural model derived by using a 7L-(12 \times 12) bulk unit cell.

(B) DFT-relaxed structure of a 4L-(1 \times 1) ABCB stacking sequence coherent.

(C) 7L-(12 \times 12) slab unit cell filled with SO_2 and water molecules.

(D) DFT-relaxed structure of a 4L-(1 × 1) ABCB stacking sequence containing 2 SO₂ molecules interacting with the CuO₄ open-metal centers and with the MOF walls.

(E) Products of the reaction of SO₂ and water with the CuO₄ open-metal sites; PDOS corresponding to the reduction from Cu(II) to Cu(I). Color coding: Cu, orange; O, red; C, cyan; S, yellow; and H, white.

of 4,000–500 cm⁻¹, which is consistent with our previous observation of Cu₃(HHTP)₂ upon exposure to H₂S.¹⁸ Second, a set of strong absorbance bands in 1,330-1,360 cm⁻¹ appeared immediately after the exposure of SO₂ and disappeared after purging with N₂ to remove the unabsorbed SO₂. These bands in 1,330-1,360 cm⁻¹ were assigned to the asymmetric stretching mode of SO₂, which was also observed in the ATR-IR measurements (Figure S53).66,67 Third, two absorbance bands at 1,716 and 1,455 cm⁻¹ were observed and assigned to the stretching and vibration of C=O and C=C in HHTP, indicating that the stretching and vibrational modes of the HHTP ligand were strengthened upon the interaction of SO₂. 18,68 Fourth, two absorbance bands at 1,045 and 860 cm⁻¹ coincide with the Raman spectroscopic observations as shown in Figures 4A and S46, corresponding to the symmetric stretch (ν 1) of the solid-state sulfate and the O-H bending of hydrated sulfate due to the aqua ligand in Cu₃(HHTP)₂ respectively.⁶⁴ EPR spectroscopy of the Cu₃(HHTP)₂ powder before and after SO₂ dosing revealed a similar absorbance band. The g-value remained constant at 2.135 since the unpaired electron primarily resulted from Cu²⁺ (Figure S54).

Computational investigation of the mechanism

Theoretical models efficiently reproduced the structural and electronic properties of the Cu₃(HHTP)₂ system in its "Eclipsed Model" (Figures S55-S58; Table S6). As confirmed by the RMD simulations based on the 7L-(12 \times 12) bulk unit cell and an initial fully eclipsed stacking pattern (Figure S56), the new arrangements limited the long-range order along the c-direction. 62,69,70 The comparison of the calculated XRD spectra of the starting and final configurations in Figure S57 showed a widening of the XRD peaks (blue lines), suggesting that the original order was not maintained, as all the layers reorganized their arrangements in response to thermal perturbations and intermolecular interactions with the guest species. The structural changes included concerted translations and rotations of their combinations that led to different pattern types. The calculated XRD pattern was further confirmed by the experimental PXRD of Cu₃(HHTP)₂@textile and the literature.

Interestingly, from a detailed analysis of the most stable RMD structure emerged the presence of peculiar motifs (Figure 5A), where the individual layers were organized in ABC stacking sequences analogous to those of face-centered cubic (fcc) crystals





(Figures S60 and S61). In such structures, even though a longrange sequence ordering could not be found, two eclipsed neighboring planes did not appear. Specifically, the proposed stacking sequence identified as an ABC motif is related to the computational reduced model that we have created to simulate the capturing mechanism of the guest molecules and to give an idea of the various stacking/shifted "planes" that can be adopted by these types of composite materials. We first extended the system size as much as possible, then "constrained" the MOF configuration by adsorbing it on a flat surface (frozen at the initial geometry) to simulate its adhesion onto a textile. Thus, the theoretical supramolecular model is biased by the geometry of the support. The sequence of layer arrangements is not ideally geometrically replicated but slightly distorted, shifted, and undulated. These reconstructions had several areas with exposed CuO₄ units (open-metal sites), which were more accessible for guest species adsorption/interactions. The examination of this new pattern at the density functional theory (DFT) level (Figures 5B and S59) and the direct comparison of the stability of the structure with the previously identified slipped-parallel arrangement suggested a coexistence of the two morphologies. The scenario of the MOF dynamics confirms a high flexibility of the structure along the direction perpendicular to its planes due to a curved and sinuous surface of the woven polyester textile in reality. We reason that the in situ assembly of MOF on the uneven textile surface caused the MOF to adapt to the curves and contours of the substrate. Due to this complexity, it is quite challenging to determine the exact stacking pattern of the MOF

As the experimental TGA results suggested the presence of residual moisture inside the material even after drying (Figure S16), we tried to estimate the potential water content by simulating the dynamics of the drying process using the 7L-(12 \times 12) slab unit cell. The RMD indicated that after drying (water evaporation), only 20% of the initial molecules remained in the material. When SO₂ was included, its content became dominant. Radial distributions of the final structures (Figures S62-S64) helped identify the relative positions of the copper ions and the other species. In the case of copper, all the plots of the empty and solvated bulk materials showed a high sharp peak at about 5.7 Å and lower, broader peaks at about 7.3 ± 0.4 Å, suggesting that water molecules do not significantly perturb the metal centers and the surrounding species. The minimal effect of water is also confirmed by the trend of the Cu-Cu radial distribution function (RDF) of the water-solvated MOF slab, which displays similar peaks. Instead, the Cu-Cu RDFs of the MOF filled with SO₂ only showed one high broader peak at approximately 6.8 Å, suggesting that these molecules could interact directly or indirectly with the metal sites and induce different relocations. The coordination linkages between HHTP ligands and Cu-metal centers were stable since no replacements were observed during the dynamics. Based on the molecular surface representations (Figures S65 and S66), the guest species remained close to the walls of the channels (Figure 5C).

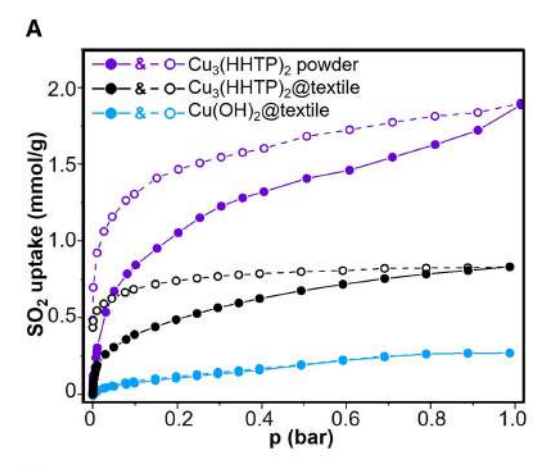
To assess the extent of agreement between RMD and QC predictions in describing the sensing properties, we performed DFT and second-order Møller-Plesset perturbation theory (MP2) local optimizations of water and SO₂ molecules interacting with the

channel walls and open-metal sites considering reduced models. For the interaction with the channel walls, we selected the preferred slipped-parallel structure (2L-[1 × 1] Translated #1, Figure S59A) and investigated the interaction of water and SO₂ separately via periodic local DFT optimizations. We singled out several configurations with similar total energy, indicating different coexisting arrangements governed by van der Waals and hydrogen-bonding interactions. Notably, SO₂ exhibited a slightly stronger affinity with the channel walls compared with water (Figure S67). When both SO₂ and H₂O are present in the framework, even at low concentrations, they can interact favorably, resulting in a flat potential energy surface. This process is accompanied by the migration of two hydrogens and a proton to the adjacent oxygens within the MOF structure, where SO₂ is oxidized by two water molecules, producing a charged HSO₄⁻ as the final product (Figure S68A). The rate determining step (RDS) of the reaction with an estimated energy barrier of 1.4 eV corresponds to the adsorption of the first water on SO₂ to form H₂SO₃. The formation of -OH groups bound to Cu changed the electronic structure of the MOF, leading to a reduction in the energy of the Cu 3d minority spin band and the formation of reduced Cu(I) species, as shown by the shift toward a lower energy (Figure S68B). A possible configuration of the interaction of guest species with open-metal sites is shown in Figure 5D. The DFT-relaxed structure extracted from RMD revealed that two SO₂ molecules interact with the neighborhood of uncovered CuO₄ units in the MOF. Consistent with RMD predictions, the typical distances between S and Cu atoms range from 3.0 to 3.5 Å, with SO₂ preferentially approaching Cu via its oxygens at distances of 2.6-2.7 Å. Similarly, as observed in the interaction with MOF walls, there is a preferential interaction between O_{SO2} and H_{MOF} at typical distances of 2.4–2.5 Å.

Further characterizations of the MOF/guest interactions and charge states of the Cu-metal center were conducted by local optimizations at the MP2 level of reduced models. We focused on the main species and intermediates interacting with the exposed CuO₄ units resulting from the MOF reconstruction. As shown in Figure 5E, SO₂ interacts with Cu(II) via one oxygen atom at elongated distances of 2.6-2.7 Å; H₂O is adsorbed on Cu(II) via its oxygen atom at distances of 2.3-2.4 Å, consistent with the previously reported results of computational investigations on hydrated Cu₃(HHTP)₂. ⁷² Reaction pathways via the addition of two H₂O molecules can lead to the formation of H₂SO₄/ HSO₄⁻ species. In the final configuration, HSO₄⁻ was stabilized on a Cu(II) center, and in an alternative configuration, H₂SO₄ interacted with a reduced Cu(I) center. The coordination of Cu decreased from four to two due to a local reconstruction of the metal oxide center. We also stabilized the configuration at the DFT level using a Cu₃(HHTP)₂ isolated layer and analyzed the contribution of the Cu atoms to the total density of states (DOS) (Figure 5E). The projected DOS (PDOS) reveals two typical features of oxidized Cu atoms (black lines) and the contribution of the reconstructed Cu atom (red line), which indicates a formal +1 oxidation state due to nearly canceled local spin polarization, consistent with a 3d10 electronic configuration. The PDOS not only demonstrates the structure of the Cu(I) complex but shows that a variation in the relative quantities of Cu(II)/Cu(I) species can significantly alter the conductive properties of the MOF. 63









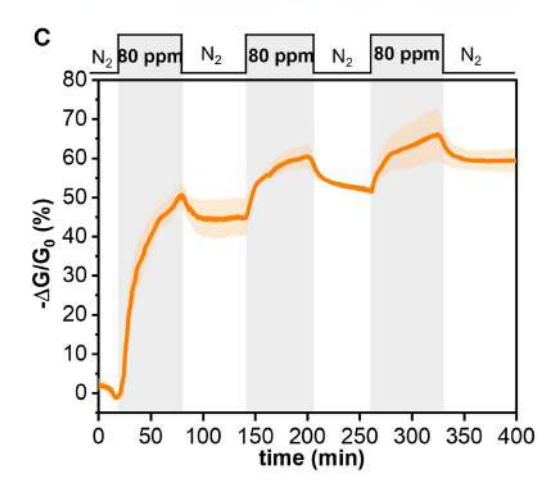


Figure 6. Adsorption performance of the MOF/textile device and a demonstration of the MOF/textile PPE

(A) SO_2 adsorption isotherms of $Cu_3(HHTP)_2$ powder (purple trace), $Cu_3(HHTP)_2$ @textile (black trace), and $Cu(OH)_2$ @textile (blue trace) at 298 K. (B) Photographic illustration of a smart MOF-mask PPE.

(C) Cyclic sensing responses of the MOF-mask when exposed to 80 ppm \mbox{SO}_2 in \mbox{N}_2 atmosphere.

Filtration and prototype demonstration

To investigate the filtration properties of the MOF/textile device, we carried out SO₂ adsorption-desorption isotherms for

 $Cu_3(HHTP)_2$ @textile, $Cu_3(HHTP)_2$ powder, and $Cu(OH)_2$ @textile, as depicted in Figure 6A and Table S7. The total SO₂ capture of 1.9 mmol g⁻¹ exhibited by the bulk MOF powder is characterized by a type 1 isotherm and is comparable to that of MOF materials with relatively similar BET surface areas. 73 The SO₂ desorption process was found not to be fully reversible, as evidenced by the relatively strong hysteresis, which confirmed a strong interaction and redox reaction between SO2 and the MOF.⁷⁴ The irreversibility of this desorption process is consistent with the partial chemisorption of SO₂ on Cu₃(HHTP)₂@textile observed spectroscopically (Figure S53). The SO2 isotherm corresponding to the activated sample of Cu₃(HHTP)₂@textile exhibited a similar behavior to Cu₃(HHTP)₂ powder, reaching a total uptake of 0.8 mmol g⁻¹. The strong hysteresis of Cu₃(HHTP)₂@textile upon desorption of SO₂ supported the presence of the chemisorptive interactions. The lower SO₂ uptake by the Cu₃(HHTP)₂@textile compared with the powder sample is rationalized by the fact that the MOF constitutes only 38% ± 3% by mass of the MOF/textile composite (Table S1). Indeed, the uptake values for the powdered MOF and the textile composite are of a comparable magnitude when taking into consideration the loading percentage of Cu₃(HHTP)₂ on the textile, suggesting that the deposition methodology of Cu₃(HHTP)₂ on the textile is efficient and does not affect the MOF uptake capacity. Six-cycle SO₂ adsorption experiments demonstrated a partial loss in the uptake capacity of Cu₃(HHTP)₂@textile after the first exposure, which was subsequently retained in the following exposures (Figures S69 and S70; Table S8). The uptake reached 0.83 mmol g⁻¹ in the first adsorption cycle at 1 bar, then decreased and stabilized at approximately 0.27 mmol g⁻¹ in subsequent cycles. This result can be attributed to the partial loss of MOF crystallinity and the combined physisorption and chemisorption of SO₂, where physisorbed SO₂ can be removed from the MOF through thermal activation in each cycle. This observation is also consistent with the trend in chemiresistive responses toward SO₂ during the three-cycle sensing experiments (Figure S20), showing diminished response after the first exposure. In the control experiment, Cu(OH)2@textile showed minimal SO₂ uptake of 0.2 mmol g⁻¹.

Additional kinetic experiments were carried out on the Cu₃(HHTP)₂@textile sample at 100 and 1,000 ppm SO₂ (Figure S71A). The kinetic profiles followed a zero-order reaction (Figure S72), consistent with the experimental condition that SO₂ concentration was fixed in the kinetic studies. We also observed that the kinetic constants decreased from 0.019 to 0.0029 h⁻¹ under 100 ppm SO_2 and from 0.027 to 0.0035 h^{-1} (Table S9) and then reached a pseudo-steady state where the SO₂ uptake ratio remained steady (Figure S71B). Based on SO₂ uptake kinetics, achieving a safe SO2 level through adsorption is estimated to require 13.3 days under 100 ppm SO₂ exposure and 8.8 days under 1,000 ppm SO₂ exposure. Two key factors should be considered here: (1) the PEL of 5 ppm, and (2) the use of a fixed SO₂ partial pressure in these kinetic experiments instead of gas flow. Besides, based on the initial adsorption rate, the time to reach an uptake of 0.028 mmol g⁻¹ (equivalent to 95 ppm) was estimated to be 1.5 h while the time to reach an uptake of 0.070 mmol g⁻¹ (equivalent to 995 ppm) was calculated as 5.28 min (0.088 h). Notably, the time required to absorb





SO₂ and reach 5 ppm is 17 times shorter when the initial concentration is 1,000 ppm compared with the initial 100 ppm SO₂ condition. This is due to the higher probability of SO₂ molecules being adsorbed at higher concentrations under the fixed SO₂ partial pressure. It is also important to note that these times represent the duration required to absorb the amounts of SO₂ equivalent to 95 and 995 ppm for 1 g of Cu₃(HHTP)₂@textile via diffusion alone. In dynamic conditions, such as during inhalation and exhalation, these times are expected to decrease significantly with gas flow.

SO₂-filtration abilities of the MOF/textile device were quantified by micro-breakthrough experiments under dry and humid (RH = 80%) dynamic air (Table S10; Figure S74). Cu₃(HHTP)₂ powder exhibited 0.62 \pm 0.04 and 0.87 \pm 0.05 mmol g⁻¹ uptake capacities of SO₂ in dry and humid air, while Cu₃(HHTP)₂@textile showed a lower uptake of 0.15 \pm 0.07 mmol g⁻¹ in dry air and 0.26 ± 0.11 mmol g⁻¹ in humid air. The lower loadings for the MOF/textile in comparison to the powder correlate well with the expected loadings based on a 38 wt % loading of MOF on textile. As seen in the breakthrough curves (Figure S74), after saturation occurred and the SO₂ was terminated, the effluent concentrations dropped rapidly toward the baseline, which indicated a chemisorption/chemical reaction event and permanent removal of the chemical.

To illustrate the practical applicability of the MOF/textile composites in multifunctional PPE, we fabricated a MOFcontaining mask (Figure 6B) by gluing a 1.5 cm \times 1.5 cm Cu₃(HHTP)₂@textile swatch to a KN95 respirator. The MOFmask PPE was equipped with conductive silver threads to provide good electrical contacts for chemiresistive sensing tests (Figure S75). The detection of SO₂ utilizing the mask prototype was collected and measured as the normalized conductance. The MOF-mask showed cyclic sensing capability toward 80 ppm SO₂ for 1 h and recovered in N₂ for 1 h three times, with maximum response changes of 50%, 15%, and 14%, respectively (Figure 6C). The demonstration and performance of the MOFmask PPE proves the effectiveness and potential of the templated fabrication technique for wearable multifunctional e-textile devices. It is worth noting that the toxicity and biocompatibility of Cu₃(HHTP)₂ remain unknown and require future investigation. Therefore, the Cu₃(HHTP)₂@textile device was integrated as an exterior sensor on the mask to avoid direct contact with the skin of the wearer.

Conclusion

This work demonstrates the first example of simultaneous detection, filtration, and detoxification of SO₂ using MOF-containing e-textiles obtained through a scalable templated fabrication method. The synthesized Cu₃(HHTP)₂@textile device exhibited noteworthy performance in terms of sub-ppm sensing limit (LOD of 0.43 ppm) and high adsorption capacity of SO₂ (0.8 mmol g⁻¹), making it a promising candidate for creating multifunctional e-textiles that provide timely alerting, personal protection, and air remediation. The resulting e-textiles are flexible, washable, and can be integrated into a smart mask capable of simultaneous sensing and filtration of toxic gas. Moreover, our comprehensive experimental and computational studies provide a key fundamental insight into the interactions of Cu₃(HHTP)₂ with SO₂, suggesting the conversion of SO₂ into less-toxic sulfate species through a redox reaction within the MOF.

As smart e-textile technology emerges as a burgeoning research field, 13,75-78 we believe this work has the potential to fill the gap in the design and implementation of smart membrane materials for widely distributed air quality management and monitoring. This work showcases the interdisciplinary feature of smart e-textile technology that relies on (1) the development of novel conductive and semi-conductive materials, (2) advancements in existing textile engineering techniques such as in situ deposition, layer-by-layer coating, and post-treatments to incorporate functional components, and (3) enhancement of sensor performance, regenerability, and reliability in textile environments. This work is poised to lay the scientific and technological foundation for the development of smart e-textiles and corresponding devices, enabling innovations across a wide range of applications including wearable sensors and filters, ^{48,51} smart PPE and air cleaning, ^{5,32,47} drug delivery and wound dressing, 27,75 and chemical and biological warfare defense.31,48,49

METHODS

General materials and instrumentations

Cu-coated polyester fabrics were purchased from Shieldex (Prag) (product ID: 1306081132, Hand sheet 9.9 cm \times 20.9 cm). The metallization process is electroless plating of Cu in an aqueous plating bath according to the company. Ammonium persulfate (7727-54-0, 98+% purity) was purchased from Sigma Aldrich. Sodium hydroxide (1310-73-2, ACS Grade) and trichloro (1H,1H,2H,2H-perfluorooctyl)silane (78560-45-9, 97%) were purchased from Fisher Scientific. 2,3,6,7,10,11-hexahydroxytriphenylene (HHTP) (4877-80-9, 97% purity) and copper hydroxide (Cu(OH)₂, 20427-59-2) were purchased from AmBeed.

SEM and EDX were performed using a Thermo Scientific Helios 5 CX DualBeam scanning electron microscope. PXRD measurements were performed with a Rigaku sixth generation MiniFlex X-ray diffractometer with a 600 W (40 kV, 15 mA) CuK α (α = 1.54 Å) radiation source. PXRD spectra were presented with the background subtracted and normalized by dividing by the intensity of the highest peak and multiplying by 100. XPS experiments were conducted on a Physical Electronics Versaprobe II X-ray Photoelectron Spectrometer under ultrahigh vacuum (base pressure 10-10 mbar). The measurement chamber was equipped with a monochromatic Al (Kα) X-ray source. Both survey and high-resolution spectra were obtained using a beam diameter of 200 µm. BET N2 gas adsorption measurements were performed with 3Flex (Micromeritics, Norcross, Georgia) instrument at 77 K. Textile samples (60-80 mg) were submerged in acetone for 1 day and vacuum dried at 80°C for 2 days for activation. Quantachrome Nova- 2200E BET Surface Area Analyzer was employed for the surface area analysis of BET measurements (surface area range: 0.01 m²/g to no known upper limit). BET isotherms plotted the quantity of gas adsorbed as a function of the relative pressure. The BET surface area was calculated based on the isotherms obtained from the relative pressure range of 0.05 to 0.3. The surface contact angle





was measured using a contact angle goniometer (Rame Hart Model 190-F2). For each measurement, a 2 µL droplet of deionized (DI) water was dispensed onto the substrate surface. Three measurements were performed for each sample. The left and right contact angles were determined using DROPimage CA software and then averaged. EPR spectra were collected using a Bruker EPR spectrometer operating at 9.77 GHz. Samples were analyzed under room temperature. TGA was performed using a TA Instruments TGA 55 instrument with a 10°C/min ramp from room temperature to 1,000°C under nitrogen. DRIFTS was performed on an IS-50 Fisher IR Spectrometer equipped with a Praying Mantis DRIFTS accessory (Harrick). Gas delivery was accomplished with a custom-built manifold having a gas inlet and gas outlet adapted for the Praying Mantis. Spectra were collected using a liquid N2-cooled mercury-cadmium-telluride (MCT) IR detector. Gas delivery was monitored with mass flow controllers.

Synthesis of Cu₃(HHTP)₂@textile

1.5 cm \times 1.5 cm pieces of Cu-coated textile swatches were ultrasonically cleaned in acetone, ethanol, and deionized water consecutively for 10 min. The fabric swatches were air dried and submerged in 10 mL of 2.67 M NaOH and 0.133 M ammonium persulfate ((NH₄)₂S₂O₈) stock solution for 0.5 h. The formed Cu(OH)₂@textile devices were rinsed with ethanol, water, and acetone three times after reaction, and air dried overnight. 1.5 cm \times 1.5 cm pieces of Cu(OH)₂@textile were submerged in 1 mL of 60 mM HHTP in H₂O/EtOH (volume ratio = 1:1) co-solvent and open to ambient air for 20 h. The formed Cu₃(HHTP)₂@textile devices were rinsed with ethanol, water, and acetone three times after reaction, and air dried overnight.

 $\label{lem:potential} \textbf{Detailed methods can be found in the } \textbf{supplemental information.}$

RESOURCE AVAILABILITY

Lead contact

Requests for further information and resources should be directed to and will be fulfilled by the lead contact, Katherine A. Mirica (katherine.a.mirica@dartmouth.edu).

Materials availability

Any unique materials generated in this study are available from the lead contact with a completed material transfer agreement.

Data and code availability

This study did not generate datasets or code.

ACKNOWLEDGMENTS

The authors acknowledge support from funds provided by the Dartmouth Guarini School PhD Innovation Program, NSF CAREER award (1945218), NIH MIRA Award (R35GM138318), United States Army Research Office Grant (W911NF2320020), and National Science Foundation Research Traineeship Award (2125733). I.A.I. thanks PAPIIT-UNAM (IN201123) for financial support. G.W.P. acknowledges the Defense Threat Reduction Agency for partially funding this effort under CB11222.

AUTHOR CONTRIBUTIONS

K.A.M. conceived the project; Z.Z., A.M.E., and N.V. designed the experiments and methods; Z.Z., P.D., R.W., J.T.A., and S.G. prepared and characterized the materials; E.S.-G. and I.A.I. conducted and analyzed isotherm experi-

ments; G.W.P. and B.B. conducted and analyzed micro-breakthrough experiments; S.M. and G.B. conducted computational studies; Z.Z., P.D., S.M., G.B., I.A.I., and K.A.M. wrote the paper. All authors discussed the results and edited the manuscript.

DECLARATION OF INTERESTS

The authors declare no competing interests.

SUPPLEMENTAL INFORMATION

Supplemental information can be found online at https://doi.org/10.1016/j.chempr.2025.102580.

Received: October 18, 2024 Revised: February 17, 2025 Accepted: April 15, 2025 Published: May 12, 2025

REFERENCES

- Seinfeld, J.H. (1989). Urban air pollution: state of the science. Science 243, 745–752. https://doi.org/10.1126/science.243.4892.745.
- Sigsgaard, T., and Hoffmann, B. (2024). Assessing the health burden from air pollution. Science 384, 33–34. https://doi.org/10.1126/science.abo3801.
- Barea, E., Montoro, C., and Navarro, J.A.R. (2014). Toxic gas removal-metal-organic frameworks for the capture and degradation of toxic gases and vapours. Chem. Soc. Rev. 43, 5419–5430. https://doi.org/10.1039/c3cs60475f.
- DeCoste, J.B., and Peterson, G.W. (2014). Metal-organic frameworks for air purification of toxic chemicals. Chem. Rev. 114, 5695–5727. https:// doi.org/10.1021/cr4006473.
- Kumar, P., Kim, K.H., Kwon, E.E., and Szulejko, J.E. (2016). Metal-organic frameworks for the control and management of air quality: advances and future direction. J. Mater. Chem. A 4, 345–361. https://doi.org/10.1039/ c5ta07068f.
- Kumar, P., Vejerano, E., Khan, A., Lisak, G., Ahn, J.H., and Kim, K.H. (2019). Metal organic frameworks (MOFs): Currents trends and challenges in control and management of air quality. Korean J. Chem. Eng. 36, 1839–1853. https://doi.org/10.1007/s11814-019-0378-8.
- Huang, W., Xu, H., Wu, J., Ren, M., Ke, Y., and Qiao, J. (2024). Toward cleaner air and better health: Current state, challenges, and priorities. Science 385, 386–390. https://doi.org/10.1126/science.adp7832.
- 8. Jia, Z., Ai, Z., and Zhang, C. (2024). Mechanism of respiratory protective equipment in controlling wearer's exhaled pollutants. Sep. Purif. Technol. 350, 128028. https://doi.org/10.1016/j.seppur.2024.128028.
- Feng, T., Sun, Y., Shi, Y., Ma, J., Feng, C., and Chen, Z. (2024). Air pollution control policies and impacts: A review. Renew. Sustain. Energy Rev. 191, 114071. https://doi.org/10.1016/j.rser.2023.114071.
- Bandodkar, A.J., Jeerapan, I., and Wang, J. (2016). Wearable Chemical Sensors: Present Challenges and Future Prospects. ACS Sens. 1, 464–482. https://doi.org/10.1021/acssensors.6b00250.
- Tai, H., Wang, S., Duan, Z., and Jiang, Y. (2020). Evolution of breath analysis based on humidity and gas sensors: Potential and challenges. Sens. Actuators B 318. https://doi.org/10.1016/j.snb.2020.128104.
- Verma, G., Gokarna, A., Kadiri, H., Nomenyo, K., Lerondel, G., and Gupta, A. (2023). Multiplexed Gas Sensor: Fabrication Strategies, Recent Progress, and Challenges. ACS Sens. 8, 3320–3337. https://doi.org/10.1021/acssensors.3c01244.
- Eagleton, A.M., Ambrogi, E.K., Miller, S.A., Vereshchuk, N., and Mirica, K. A. (2023). Fiber Integrated Metal-Organic Frameworks as Functional Components in Smart Textiles. Angew. Chem. Int. Ed. Engl. 62, e202309078. https://doi.org/10.1002/anie.202309078.





- Ma, K.K., Idrees, K.B., Son, F.A., Maldonado, R., Wasson, M.C., Zhang, X., Wang, X.J., Shehayeb, E., Merhi, A., Kaafarani, B.R., et al. (2020). Fiber Composites of Metal-Organic Frameworks. Chem. Mater. 32, 7120– 7140. https://doi.org/10.1021/acs.chemmater.0c02379.
- Loke, G., Alain, J., Yan, W., Khudiyev, T., Noel, G., Yuan, R., Missakian, A., and Fink, Y. (2020). Computing Fabrics. Matter 2, 786–788. https://doi. org/10.1016/j.matt.2020.03.007.
- Furukawa, H., Cordova, K.E., O'Keeffe, M., and Yaghi, O.M. (2013). The chemistry and applications of metal-organic frameworks. Science 341, 1230444. https://doi.org/10.1126/science.1230444.
- Zhou, H.C., Long, J.R., and Yaghi, O.M. (2012). Introduction to metalorganic frameworks. Chem. Rev. 112, 673–674. https://doi.org/10.1021/ cr300014x.
- Eagleton, A.M., Ko, M., Stolz, R.M., Vereshchuk, N., Meng, Z., Mendecki, L., Levenson, A.M., Huang, C., MacVeagh, K.C., Mahdavi-Shakib, A., et al. (2022). Fabrication of Multifunctional Electronic Textiles Using Oxidative Restructuring of Copper into a Cu-Based Metal-Organic Framework. J. Am. Chem. Soc. 144, 23297–23312. https://doi.org/10.1021/jacs. 2c05510.
- Küsgens, P., Siegle, S., and Kaskel, S. (2009). Crystal Growth of the Metal—Organic Framework Cu3(BTC)2 on the Surface of Pulp Fibers. Adv. Eng. Mater. 11, 93–95. https://doi.org/10.1002/adem.200800274.
- Zhao, J.J., Losego, M.D., Lemaire, P.C., Williams, P.S., Gong, B., Atanasov, S.E., Blevins, T.M., Oldham, C.J., Walls, H.J., Shepherd, S.D., et al. (2014). Highly Adsorptive, MOF-Functionalized Nonwoven Fiber Mats for Hazardous Gas Capture Enabled by Atomic Layer Deposition. Adv. Materials Inter. 1, 1400040. https://doi.org/10.1002/admi.201400040.
- Lee, D.T., Zhao, J., Oldham, C.J., Peterson, G.W., and Parsons, G.N. (2017). UiO-66-NH2 Metal-Organic Framework (MOF) Nucleation on TiO2, ZnO, and Al2O3 Atomic Layer Deposition-Treated Polymer Fibers: Role of Metal Oxide on MOF Growth and Catalytic Hydrolysis of Chemical Warfare Agent Simulants. ACS Appl. Mater. Interfaces 9, 44847–44855. https://doi.org/10.1021/acsami.7b15397.
- Lee, H., and Jeon, S. (2020). Polyacrylonitrile Nanofiber Membranes Modified with Ni-Based Conductive Metal Organic Frameworks for Air Filtration and Respiration Monitoring. ACS Appl. Nano Mater. 3, 8192–8198. https://doi.org/10.1021/acsanm.0c01619.
- Duan, J., Li, Q., Xu, W., Hu, X., Wang, Y., Valdez, S.M., Qiang, Z., Liao, Y., Wen, J., Ye, C., et al. (2024). Mechanically Flexible and Weavable Hybrid Aerogel Fibers with Ultrahigh Metal–Organic Framework Loadings for Versatile Applications. ACS Appl. Polym. Mater. 6, 1900–1910. https://doi. org/10.1021/acsapm.3c02734.
- Rauf, S., Vijjapu, M.T., Andrés, M.A., Gascón, I., Roubeau, O., Eddaoudi, M., and Salama, K.N. (2020). Highly Selective Metal-Organic Framework Textile Humidity Sensor. ACS Appl. Mater. Interfaces 12, 29999–30006. https://doi.org/10.1021/acsami.0c07532.
- Smith, M.K., and Mirica, K.A. (2017). Self-Organized Frameworks on Textiles (SOFT): Conductive Fabrics for Simultaneous Sensing, Capture, and Filtration of Gases. J. Am. Chem. Soc. 139, 16759–16767. https://doi.org/10.1021/jacs.7b08840.
- Emam, H.E., Abdelhamid, H.N., and Abdelhameed, R.M. (2018). Self-cleaned photoluminescent viscose fabric incorporated lanthanide-organic framework (Ln-MOF). Dyes Pigm. 159, 491–498. https://doi.org/10.1016/j.dyepig.2018.07.026.
- Noorian, S.A., Hemmatinejad, N., and Navarro, J.A.R. (2019). Bio-MOF@cellulose fabric composites for bioactive molecule delivery.
 J. Inorg. Biochem. 201, 110818. https://doi.org/10.1016/j.jinorgbio.2019.
 110818.
- Lee, D.T., Jamir, J.D., Peterson, G.W., and Parsons, G.N. (2020). Protective Fabrics: Metal-Organic Framework Textiles for Rapid Photocatalytic Sulfur Mustard Simulant Detoxification. Matter 2, 404–415. https://doi.org/10.1016/j.matt.2019.11.005.

- Li, W., Zhang, Y., Yu, Z., Zhu, T., Kang, J., Liu, K., Li, Z., and Tan, S.C. (2022). In Situ Growth of a Stable Metal-Organic Framework (MOF) on Flexible Fabric via a Layer-by-Layer Strategy for Versatile Applications. ACS Nano 16, 14779–14791. https://doi.org/10.1021/acsnano.2c05624.
- Smith, M.K., Jensen, K.E., Pivak, P.A., and Mirica, K.A. (2016). Direct Self-Assembly of Conductive Nanorods of Metal-Organic Frameworks into Chemiresistive Devices on Shrinkable Polymer Films. Chem. Mater. 28, 5264–5268. https://doi.org/10.1021/acs.chemmater.6b02528.
- Barton, H.F., Davis, A.K., and Parsons, G.N. (2020). The Effect of Surface Hydroxylation on MOF Formation on ALD Metal Oxides: MOF-525 on TiO2/Polypropylene for Catalytic Hydrolysis of Chemical Warfare Agent Simulants. ACS Appl. Mater. Interfaces 12, 14690–14701. https://doi. org/10.1021/acsami.9b20910.
- Li, P., Li, J., Feng, X., Li, J., Hao, Y., Zhang, J., Wang, H., Yin, A., Zhou, J., Ma, X., et al. (2019). Metal-organic frameworks with photocatalytic bactericidal activity for integrated air cleaning. Nat. Commun. 10, 2177. https://doi.org/10.1038/s41467-019-10218-9.
- Emam, H.E., and Abdelhameed, R.M. (2017). Anti-UV Radiation Textiles
 Designed by Embracing with Nano-MIL (Ti, In)-Metal Organic Framework. ACS Appl. Mater. Interfaces 9, 28034–28045. https://doi.org/10.
 1021/acsami.7b07357.
- Hashem, T., Ibrahim, A.H., Wöll, C., and Alkordi, M.H. (2019). Grafting Zirconium-Based Metal-Organic Framework UiO-66-NH 2 Nanoparticles on Cellulose Fibers for the Removal of Cr(VI) Ions and Methyl Orange from Water. ACS Appl. Nano Mater. 2, 5804–5808. https://doi.org/10. 1021/acsanm.9b01263.
- Rubin, H.N., Neufeld, B.H., and Reynolds, M.M. (2018). Surface-Anchored Metal-Organic Framework-Cotton Material for Tunable Antibacterial Copper Delivery. ACS Appl. Mater. Interfaces 10, 15189–15199. https://doi. org/10.1021/acsami.7b19455.
- de Koning, M.C., Ma, K., van Grol, M., Iordanov, I., Kruijne, M.J.L., Idrees, K.B., Xie, H., Islamoglu, T., Bross, R.P.T., and Farha, O.K. (2022). Development of a Metal-Organic Framework/Textile Composite for the Rapid Degradation and Sensitive Detection of the Nerve Agent VX. Chem. Mater. 34, 1269–1277. https://doi.org/10.1021/acs.chemmater.1c03895.
- Yu, M., Li, W., Wang, Z., Zhang, B., Ma, H., Li, L., and Li, J. (2016). Covalent immobilization of metal-organic frameworks onto the surface of nylon–a new approach to the functionalization and coloration of textiles. Sci. Rep. 6, 22796. https://doi.org/10.1038/srep22796.
- Lee, D.T., Zhao, J.J., Peterson, G.W., and Parsons, G.N. (2017). Catalytic "MOF-Cloth" Formed via Directed Supramolecular Assembly of UiO-66-NH 2 Crystals on Atomic Layer Deposition-Coated Textiles for Rapid Degradation of Chemical Warfare Agent Simulants. Chem. Mater. 29, 4894–4903. https://doi.org/10.1021/acs.chemmater.7b00949.
- Lee, D.T., Jamir, J.D., Peterson, G.W., and Parsons, G.N. (2019). Water-Stable Chemical-Protective Textiles via Euhedral Surface-Oriented 2D Cu-TCPP Metal-Organic Frameworks. Small 15, e1805133. https://doi. org/10.1002/smll.201805133.
- Kalaj, M., Denny, M.S., Bentz, K.C., Palomba, J.M., and Cohen, S.M. (2019). Nylon-MOF Composites through Postsynthetic Polymerization. Angew. Chem. Int. Ed. Engl. 58, 2336–2340. https://doi.org/10.1002/anje.201812655
- Kalaj, M., and Cohen, S.M. (2020). Spray-Coating of Catalytically Active MOF-Polythiourea through Postsynthetic Polymerization. Angew. Chem. Int. Ed. Engl. 59, 13984–13989. https://doi.org/10.1002/anie.202004205.
- Abdelhamid, H.N., and Mathew, A.P. (2022). Cellulose–metal organic frameworks (CelloMOFs) hybrid materials and their multifaceted Applications: A review. Coord. Chem. Rev. 451. https://doi.org/10.1016/j.ccr. 2021.214263.
- Yao, M.S., Lv, X.J., Fu, Z.H., Li, W.H., Deng, W.H., Wu, G.D., and Xu, G. (2017). Layer-by-Layer Assembled Conductive Metal-Organic Framework Nanofilms for Room-Temperature Chemiresistive Sensing. Angew. Chem. Int. Ed. Engl. 56, 16510–16514. https://doi.org/10.1002/anie.201709558.

Chem Article



- Chen, Y., Li, S., Pei, X., Zhou, J., Feng, X., Zhang, S., Cheng, Y., Li, H., Han, R., and Wang, B. (2016). A Solvent-Free Hot-Pressing Method for Preparing Metal-Organic-Framework Coatings. Angew. Chem. Int. Ed. Engl. 55, 3419–3423. https://doi.org/10.1002/anie.201511063.
- Turetsky, D., Alzate-Sánchez, D.M., Wasson, M.C., Yang, A., Noh, H., Atilgan, A., Islamoglu, T., Farha, O.K., and Dichtel, W.R. (2022). Hot Press Synthesis of MOF/Textile Composites for Nerve Agent Detoxification. ACS Materials Lett. 4, 1511–1515. https://doi.org/10.1021/acsmaterialslett.2c00258.
- Molco, M., Laye, F., Samperio, E., Ziv Sharabani, S., Fourman, V., Sherman, D., Tsotsalas, M., Wöll, C., Lahann, J., and Sitt, A. (2021). Performance Fabrics Obtained by In Situ Growth of Metal-Organic Frameworks in Electrospun Fibers. ACS Appl. Mater. Interfaces 13, 12491–12500. https://doi.org/10.1021/acsami.0c22729.
- Liang, C., Li, J., Chen, Y., Ke, L., Zhu, J., Zheng, L., Li, X.P., Zhang, S., Li, H., Zhong, G.J., et al. (2023). Self-Charging, Breathable, and Antibacterial Poly(lactic acid) Nanofibrous Air Filters by Surface Engineering of Ultrasmall Electroactive Nanohybrids. ACS Appl. Mater. Interfaces 15, 57636–57648. https://doi.org/10.1021/acsami.3c13825.
- Kirlikovali, K.O., Chen, Z., Islamoglu, T., Hupp, J.T., and Farha, O.K. (2020). Zirconium-Based Metal-Organic Frameworks for the Catalytic Hydrolysis of Organophosphorus Nerve Agents. ACS Appl. Mater. Interfaces 12, 14702–14720. https://doi.org/10.1021/acsami.9b20154.
- Ma, K.K., Cheung, Y.H., Kirlikovali, K.O., Wang, X.L., Islamoglu, T., Xin, J.H., and Farha, O.K. (2023). Protection against Chemical Warfare Agents and Biological Threats Using Metal-Organic Frameworks as Active Layers. Acc. Mater. Res. 4, 168–179. https://doi.org/10.1021/accountsmr.2c00200.
- Gogoi, C., Rana, A., Ghosh, S., Fopase, R., Pandey, L.M., and Biswas, S. (2022). Superhydrophobic Self-Cleaning Composite of a Metal-Organic Framework with Polypropylene Fabric for Efficient Removal of Oils from Oil-Water Mixtures and Emulsions. ACS Appl. Nano Mater. 5, 10003–10014. https://doi.org/10.1021/acsanm.2c02418.
- Campbell, M.G., and Dinca, M. (2017). Metal-Organic Frameworks as Active Materials in Electronic Sensor Devices. Sensors (Basel) 17, 1108. https://doi.org/10.3390/s17051108.
- Campbell, M.G., Liu, S.F., Swager, T.M., and Dinca, M. (2015). Chemiresistive Sensor Arrays from Conductive 2D Metal-Organic Frameworks.
 J. Am. Chem. Soc. 137, 13780–13783. https://doi.org/10.1021/jacs. 5b09600.
- Martínez-Ahumada, E., López-Olvera, A., Jancik, V., Sánchez-Bautista, J. E., González-Zamora, E., Martis, V., Williams, D.R., and Ibarra, I.A. (2020).
 MOF Materials for the Capture of Highly Toxic H₂S and SO₂. Organometallics 39, 883–915. https://doi.org/10.1021/acs.organomet.9b00735.
- Martínez-Ahumada, E., Díaz-Ramírez, M.L., Velásquez-Hernández, M.J., Jancik, V., and Ibarra, I.A. (2021). Capture of toxic gases in MOFs: SO2, H2S, NH3 and NO x. Chem. Sci. 12, 6772–6799. https://doi.org/10. 1039/d1sc01609a.
- Chernikova, V., Yassine, O., Shekhah, O., Eddaoudi, M., and Salama, K.N. (2018). Highly sensitive and selective SO 2 MOF sensor: the integration of MFM-300 MOF as a sensitive layer on a capacitive interdigitated electrode. J. Mater. Chem. A 6, 5550–5554. https://doi.org/10. 1039/c7ta10538i
- Brandt, P., Nuhnen, A., Lange, M., Möllmer, J., Weingart, O., and Janiak, C. (2019). Metal-Organic Frameworks with Potential Application for SO2 Separation and Flue Gas Desulfurization. ACS Appl. Mater. Interfaces 11, 17350–17358. https://doi.org/10.1021/acsami.9b00029.
- Cui, X., Yang, Q., Yang, L., Krishna, R., Zhang, Z., Bao, Z., Wu, H., Ren, Q., Zhou, W., Chen, B., et al. (2017). Ultrahigh and Selective SO2 Uptake in Inorganic Anion-Pillared Hybrid Porous Materials. Adv. Mater. 29, 1606929. https://doi.org/10.1002/adma.201606929.
- Savage, M., Cheng, Y., Easun, T.L., Eyley, J.E., Argent, S.P., Warren, M.R., Lewis, W., Murray, C., Tang, C.C., Frogley, M.D., et al. (2016).
 Selective Adsorption of Sulfur Dioxide in a Robust Metal-Organic

- Framework Material. Adv. Mater. 28, 8705–8711. https://doi.org/10.1002/adma.201602338.
- Espejo, E.M.A., and Balela, M.D.L. (2017). Facile synthesis of cupric hydroxide and cupric oxide on copper foil for potential electrochemical applications. IOP Conf. Ser.: Mater. Sci. Eng. 201, 012050. https://doi.org/10.1088/1757-899X/201/1/012050.
- Snook, K.M., Zasada, L.B., Chehada, D., and Xiao, D.J. (2022). Oxidative control over the morphology of Cu3(HHTP)2, a 2D conductive metalorganic framework. Chem. Sci. 13, 10472–10478. https://doi.org/10. 1039/d2sc03648g.
- Ghosh, S. (2019). Electroless copper deposition: A critical review. Thin Solid Films 669, 641–658. https://doi.org/10.1016/j.tsf.2018.11.016.
- Rubio-Giménez, V., Galbiati, M., Castells-Gil, J., Almora-Barrios, N., Navarro-Sánchez, J., Escorcia-Ariza, G., Mattera, M., Arnold, T., Rawle, J., Tatay, S., et al. (2018). Bottom-Up Fabrication of Semiconductive Metal-Organic Framework Ultrathin Films. Adv. Mater. 30, 1704291. https://doi.org/10.1002/adma.201704291.
- de Lourdes Gonzalez-Juarez, M., Morales, C., Flege, J.I., Flores, E., Martin-Gonzalez, M., Nandhakumar, I., and Bradshaw, D. (2022). Tunable Carrier Type of a Semiconducting 2D Metal-Organic Framework Cu3(HHTP)2.
 ACS Appl. Mater. Interfaces 14, 12404–12411. https://doi.org/10.1021/acsami.2c00089.
- Lane, M.D. (2007). Mid-infrared emission spectroscopy of sulfate and sulfate-bearing minerals. Am. Mineral. 92, 1–18. https://doi.org/10.2138/am. 2007.2170.
- Buzgar, N., Buzatu, A., and Sanislav, I.V. (2009). The Raman Study of Certain Sulfates. Analele Stiintifice de Universitatii A.I. Cuza din lasi. Sect. 2, Geologie 55, 5–23.
- Scamporrino, A.A., Puglisi, C., Spina, A., Montaudo, M., Zampino, D.C., Cicala, G., Ognibene, G., Mauro, C.D., Dattilo, S., Mirabella, E.F., et al. (2020). Synthesis and Characterization of Copoly(Ether Sulfone)s with Different Percentages of Diphenolic Acid Units. Polymers (Basel) 12, 1817. https://doi.org/10.3390/polym12081817.
- Bounechada, D., Darmastuti, Z., Andersson, M., Ojamäe, L., Lloyd Spetz, A., Skoglundh, M., and Carlsson, P.-A. (2014). Vibrational Study of SO x Adsorption on Pt/SiO 2. J. Phys. Chem. C 118, 29713–29723. https://doi.org/10.1021/jp506644w.
- Stolz, R.M., Mahdavi-Shakib, A., Frederick, B.G., and Mirica, K.A. (2020). Host–Guest Interactions and Redox Activity in Layered Conductive Metal–Organic Frameworks. Chem. Mater. 32, 7639–7652. https://doi.org/10.1021/acs.chemmater.0c01007.
- Meng, Z., and Mirica, K.A. (2021). Two-dimensional d-π conjugated metalorganic framework based on hexahydroxytrinaphthylene. Nano Res. 14, 369–375. https://doi.org/10.1007/s12274-020-2874-x.
- Park, J., Hinckley, A.C., Huang, Z., Feng, D., Yakovenko, A.A., Lee, M., Chen, S., Zou, X., and Bao, Z. (2018). Synthetic Routes for a 2D Semiconductive Copper Hexahydroxybenzene Metal-Organic Framework. J. Am. Chem. Soc. 140, 14533–14537. https://doi.org/10.1021/ jacs.8b06666.
- Gittins, J.W., Balhatchet, C.J., Fairclough, S.M., and Forse, A.C. (2022). Enhancing the energy storage performances of metal-organic frameworks by controlling microstructure. Chem. Sci. 13, 9210–9219. https://doi.org/ 10.1039/d2sc03389e.
- Shi, Y., Momeni, M.R., Chen, Y.-J., Limbu, D.K., Zhang, Z., and Shakib, F. A. (2022). Water Induced Structural Transformations in Flexible Two-Dimensional Layered Conductive Metal-Organic Frameworks. Chem. Mater. 34, 7730–7740. https://doi.org/10.1021/acs.chemmater.2c00989.
- Brandt, P., Xing, S.H., Liang, J., Kurt, G., Nuhnen, A., Weingart, O., and Janiak, C. (2021). Zirconium and Aluminum MOFs for Low-Pressure SO2 Adsorption and Potential Separation: Elucidating the Effect of Small Pores and NH2 Groups. ACS Appl. Mater. Interfaces 13, 29137–29149. https:// doi.org/10.1021/acsami.1c06003.





- Smith, G.L., Eyley, J.E., Han, X., Zhang, X., Li, J., Jacques, N.M., Godfrey, H.G.W., Argent, S.P., McCormick McPherson, L.J., Teat, S.J., et al. (2019). Reversible coordinative binding and separation of sulfur dioxide in a robust metal-organic framework with open copper sites. Nat. Mater. 18, 1358–1365. https://doi.org/10.1038/s41563-019-0495-0.
- Park, S., Loke, G., Fink, Y., and Anikeeva, P. (2019). Flexible fiber-based optoelectronics for neural interfaces. Chem. Soc. Rev. 48, 1826–1852. https://doi.org/10.1039/c8cs00710a.
- 76. Chen, M., Liu, J., Li, P., Gharavi, H., Hao, Y., Ouyang, J., Hu, J., Hu, L., Hou, C., Humar, I., et al. (2022). Fabric computing: Concepts, opportu-
- nities, and challenges. Innovation (Camb) 3, 100340. https://doi.org/10.1016/j.xinn.2022.100340.
- Chen, G., Xiao, X., Zhao, X., Tat, T., Bick, M., and Chen, J. (2022). Electronic Textiles for Wearable Point-of-Care Systems. Chem. Rev. 122, 3259–3291. https://doi.org/10.1021/acs.chemrev.1c00502.
- Zhang, Y., Xia, X., Ma, K., Xia, G., Wu, M., Cheung, Y.H., Yu, H., Zou, B., Zhang, X., Farha, O.K., et al. (2023). Functional Textiles with Smart Properties: Their Fabrications and Sustainable Applications. Adv. Funct. Materials 33, 2301607. https://doi.org/10.1002/adfm.202301607.

Supplemental information

Scalable templated fabrication of Cu-based MOF on textiles for simultaneous sensing, filtration, and detoxification of SO_2

Zhuoran Zhong, Patrick Damacet, Elí Sánchez-González, Aileen M. Eagleton, Nataliia Vereshchuk, Ravint Wongratanaphisan, Jamison T. Anderson, Sofia Goncalves, Gregory W. Peterson, Brandon Blount, Susanna Monti, Giovanni Barcaro, Ilich A. Ibarra, and Katherine A. Mirica

Supplemental Methods

Scalable Templated Fabrication of Cu-based MOF on Textiles for Simultaneous Sensing, Filtration, and Detoxification of SO₂

Zhuoran Zhong¹, Patrick Damacet¹, Elí Sánchez-González², Aileen M. Eagleton¹, Nataliia Vereshchuk¹, Ravint Wongratanaphisan¹, Jamison T. Anderson¹, Sofia Goncalves¹, Gregory W. Peterson³, Brandon Blount⁴, Susanna Monti⁵, Giovanni Barcaro^{6*}, Ilich A. Ibarra^{2**} and Katherine A. Mirica^{1,7***}

¹Department of Chemistry, Burke Laboratory, Dartmouth College, Hanover, New Hampshire 03755, United States

²Laboratorio de Fisicoquímica y Reactividad deSuperficies (LaFReS), Instituto de Investigaciones en Materiales, Universidad Nacional Autónoma de México, 04510 Ciudad de México, Mexico

³DEVCOM Chemical Biological Center, 8198 Blackhawk Road, Aberdeen Proving Ground, Maryland 21010-5424, United States

⁴Leidos, Inc., Abingdon, Maryland 21009, United States

⁵CNR-ICCOM, Institute of Chemistry of Organometallic Compounds, Area della Ricerca, Pisa I56124, Italy

⁶CNR-IPCF, Institute for Chemical and Physical Processes, Area della Ricerca, Pisa I-56124, Italy

⁷Lead Contact

*Correspondence: giovanni.barcaro@pi.ipcf.cnr.it

**Correspondence: argel@unam.mx

***Correspondence: <u>Katherine.A.Mirica@dartmouth.edu</u>

Table of Contents

1. Preparation and optimization	3
1.1. Preparation and optimization of Cu(OH) ₂ textile	3
1.2. Preparation and optimization of Cu ₃ (HHTP) ₂ @textile	4
2. Characterizations studies	6
2.1. Scanning electron microscopy and energy dispersive X-ray spectroscopy	6
2.2. Inductively Coupled Plasma Mass Spectrometry (ICP-MS) analysis	10
2.3. Control over Cu ₃ (HHTP) ₂ growth on the textile by varying reaction time	11
2.4. Stability tests	14
2.5. Brunauer–Emmett–Teller analysis	15
2.6. Thermogravimetric analysis	16
2.7. Preparation and characterization of bulk Cu ₃ (HHTP) ₂	17
3. Gas sensing experiments	19
3.1. Experiment and device setup	19
3.2. Cyclic sensing experiments	21
3.3. Preparation, characterization, and sensing of Cu ₃ (HHTP) ₂ @textile-F	34
3.4. Regenerability evaluation of Cu ₃ (HHTP) ₂ @textile	40
4. Spectroscopic investigation	41
5. Theoretical activity	48
5.1. Periodic quantum chemistry calculations at the DFT level	48
5.2. Preliminary considerations and RMD simulations set up	49
5.3. RMD simulations details and analysis tools	50
6. Adsorption study	68
6.1. Isotherm experiments	68
6.2. Micro-Breakthrough experiments	72
7 Mask demonstration	74

1. Preparation and Optimization

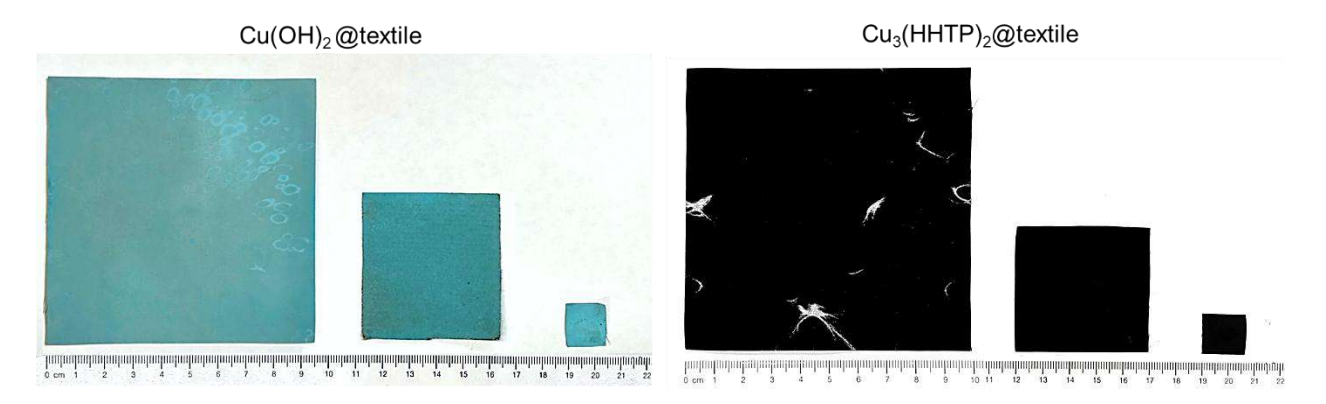


Figure S1. Scalable templated fabrication of $Cu(OH)_2$ @textile and $Cu_3(HHTP)_2$ @textile with the dimensions of 1.5 cm ×1.5 cm, 5 cm ×5 cm, and 10 cm ×10 cm. It shows that this templated fabrication of $Cu(OH)_2$ @textile and $Cu_3(HHTP)_2$ @textile is easily adaptable to different dimensions of textile swatches up to 10 cm × 10 cm. $Cu(OH)_2$ and $Cu_3(HHTP)_2$ were evenly and stably coated on the textiles. A minimal portion of $Cu_3(HHTP)_2$ peeled off the textile for the 10 cm ×10 cm $Cu_3(HHTP)_2$ @textile.

1.1. Preparation and optimization of Cu(OH)₂@textile

Cu(OH)₂@textile was synthesized following a reported method.¹ 1.5 cm ×1.5 cm pieces of textile swatches were ultrasonically cleaned in acetone, ethanol, and deionized water consecutively for 10 min. The fabric swatches were air dried and submerged in 10 mL of 2.67 M NaOH and 0.133 M ammonium persulfate ((NH₄)₂S₂O₈) stock solution for 0.5 h. All the fabric devices were rinsed with ethanol, water, acetone three times after reaction, and air dried overnight before characterizations and tests.

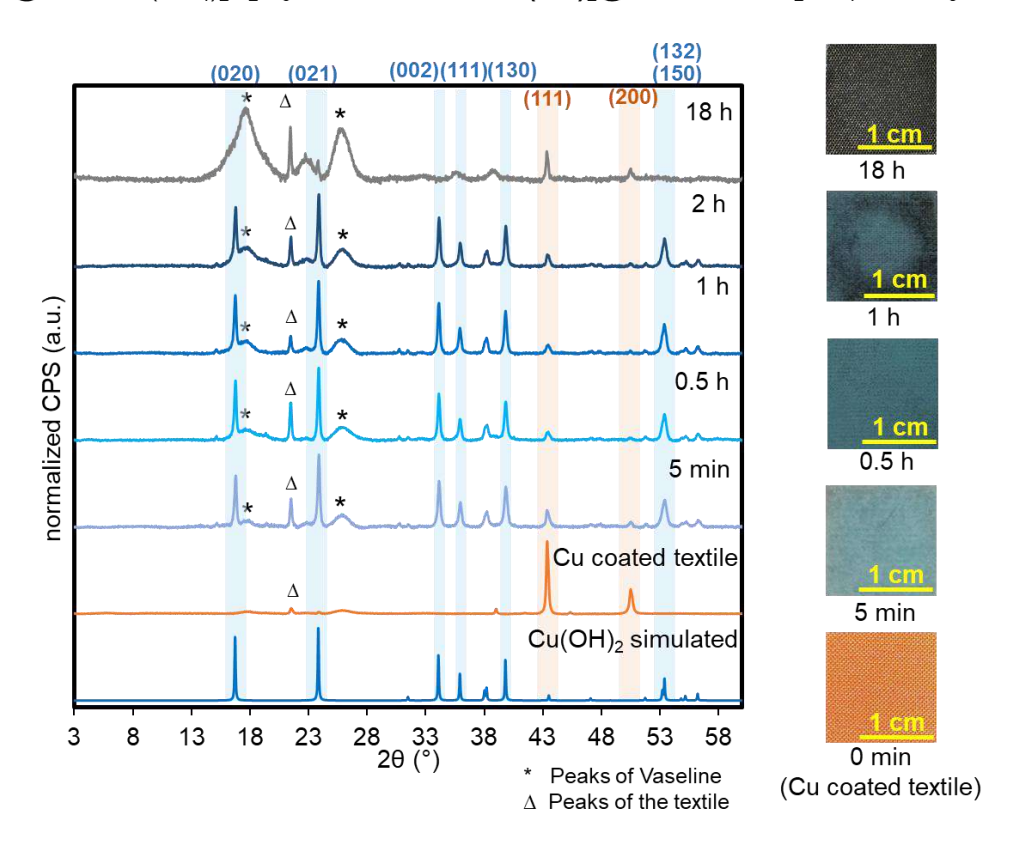


Figure S2. PXRD analysis and photographs of Cu(OH)₂@textile under varied reaction time. The color of the fabric surface turned from red to blue after 5 minutes of reaction time, indicating the rapid formation of Cu(OH)₂ on textile swatches. The color of the fabric surface turned black after 18 h, indicating the overreaction and the loss of Cu on textile swatches.

1.2. Preparation and optimization of Cu₃(HHTP)₂@textile

Cu₃(HHTP)₂@textile was synthesized and optimized based on our group's reported method.² 1.5 cm ×1.5 cm pieces of Cu(OH)₂@textile swatches were submerged in 1 mL of 60 mM HHTP in H2O/EtOH (volume ratio = 1:1) cosolvent. A complete conversion from blue Cu(OH)₂ to black Cu₃(HHTP)₂ on the textiles was visible by leaving the vial uncapped and open to ambient air for 20 hours. All the fabric devices were rinsed with ethanol, water, acetone three times after reaction, and air dried overnight before characterizations and tests.

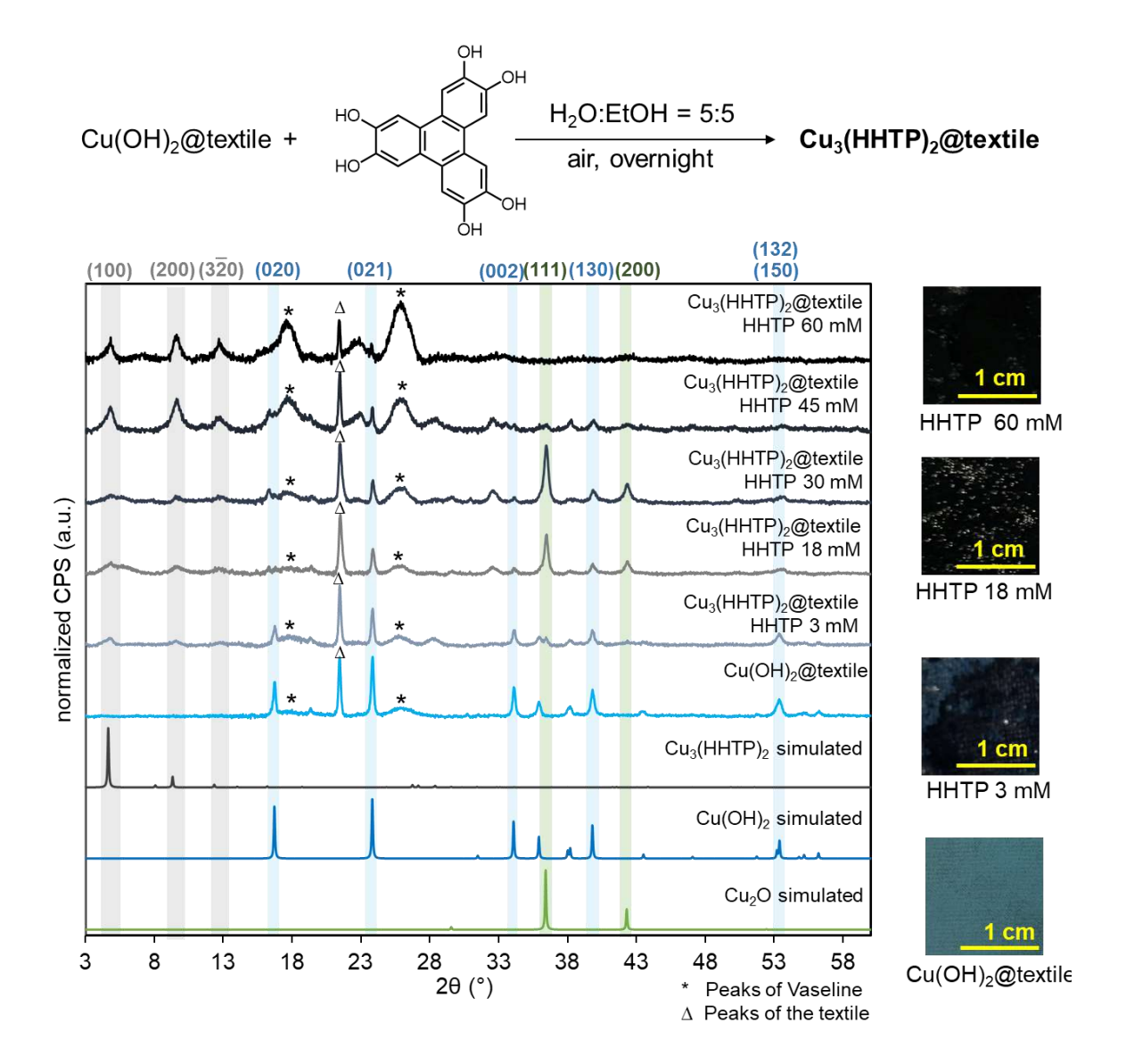


Figure S3. PXRD analysis and photographs of Cu₃(HHTP)₂@textile using varied concentrations of HHTP. The disappearance of peaks corresponding to the (020), (002), (130) planes of Cu(OH)₂ on textile swatch indicates the complete conversion from Cu(OH)₂@textile to Cu₃(HHTP)₂@textile employing 60 mM of HHTP as the optimal concentration.

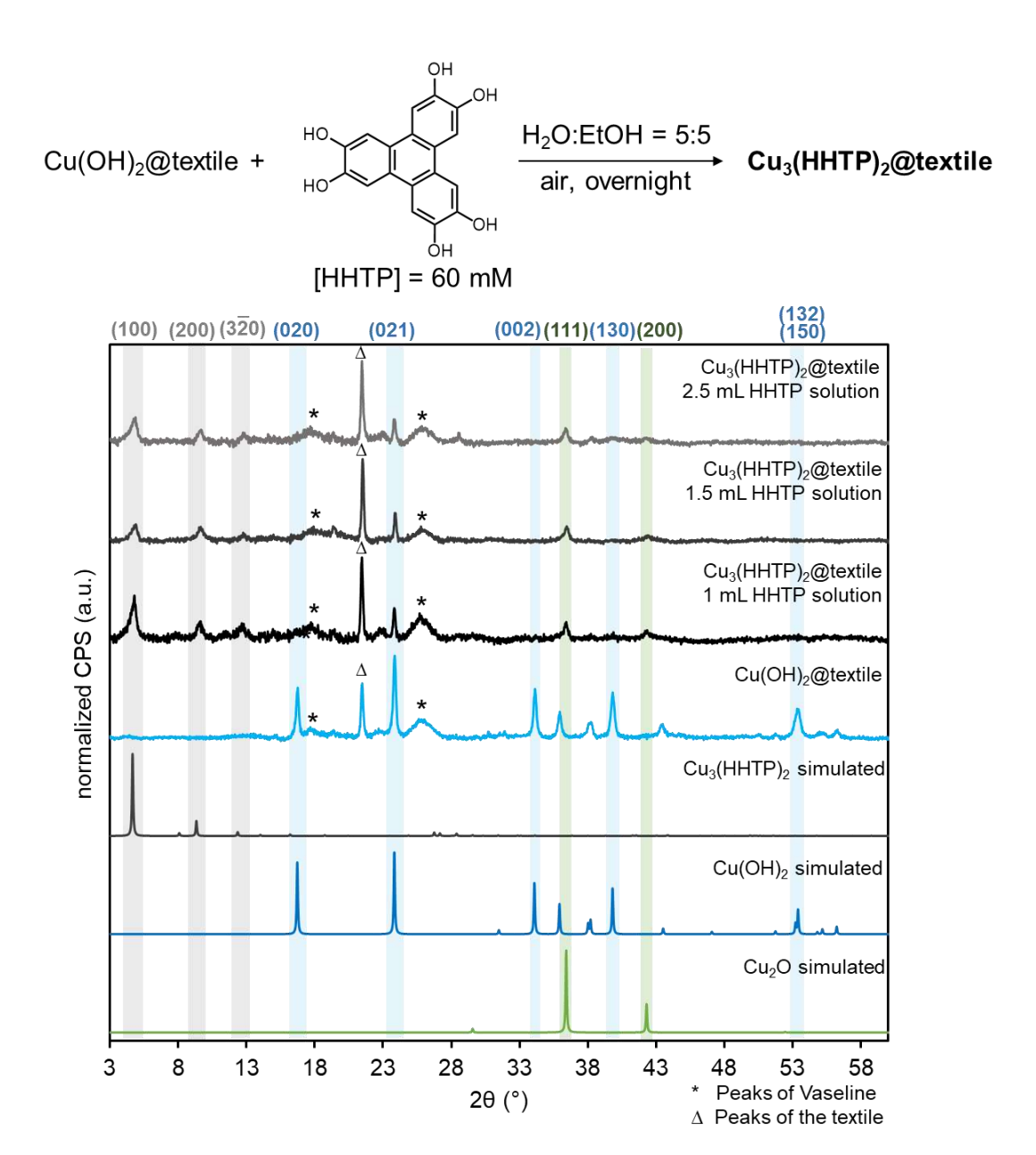


Figure S4. PXRD analysis and photographs of Cu₃(HHTP)₂@textile using varied volumes of 60mM HHTP stock solution. The disappearance of peaks corresponding to the (020), (002), (130) planes of Cu(OH)₂ on textile swatch indicates the complete conversion from Cu(OH)₂@textile to Cu₃(HHTP)₂@textile of trials under all conditions. 1 mL of 60 mM HHTP stock solution was employed as the optimal volume for full conversion of Cu₃(HHTP)₂@textile.

2. Characterization studies

2.1 Scanning electron microscopy and energy dispersive X-ray spectroscopy

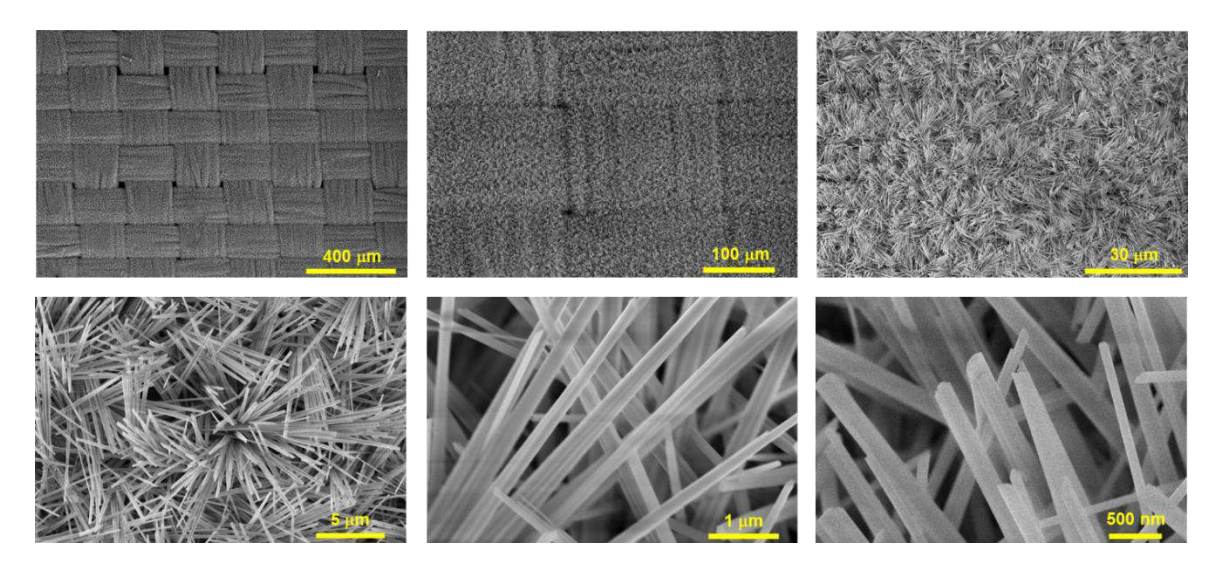


Figure S5. Scanning electron micrographs of Cu(OH)₂@textile after 0.5 h of the optimal reaction time. Conditions for all SEM images were an accelerating voltage of 5.00 kV, a working distance of 4.0 mm, a vacuum level of 10⁻⁶ torr, and a magnification of 250–150,000 X. The samples were mounted onto conductive carbon tape.

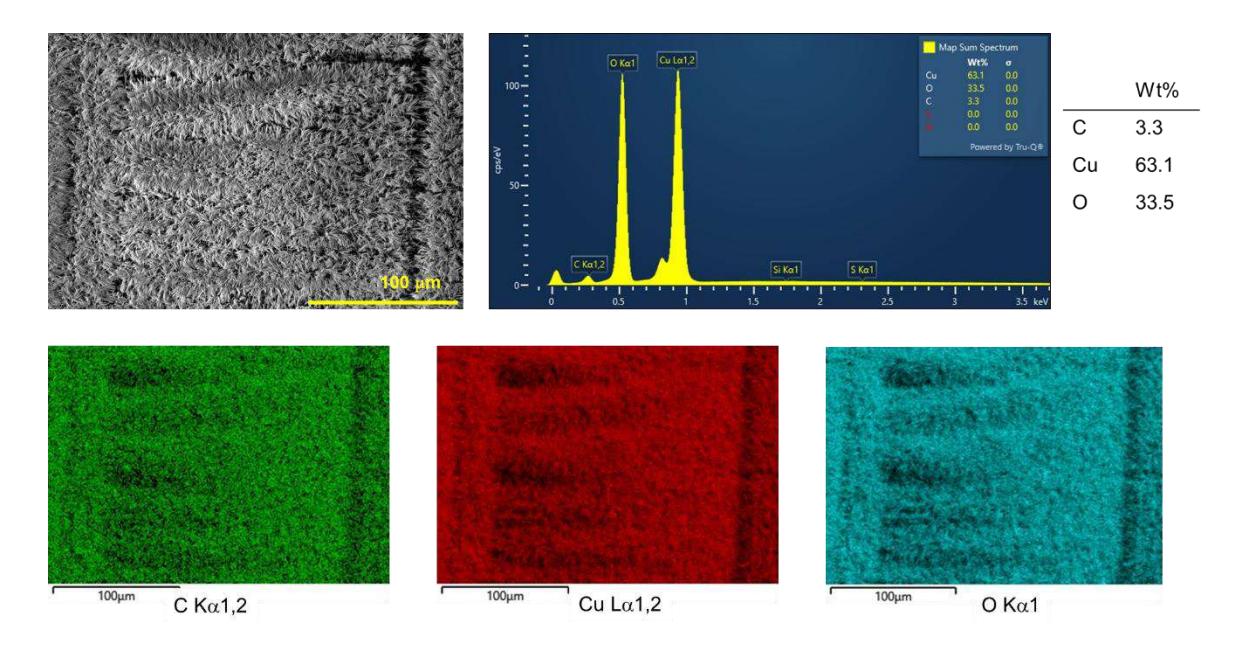


Figure S6. Representative scanning electron micrographs and energy dispersive X-ray spectroscopy (EDX) images of the surface of Cu(OH)₂@textile with three characteristic X-rays for C, O, and Cu. The EDX spectrum of the mapped Cu(OH)₂@textile confirms and quantifies the presence of C, O, and Cu. Conditions for all EDX images were accelerating

voltage of 10 keV, the working distance of 4 mm, a vacuum level of 10⁻⁶ torr, and a magnification of 10,000 X. The samples were mounted onto conductive carbon tape.

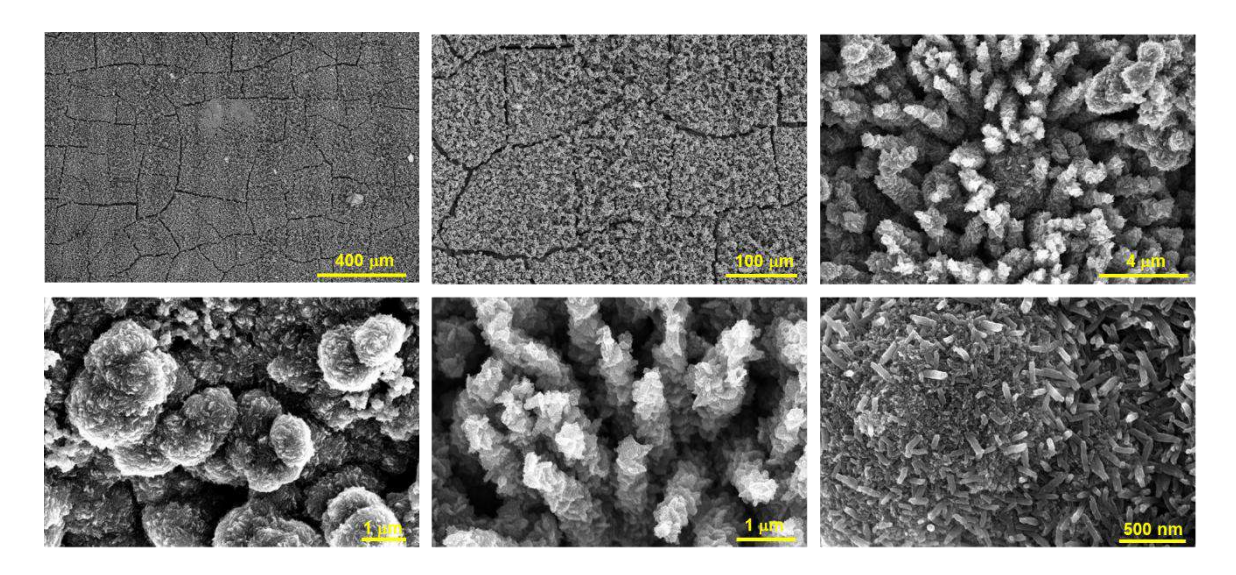


Figure S7. Scanning electron micrographs of Cu₃(HHTP)₂@textile after 0.5 h of reaction time.

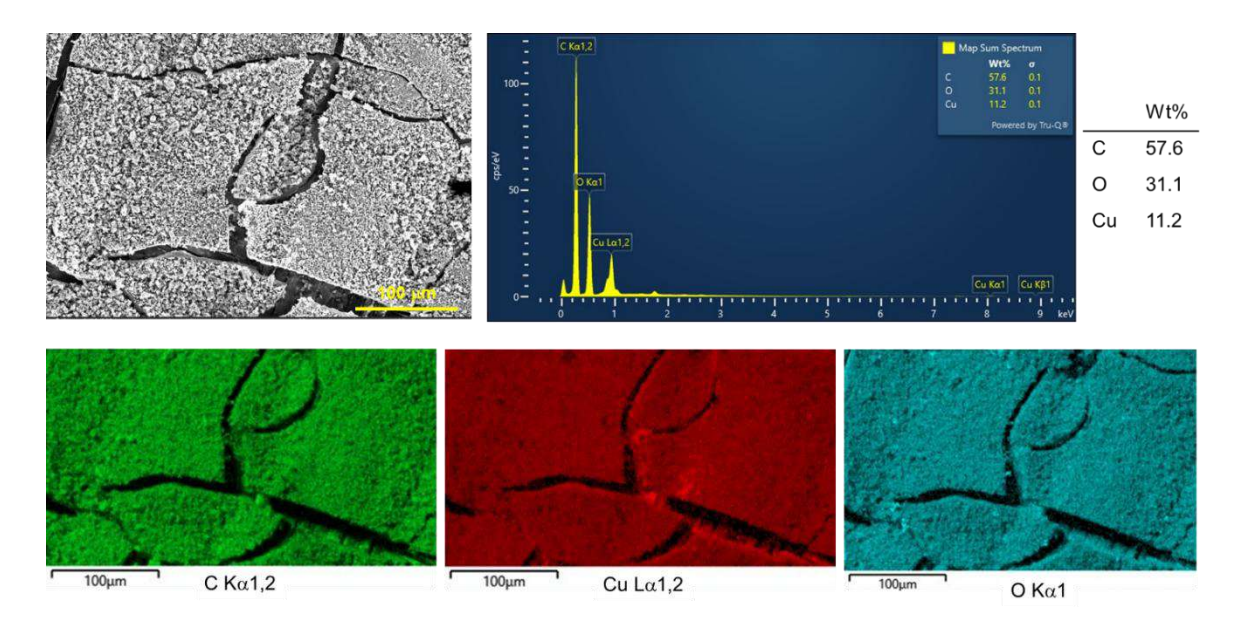


Figure S8. Representative scanning electron micrographs and EDX images of the surface of Cu₃(HHTP)₂@textile with three characteristic X-rays for C, O, and Cu. The EDX spectrum of the mapped Cu₃(HHTP)₂@textile confirms and quantifies the presence of C, O, and Cu.

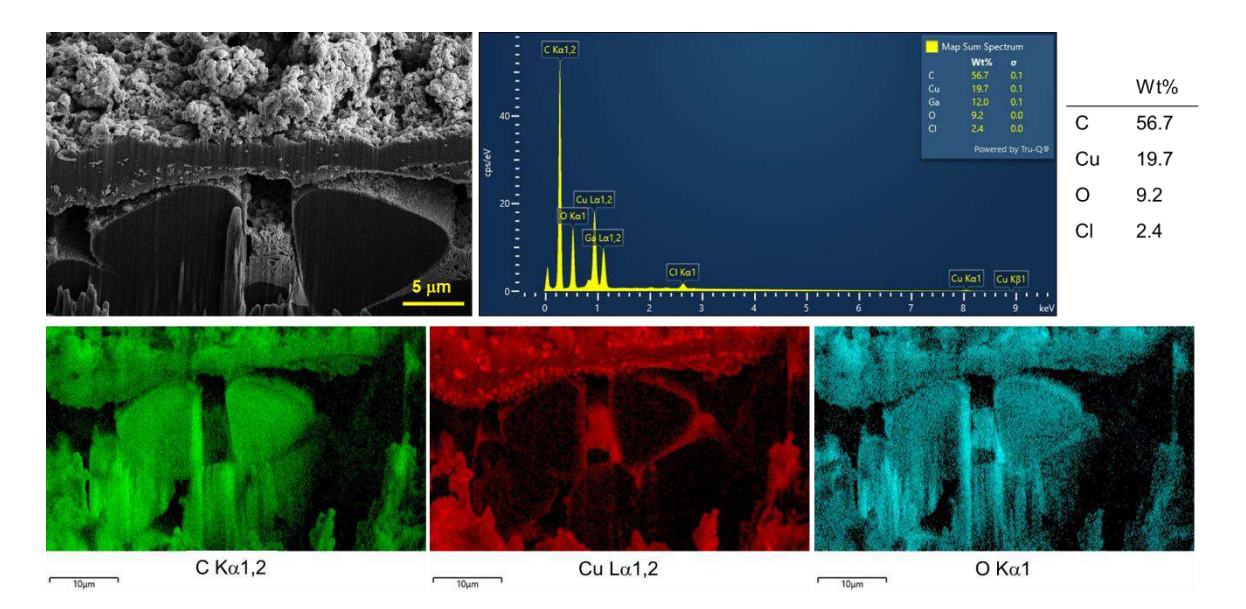


Figure S9. Representative scanning electron micrographs and EDX images of the cross-sectional face of $Cu_3(HHTP)_2$ @textile with three characteristic X-rays for C, O, and Cu. The cross section was generated using focused ion beam. The cross-sectional images of $Cu_3(HHTP)_2$ @textile showed that the thickness of the layer of $Cu_3(HHTP)_2$ was 7 μm .

2.2. ICP-MS analysis

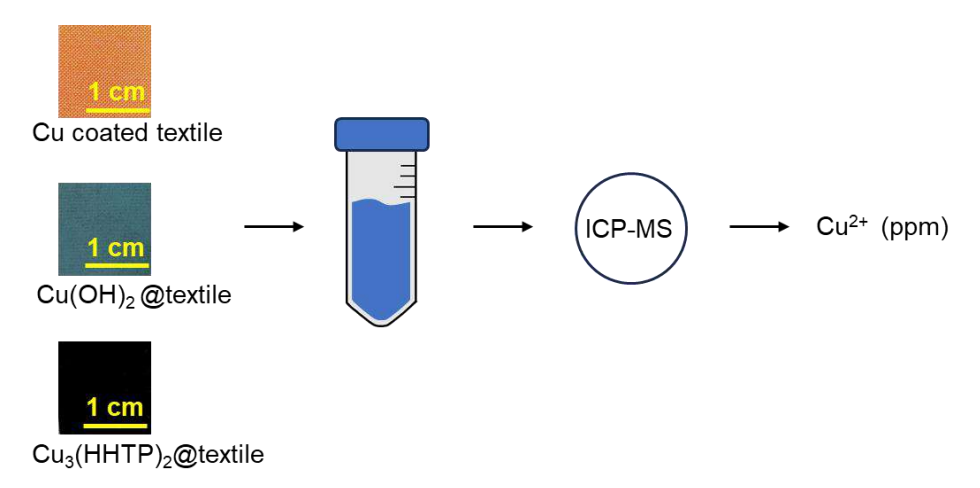


Figure S10. ICP-MS characterization of Cu²⁺ after fully dissolving the textile swatches in 98% sulfuric acid under 100 °C and diluting the solution to 0.2 g/mL with deionized water.

Table S1. ICP-MS analysis for Cu-coated textile, Cu(OH)₂@textile, Cu₃(HHTP)₂@textile in the two-step templated fabrication on four parallel trials.

Sample	Trial	Concentration of Cu ²⁺ in 0.2 g/L diluted solution (ppm)		Reaction yield (%)	Weight percentage of semiconductor in the textile (%)	
	1	62.3	65.2 ± 2.87	N/A		
Cu-coated textile	2	62.3			32.6 ± 1.43	
	3	68.4			32.0 ± 1.43	
	4	67.6				
	1	27.2	29.2 ± 2.12	.12 44.9 ± 3.57 22.4 ± 1.63		
Cu(OH) @toytilo	2	27.0			44.0 ± 2.57	22.4 ± 1.62
Cu(OH) ₂ @textile	3	31.2			22.4 ± 1.03	
	4	31.5				
	1	15.9				
Cu (UUTD) @toytilo	2	15.6	17.15 ± 1.42 58.7 ±	E9.7 + 2.55	37.9 ± 3.13	
Cu ₃ (HHTP) ₂ @textile	3	18.8		56.7 ± 2.55		
	4	18.3				

Reaction yield was determined according to Equation 1. Weight percentage (wt.%) of Cubased semiconductors in the semiconductor/textile was determined according to Equation 2. The solution of Cu-coated textile, Cu(OH)₂@textile, Cu₃(HHTP)₂@textile was diluted to 0.2g/L.

Reaction yield (%) =
$$\frac{Concentration\ of\ Cu^{2+}\ in\ diluted\ produt\ solution}{Concentration\ of\ Cu^{2+}\ in\ diluted\ reactant\ solution} \times 100$$
 Equation 1

Weight percentage of semiconductor in the textile (%) =
$$\frac{Concentration\ of\ Cu^{2+}\ in\ diluted\ solution\ \times molar\ mass\ of\ semiconductor}{molar\ mass\ of\ Cu^{2+}\times concentration\ of\ the\ diluted\ solution} \times 100$$
 Equation 2

2.3. Control over Cu₃(HHTP)₂ growth on the textile by varying reaction time

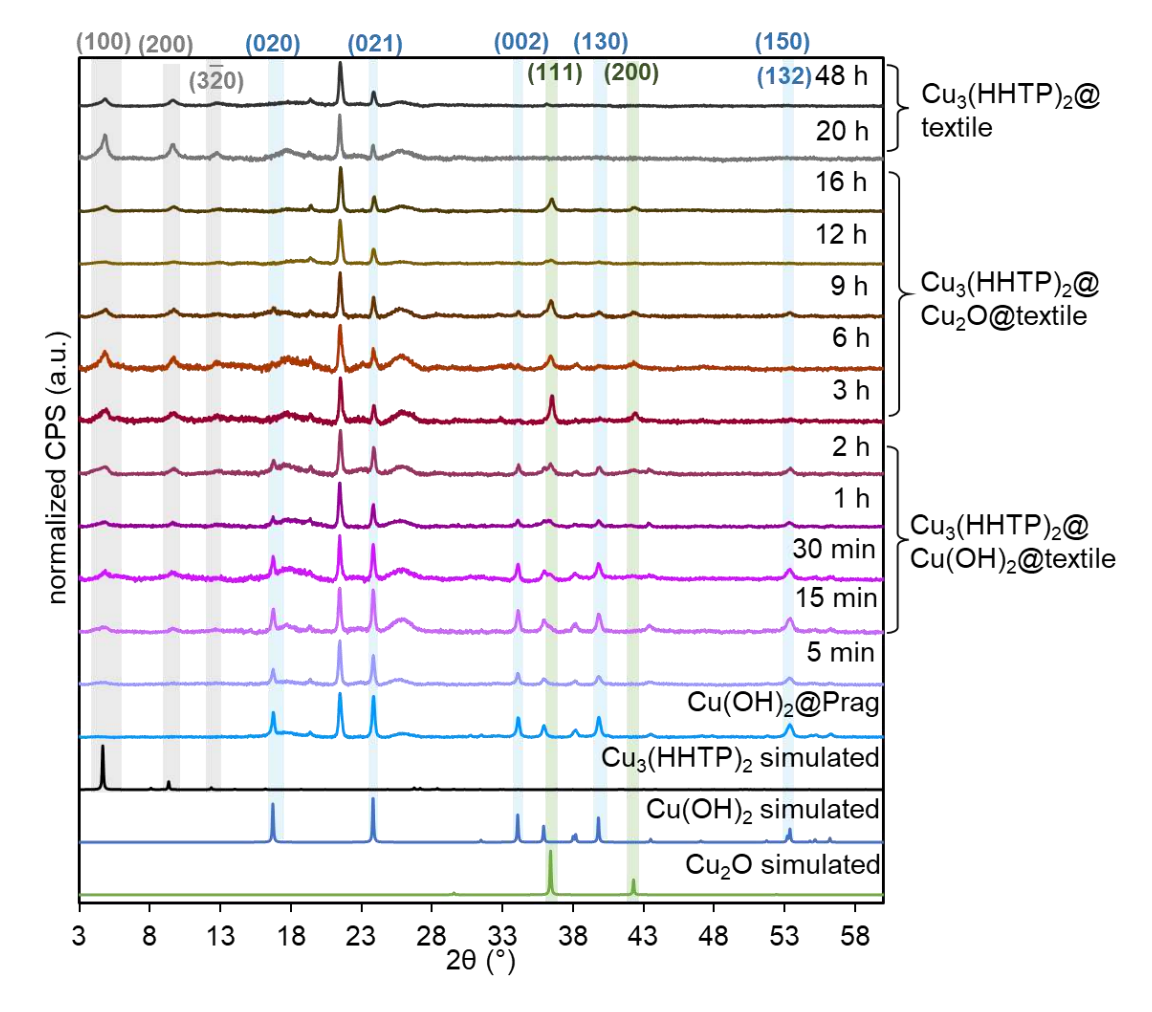


Figure S11. PXRD analysis of Cu₃(HHTP)₂@textile over varying time points from 5 min to 48 h. The growth of Cu₃(HHTP)₂ on textile swatches was stopped by taking the swatches out of the HHTP stock solution and washing the swatches with ethanol, water, and acetone three times, and dried under vacuum.

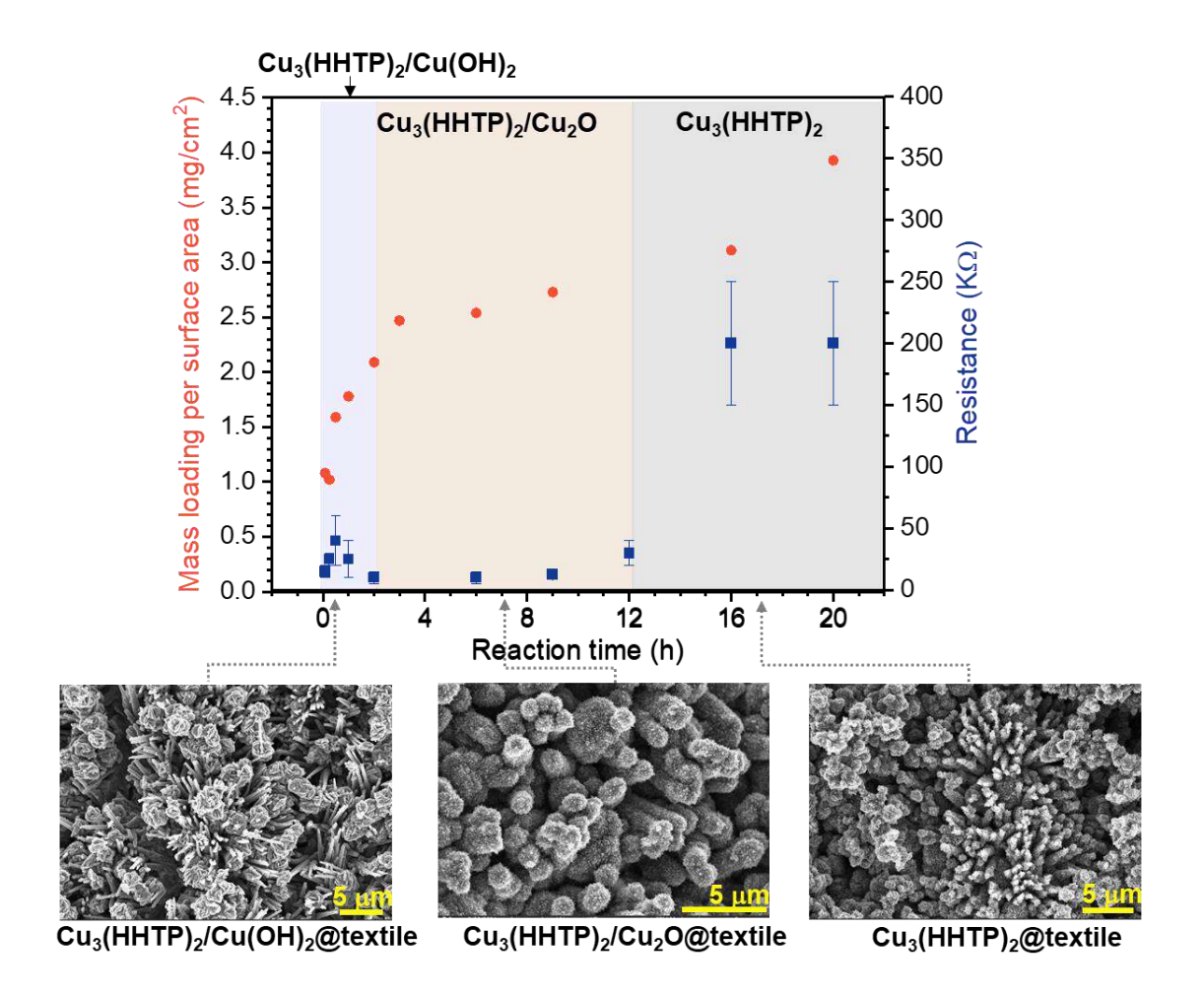


Figure S12. Impacts of reaction time on the mass loading, resistance, and morphological evolution of semiconductors on the textile from 5 min to 20 h. Red circles represent Cu₃(HHTP)₂ mass loading per surface area on fabric swatches. Green squares and error bars represent the resistance range of Cu₃(HHTP)₂@textile.

Table S2. Mass loading calculation of Cu₃(HHTP)₂ per surface area throughout the reaction.

Reaction time	Textile (mg)	Cu(OH)₂@textile (mg)	Cu₃(HHTP)₂@textil e (mg)	Mass of Cu ₃ (HHTP) ₂ (mg)	Mass of Cu ₃ (HHTP) ₂ per surface area (mg/cm²)
5 min	16.6	16.8	18.5	2.65	1.18
15 min	16.0	17.3	18.9	2.49	1.11
30 min	15.7	16.3	18.8	3.90	1.73
1 h	15.2	16.2	19.0	4.36	1.94
2 h	16.4	16.9	20.2	5.14	2.28
3 h	14.2	15.2	19.1	6.08	2.69
6 h	14.5	15.8	19.8	6.23	2.77
9 h	15.6	15.8	20.1	6.70	2.98
12 h	15.4	16.0	20.1	6.38	2.84
16 h	15.0	15.2	20.1	7.63	3.39
20 h	14.4	16.3	22.5	9.66	4.29
48 h	15.8	16.9	24.2	11.37	5.05

The dimension of the textile swatches is 1.5 cm \times 1.5cm. The mass of Cu₃(HHTP)₂ on textile per surface area was determined according to Equation 3. The reaction yield of 58.7% was adopted from ICP-MS analysis.

$$mass\ of\ Cu_3(HHTP)_2\ per\ surface\ area\ =\ \frac{mass\ of\ Cu_3(HHTP)_2\ on\ Prag\ -\ mass\ of\ Cu(OH)_2\ on\ Prag\ }{surface\ area\ of\ swatch}\ \times$$

$$\frac{1}{reaction\ yield}\times \frac{molecular\ weight\ of\ Cu_3(HHTP)_2}{molecular\ weight\ of\ Cu_3(HHTP)_2\ -\ molecular\ weight\ of\ Cu(OH)_2}$$
 Equation 3

Table S3. 2-Point probe measurements of the sheet resistance and conductivity of the MOF on textiles at set time points.

Time	Sheet Resistance (R_s)	Conductivity (σ)	Composition	
48 h	$0.1-0.2~\mathrm{M}\Omega$	0.050 - 0.10 S/m		
20 h	$0.1-0.3~\text{M}\Omega$	0.033 - 0.10 S/m	Cu ₃ (HHTP) ₂ @textile	
16 h	$0.1-0.3~\text{M}\Omega$	0.033 - 0.10 S/m		
12 h	30 – 45 KΩ	0.25 – 0.50 S/m		
9 h	$10-40~\text{K}\Omega$	0.50 - 2.0 S/m	Cu ₃ (HHTP) ₂ @	
6 h	5 – 15 KΩ	0.67 – 2.0 S/m	Cu ₂ O@textile	
4 h	$10 – 50$ Κ Ω	0.14 - 1.0 S/m		
2 h	4 – 15 ΚΩ	0.25 – 0.67 S/m		
1 h	$10-40~\text{K}\Omega$	0.25 - 1.0 S/m	Cu ₃ (HHTP) ₂ @	
30 min	$20-40~\text{K}\Omega$	0.17 - 0.50 S/m	Cu(OH) ₂ @textile	
15 min	$20-30~\text{K}\Omega$	0.33 - 0.50 S/m		
5 min	10 – 20 KΩ	0.50 – 1.0 S/m	Cu(OH) ₂ @textile	

The conductivity (σ) of the MOF/textile was determined according to Equation 4. The thickness (T) of the textile swatch was measured 100 μ m.

$$\sigma = \frac{1}{\rho} = \frac{L}{R \times A} = \frac{L}{R \times W \times T} = \frac{1}{R_S \times T}$$
 Equation 4

2.4. Stability tests

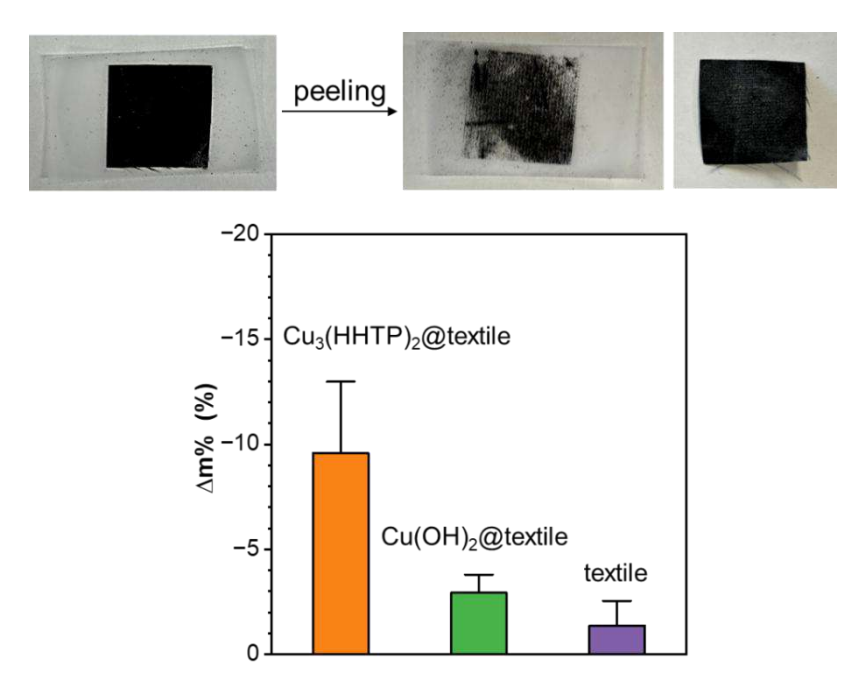


Figure S13. Scotch tape test and photographs of textile swatches. A one-side scotch tape was applied on the 1.5cm \times 1.5cm swatch, and the percentage mass differences (Δ m%) of the tape and textiles were measured and calculated before and after the peeling experiment.

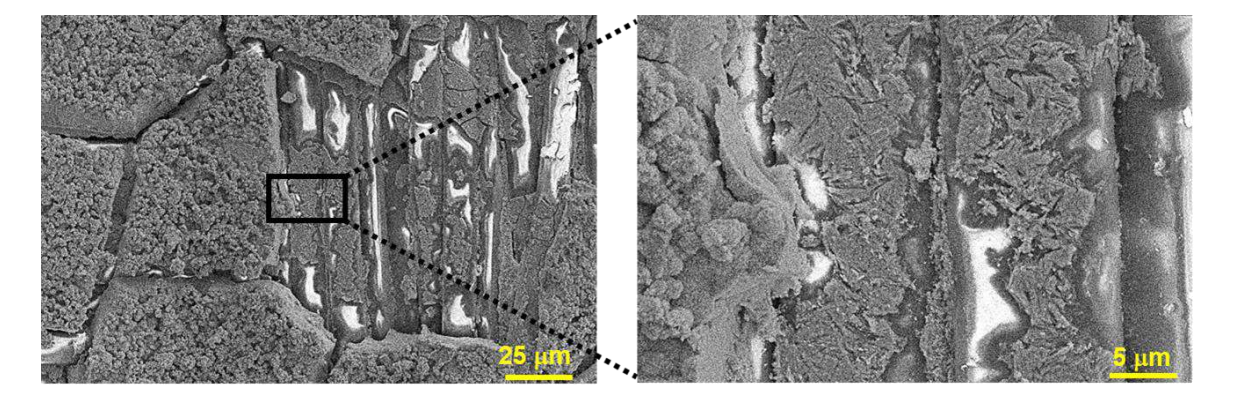


Figure S14. Representative scanning electron micrographs of Cu₃(HHTP)₂@textile after single-tape peeling test and the partial loss of the MOF aggregates.

2.5. Brunauer–Emmett–Teller analysis

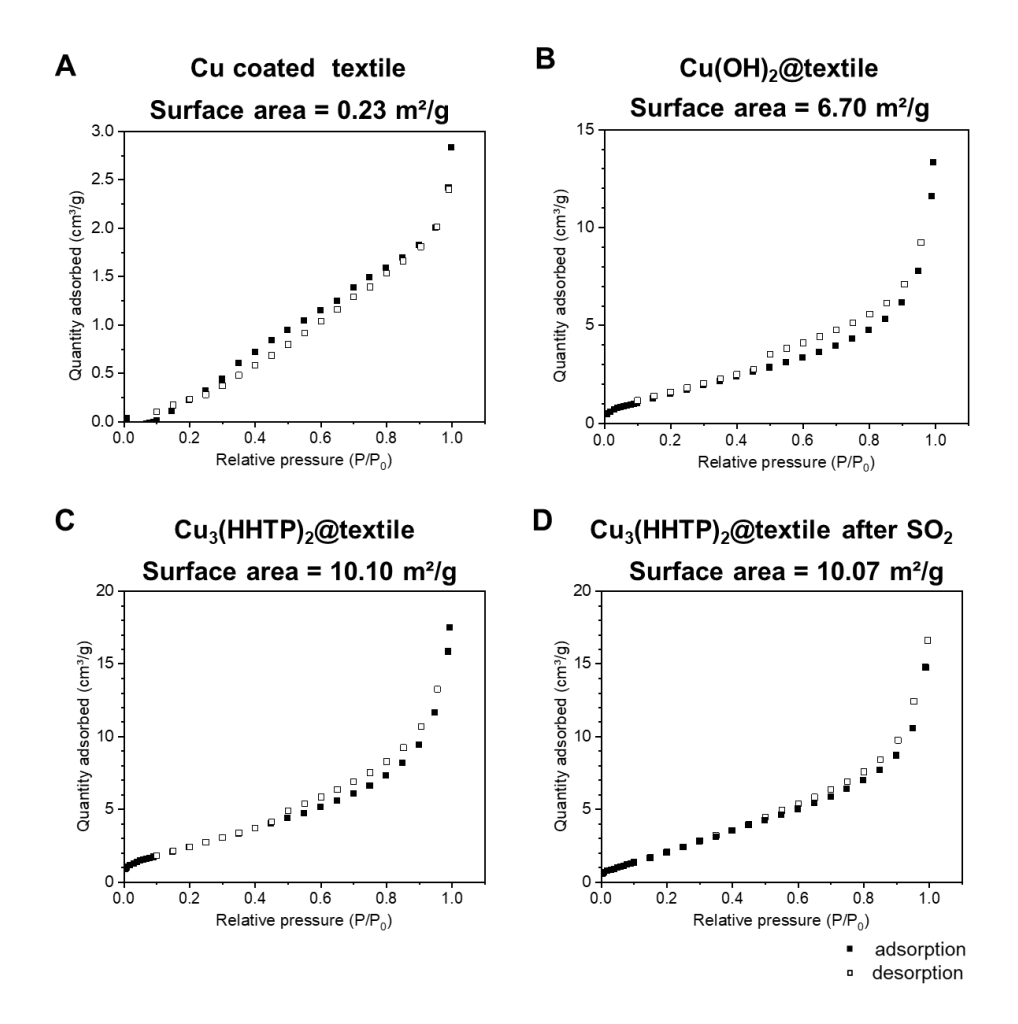


Figure S15. Nitrogen adsorption isotherms at 77 K for (A) bare textile, (B) Cu(OH)₂@textile, (C) Cu₃(HHTP)₂@textile, and (D) Cu₃(HHTP)₂@textile after a 30-minute exposure to 1% SO₂ in N₂. For activation, Cu₃(HHTP)₂@textile after 1% SO₂ exposure was degassed under vacuum overnight at 80 °C before BET analysis. Other textile devices (60 – 80 mg) were submerged in acetone for 2 days and vacuum dried at 80 °C for 2 days before BET analysis.

2.6. Thermogravimetric analysis

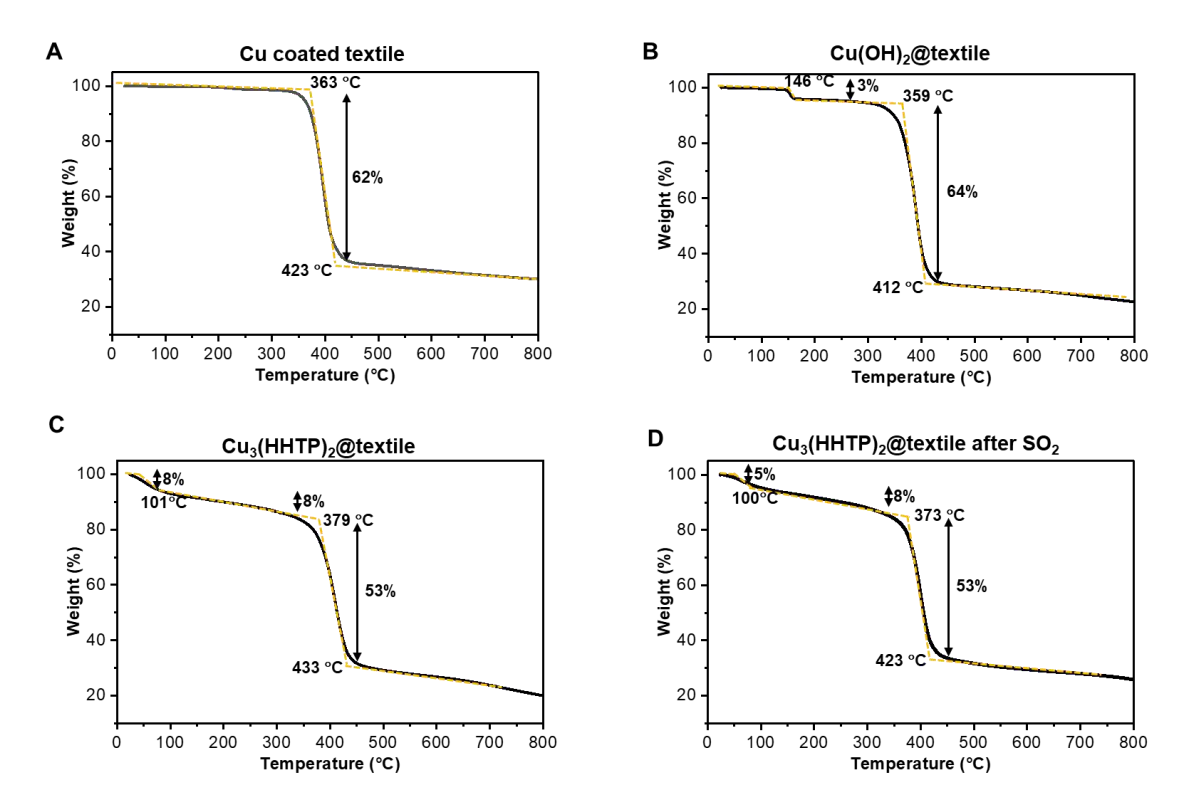


Figure S16. TGA analysis of (A) Cu coated textile (B) Cu(OH)₂@textile, (C) pristine Cu₃(HHTP)₂@textile, and (D) Cu₃(HHTP)₂@textile after a 30-minute exposure to 1% SO₂ in N₂. All samples were dried under vacuum overnight. For Cu coated textile, the polyester fabric degraded between 363 °C to 423 °C. Cu(OH)₂@textile underwent the decomposition of Cu(OH)₂ to CuO at around 146 °C, followed by polyester degradation.

Cu₃(HHTP)₂@textile before and after SO₂ exposure showed similar mass changes over temperature. A small weight loss (5–8%) due to the aqua ligand bound to the MOF occurred around 100 °C, followed with 8% and 53% mass loss ascribed to the degradation of HHTP linker and the fabric. Before SO₂ exposure, Cu₃(HHTP)₂@textile absorbed 8% water, which decreased to 5% after exposure. This 3% reduction indicates that the aqua ligand in Cu₃(HHTP)₂@textile participated in MOF-SO₂ interactions, as supported by the DRIFTS band at 860 cm⁻¹, corresponding to the O-H bending of hydrated sulfate.

2.7. Preparation and characterization of bulk Cu₃(HHTP)₂

0.2 mmol of 2,3,6,7,10,11-Hexahydroxytriphenylene (HHTP, 1 eq.) and 0.3 mmol of Cu(OH)₂ (1.5 eq.) were dispersed in a 10 mL of a 1:1 mixtures of DI water/ethanol and sonicated for 10 mins. 20 mmol of concentrated ammonia solution (100 eq. relative to HHTP) was added dropwise to the resulting solution, which was then capped, and heated at 75 °C for 14 hours. The resulting black powder was filtered, washed with DI water (20 mL), ethanol (25 mL), and acetone (25 mL), before being dried in a vacuum oven set at 75 °C for 16 hours.

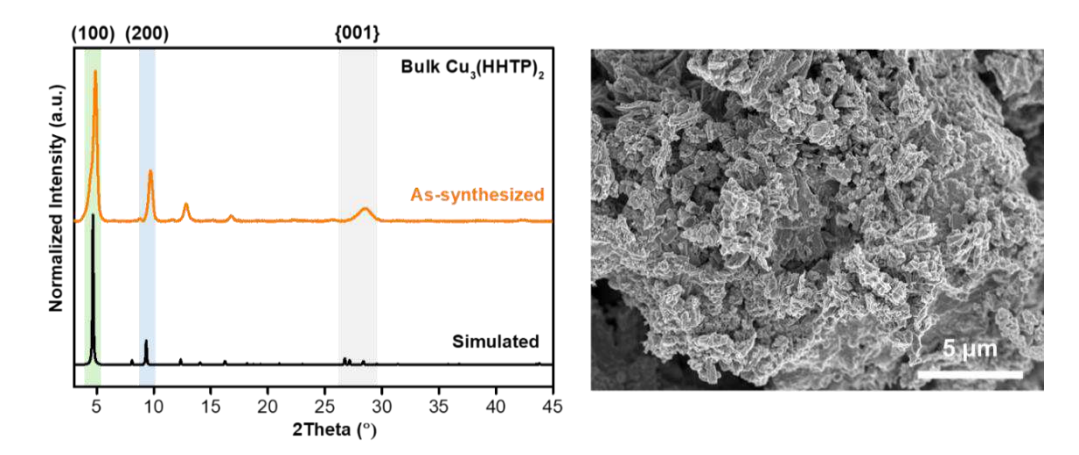


Figure S17. PXRD patterns and scanning electron micrograph of bulk Cu₃(HHTP)₂ prepared from Cu(OH)₂ using a similar solvothermal method.

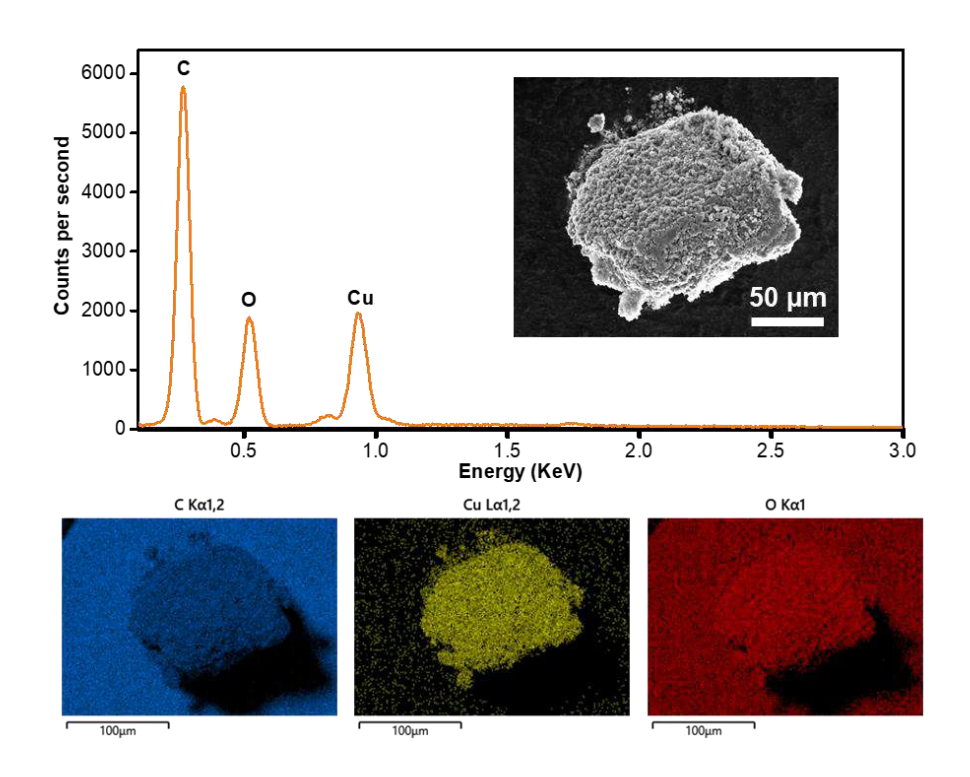


Figure S18. EDX spectrum and elemental mapping of bulk Cu₃(HHTP)₂ with characteristic X-rays for C, O, Cu.

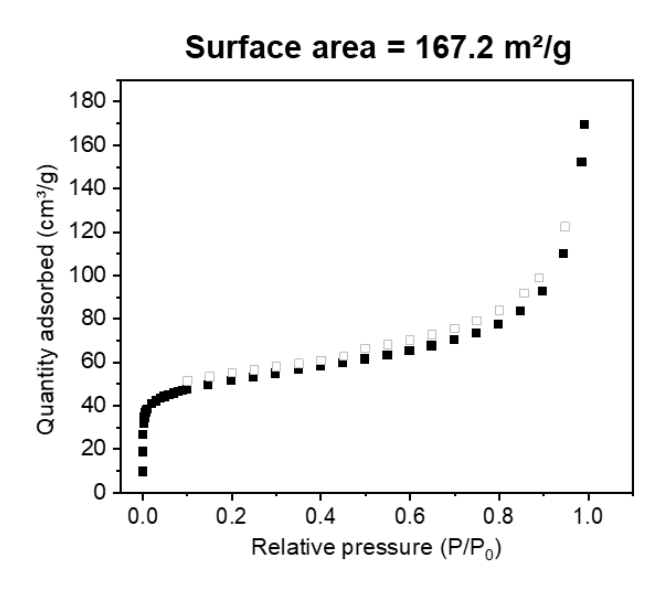


Figure S19. Nitrogen adsorption isotherms at 77 K for bulk Cu₃(HHTP)₂ prepared from Cu(OH)₂. For activation, the MOF samples (50 mg) was submerged in acetone for 2 days and vacuum dried at 80 °C for 2 days before BET analysis.

3. Gas sensing experiments

3.1. Experiment and device setup

The sensing performance of the MOF-based textile devices (1.5 cm \times 0.5 cm) was monitored in a sealed Teflon gas-sensing chamber under room temperature. ^{2, 3} An electrical feed-through and gas inlet and outlet were installed in the chamber. Dry and humid, N2 and air atmospheres were used as the balance gas. Devices used for sensing were equilibrated with the balance gas overnight or 4 h at a flow rate of 0.5 L/min before any sensing experiments. A Sierra Micro-Trak and a Smart-Trak mass flow controller were used in combination to deliver controlled concentrations of gas analytes from custom-ordered premixed tank(s) equipped with two-stage stainless steel regulators. SO₂ stream (1% or 10,000 ppm SO₂ in dry N₂) was delivered from the tank and further diluted with the delivery gas (N₂, air, humid N_2 (Relative humidity (RH) = 90%), and humid air (RH = 90%) for a defined gas dosing across the textile devices, ranging from 5 – 100 ppm. The concentrations of the gas analytes were adjusted by controlling the flow rates of the target gas while the delivery gas was fixed at 0.5 L/min; this was achieved using two mass flow controllers. The humidified stream of N₂ and air were produced by the gas generator embedded with a vial of deionized water, mass flow and temperature controllers, and a humidity sensor. By fixing the flow rate at 0.5 L/min, we reached the deliverable ppm of water vapor within the balance gas of N₂ or air. The vapor stream was mixed with SO₂ stream delivered by the mass flow system using a Y-connection. The relative humidity of the mixed streams was calculated as 90%.

Swatches of $\text{Cu}_3(\text{HHTP})_2$ @textile and $\text{Cu}(\text{OH})_2$ @textile were cut into 1.5 cm \times 0.5 cm pieces and contacted with gold pins in the sensing apparatus chamber which serve as ohmic contacts. Sensing apparatus electrodes connected to a breadboard and potentiostat for gas detection, a gas inlet and outlet on the sensing apparatus chamber allow for gas to flow through the enclosure. Chemiresistive devices of powder samples were made by dropcasting 20 μ L of semiconductor suspensions in deionized water (1 mg mL⁻¹) onto interdigitated gold electrodes (gap 5 μ m, Metrohm product # G-IDEAU5). Each device was

subjected to three dosing cycles: baseline in the delivery gas (15 minutes), dose with SO_2 (1 h, shown in gray), and recovery in the delivery gas (1 h). The sensing performance of each device was assessed through the measurement of current under a constant applied voltage (1.0 V) with a PalmSense EmStatMUX potentiostat and a multiplexer. Raw current data (collected under constant applied voltage) was normalized and converted to normalized conductance according to Equation 5, wherein I_0 = initial current and I = current at different points during measurement.²

$$-\frac{\Delta G}{G_0} = -\frac{I - I_0}{I_0} \times 100\%$$
 Equation 5

3.2. Cyclic sensing experiments

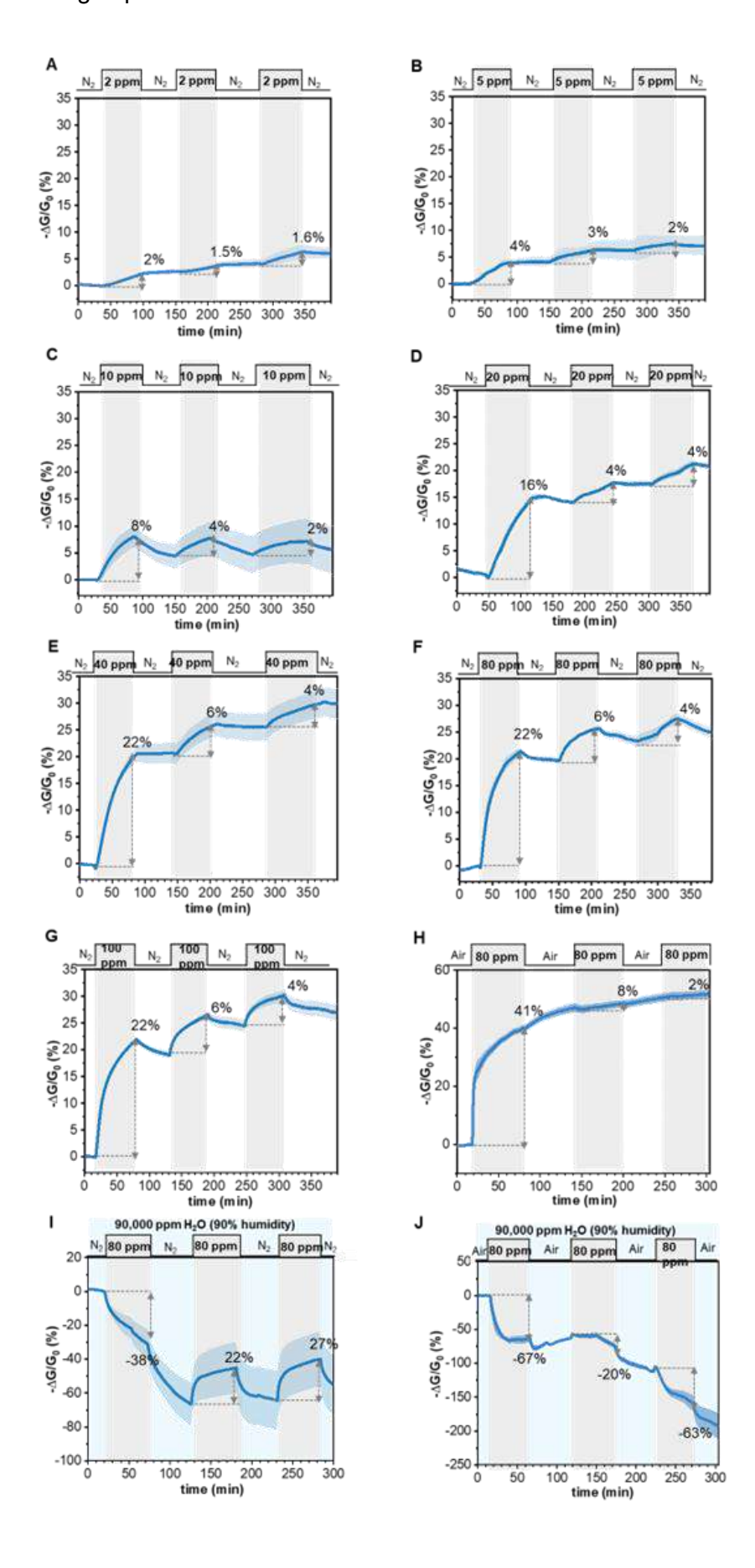


Figure S20. Chemiresistive sensing of $Cu_3(HHTP)_2$ @textile with 2–100 ppm SO_2 in N_2 . Three-cycle chemiresistive sensing responses of $Cu_3(HHTP)_2$ @textile devices with (A) 2 ppm, (B) 5 ppm, (C) 10 ppm, (D) 20 ppm, (E) 40 ppm, (F) 80 ppm, (G) 100 ppm SO_2 in N_2 atmosphere and three-cycle sensing responses of $Cu_3(HHTP)_2$ @textile devices with 80 ppm SO_2 in (H) air, (I) humid N_2 (RH = 90%), and (J) humid air (RH = 90%) atmospheres. Each cycle includes a baseline in the delivery atmosphere at a flow rate of 0.5 L/min before analyte exposure (1000 s) and exposure to target gas mixed with the delivery gas (60 min), followed by device recovery in the delivery atmosphere at a flow rate of 0.5 L/min. The sensing curves represent the average sensing responses from three parallel trials. The shading patterns indicate the standard deviation of sensing responses of these parallel trials.

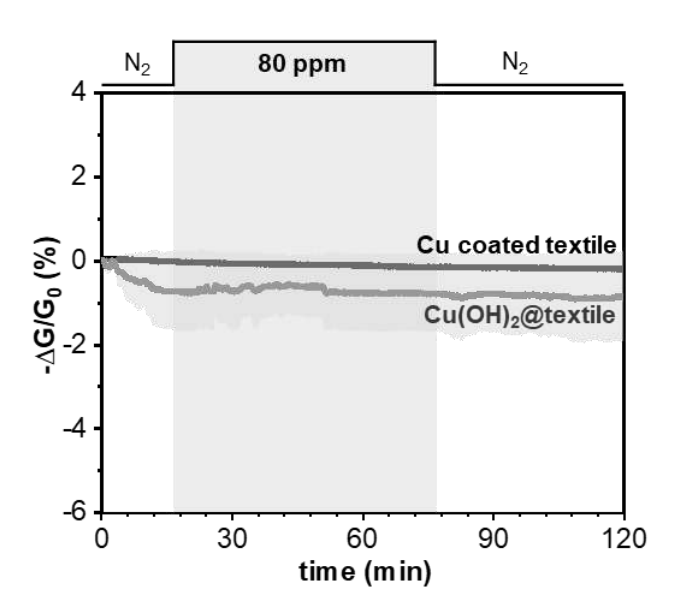


Figure S21. Sensing responses of Cu(OH)₂@textile (grey curve) and the original Cu coated textile (black curve) when exposed to 1-hour 80 ppm SO₂ in N₂ atmosphere.

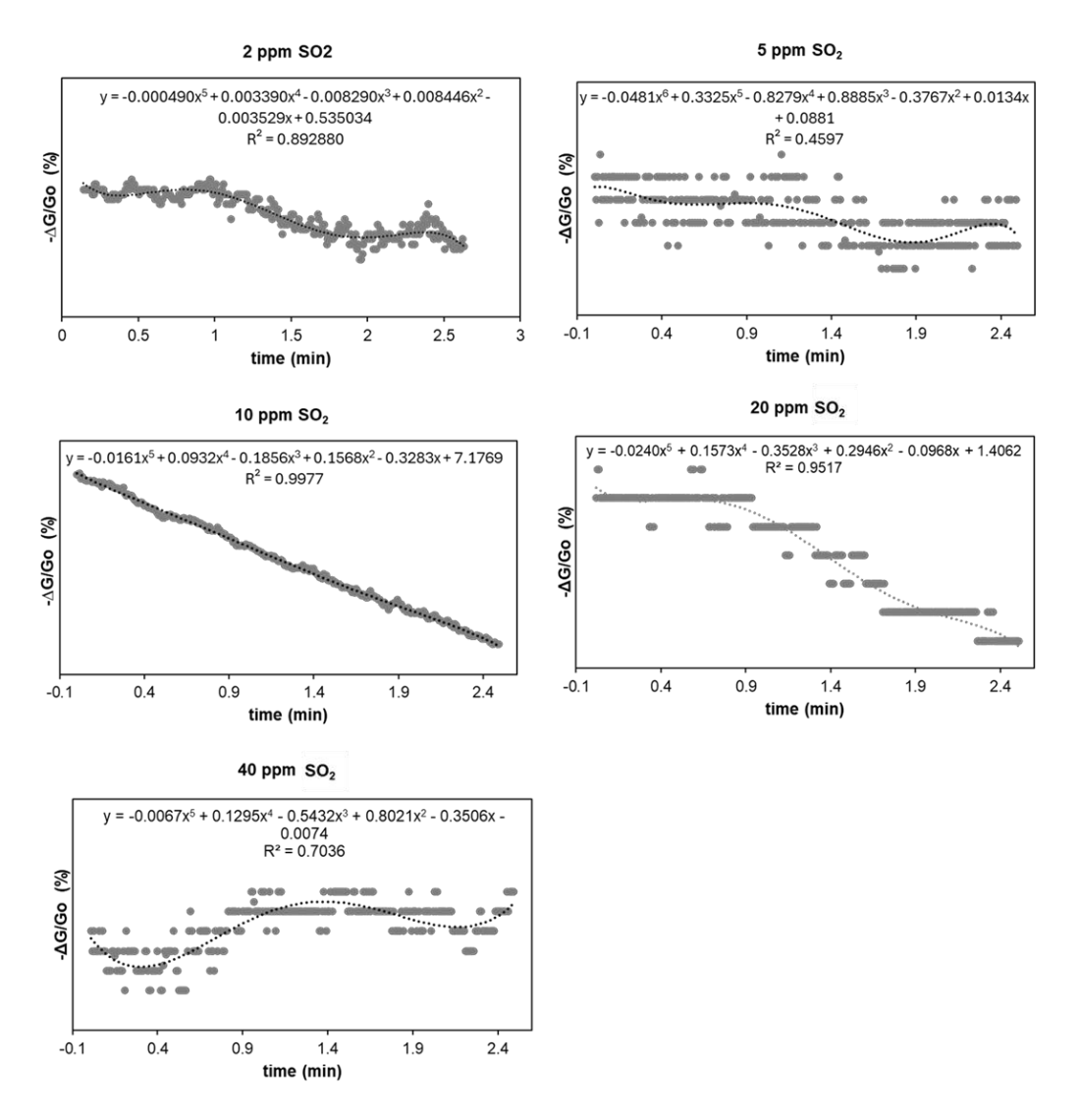


Figure S22. The extracted polynomial fitting of the sensing diagram with 2, 5, 10, 20, 40 ppm SO₂ for the analysis of LODs under different analyte dosage.

The theoretical LODs were calculated using the following protocol.³ First, we use the baseline trace before exposure to analyte and took the first 300 consecutive points (N = 300) and fit the data to a 5th order polynomial. We calculated V_{x2} from Equation 6, where y_i = measured - $\Delta G/G_o$ and y is the value calculated from the extracted polynomial fit. The root mean squared (rms) value of - $\Delta G/G_o$ was calculated from Equation 7. We calculated m by plotting the concentration of analyte versus the largest measured - $\Delta G/G_o$ in the first exposure cycle of analyte with the concentration range of 10 – 40 ppm to obtain the linear

relationship and the linear fitting equation, which provided the slope of the equation as m. With the values, the theoretical LOD was extrapolated from Equations 8.

$$V_{x^2} = \sum (y - y_i)^2$$
 Equation 6

 $rms = \sqrt{\frac{V_{x^2}}{N}}$ Equation 7

 $LOD = 3 \times \frac{rms}{m}$ Equation 8

Table S4. Theoretical LODs calculated for each $Cu_3(HHTP)_2$ @textile under various concentrations of SO_2 in N_2 atmosphere.

Gas sensing in N ₂ atmosphere	LOD	
Cu ₃ (HHTP) ₂ @textile under 2 ppm SO ₂	0.431 ppm	
Cu ₃ (HHTP) ₂ @textile under 5 ppm SO ₂	0.097 ppm	
Cu ₃ (HHTP) ₂ @textile under 10 ppm SO ₂	0.046 ppm	
Cu ₃ (HHTP) ₂ @textile under 20 ppm SO ₂	0.053 ppm	
Cu ₃ (HHTP) ₂ @textile under 40 ppm SO ₂	0.104 ppm	
Average LOD	0.146 ppm	

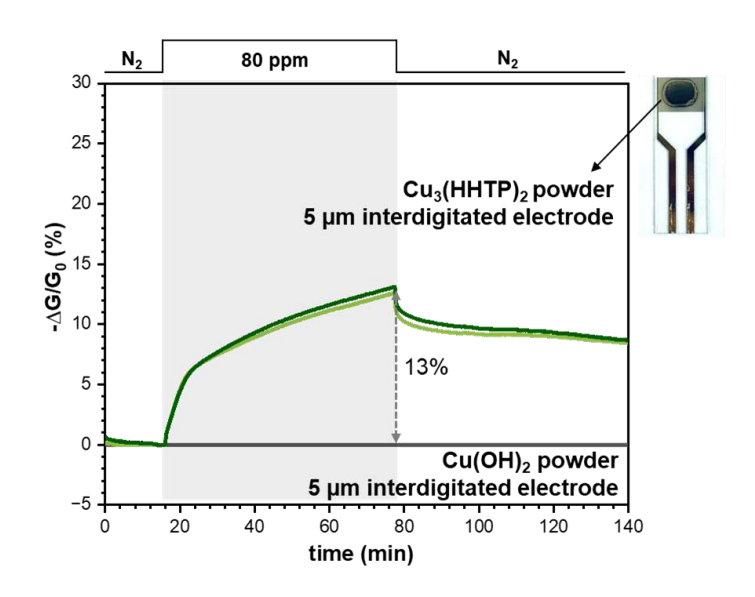


Figure S23. Chemiresistive sensing performances of Cu₃(HHTP)₂ (green curves) and Cu(OH)₂ (black curves) interdigitated electrodes towards 80 ppm SO₂ in N₂.

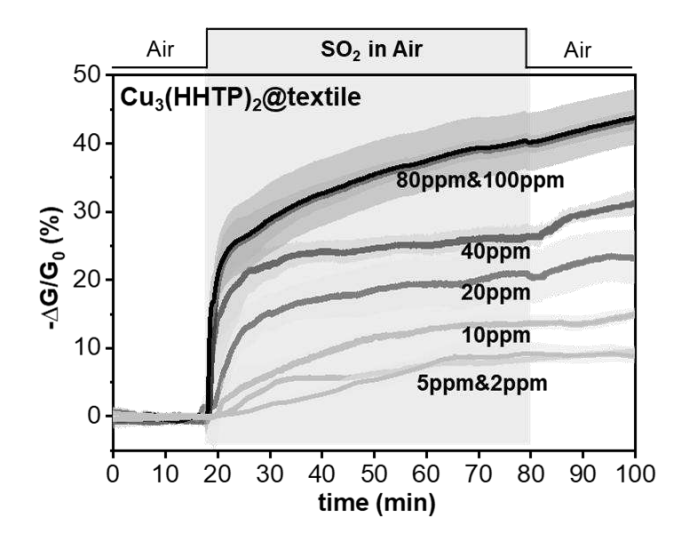


Figure S24. Chemiresistive sensing responses of Cu₃(HHTP)₂@textile devices with 2 ppm, 5 ppm, 10 ppm, 20 ppm, 40 ppm, 80 ppm and 100 ppm SO₂ in air atmosphere.

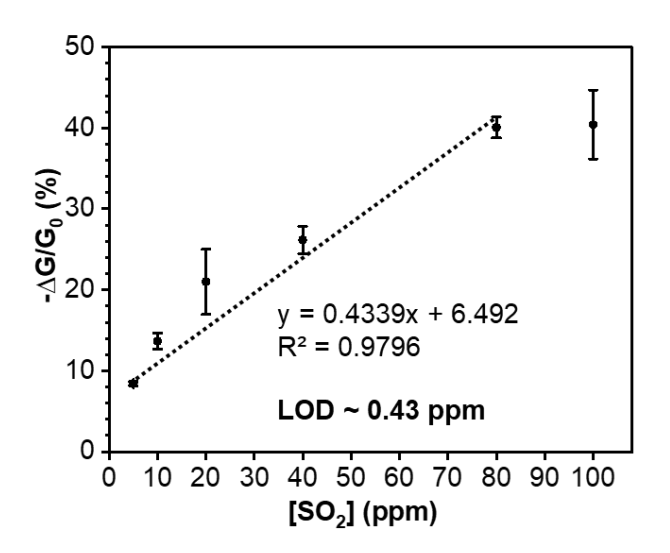


Figure S25. Linear range of maximum change in normalized conductance $(-\Delta G/G_0)$ versus SO_2 concentration (5–100 ppm) for $Cu_3(HHTP)_2$ @textile devices in air atmosphere.

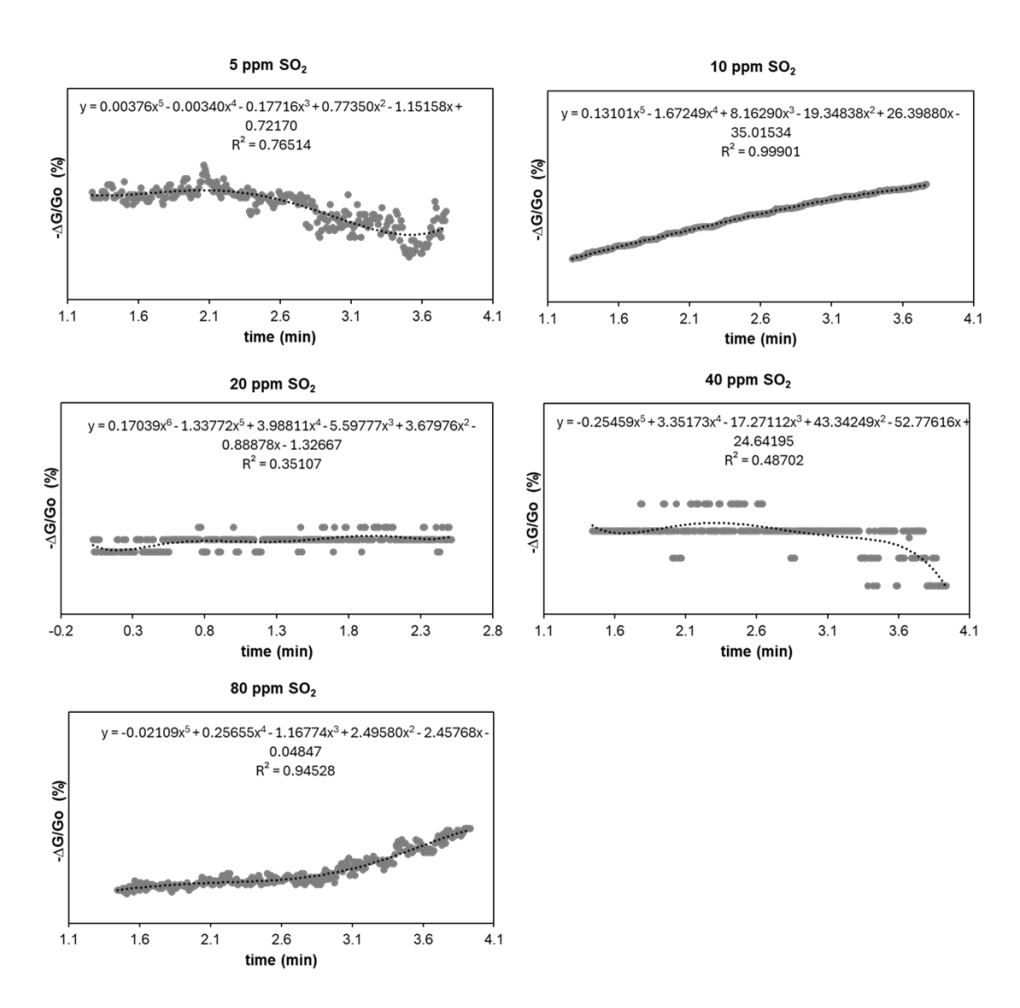


Figure S26. The extracted polynomial fitting of the sensing diagram with 5, 10, 20, 40, 80 ppm SO₂ for the analysis of LODs under different analyte dosage.

Table S5. Theoretical LODs calculated for each $Cu_3(HHTP)_2$ @textile under various concentration of SO_2 in air atmosphere.

Gas sensing in air atmosphere	LOD	
Cu ₃ (HHTP) ₂ @textile under 5 ppm SO ₂	0.180 ppm	
Cu ₃ (HHTP) ₂ @textile under 10 ppm SO ₂	0.560 ppm	
Cu ₃ (HHTP) ₂ @textile under 20 ppm SO ₂	0.359 ppm	
Cu ₃ (HHTP) ₂ @textile under 40 ppm SO ₂	0.890 ppm	
Cu ₃ (HHTP) ₂ @textile under 80 ppm SO ₂	0.148 ppm	
Average LOD	0.427 ppm	

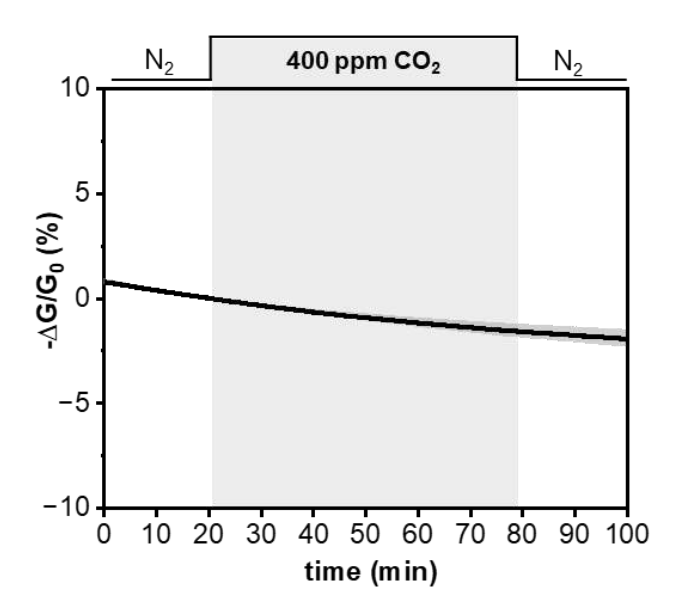


Figure S27. Chemiresistive responses of $Cu_3(HHTP)_2$ @textile devices sensing 400 ppm CO_2 in N_2 atmosphere.

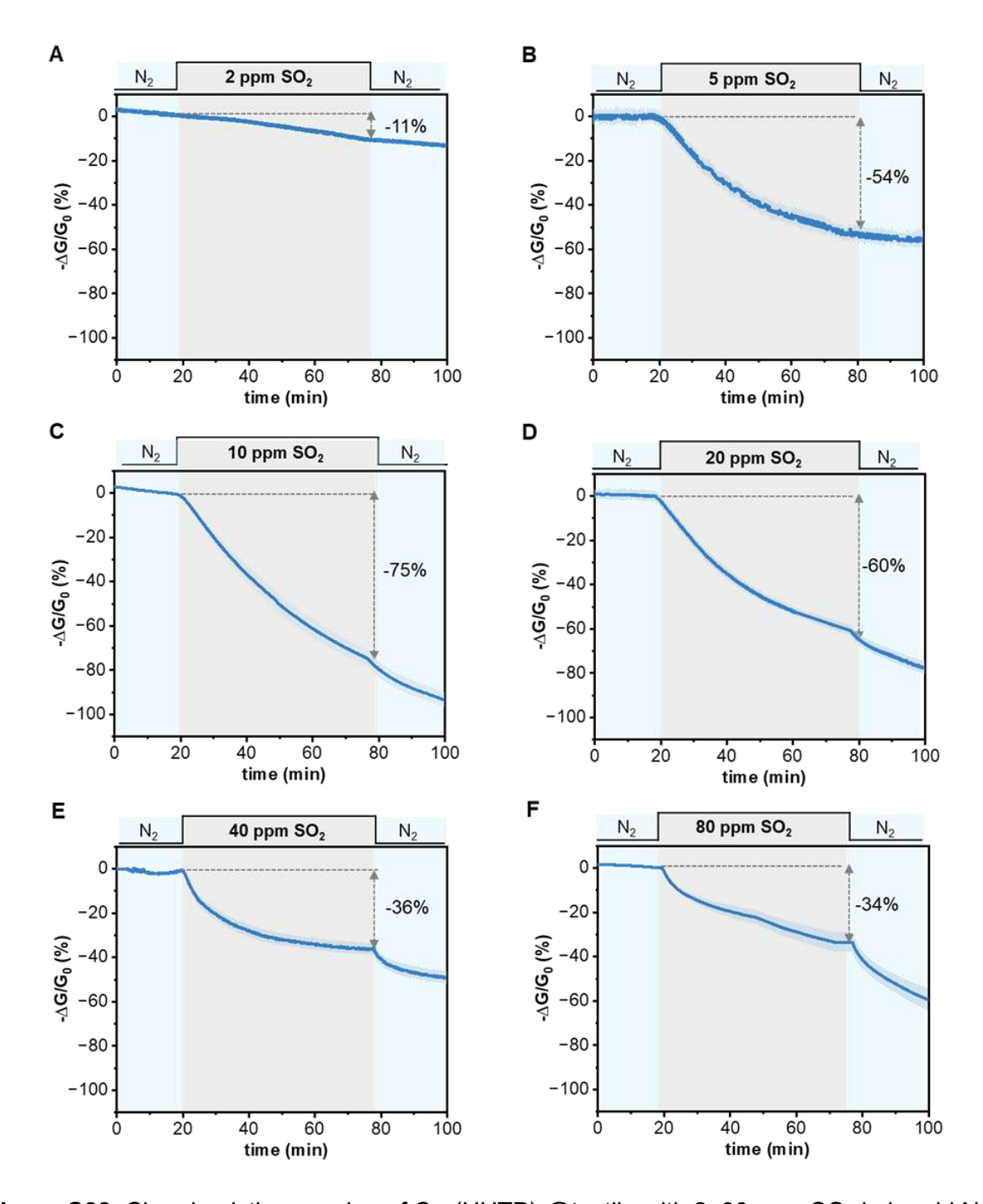


Figure S28. Chemiresistive sensing of $Cu_3(HHTP)_2$ @textile with 2–80 ppm SO_2 in humid N_2 . Chemiresistive sensing responses of $Cu_3(HHTP)_2$ @textile devices with (A) 2 ppm, (B) 5 ppm, (C) 10 ppm, (D) 20 ppm, (E) 40 ppm, and (F) 80 ppm SO_2 in humid N_2 (RH = 90%).

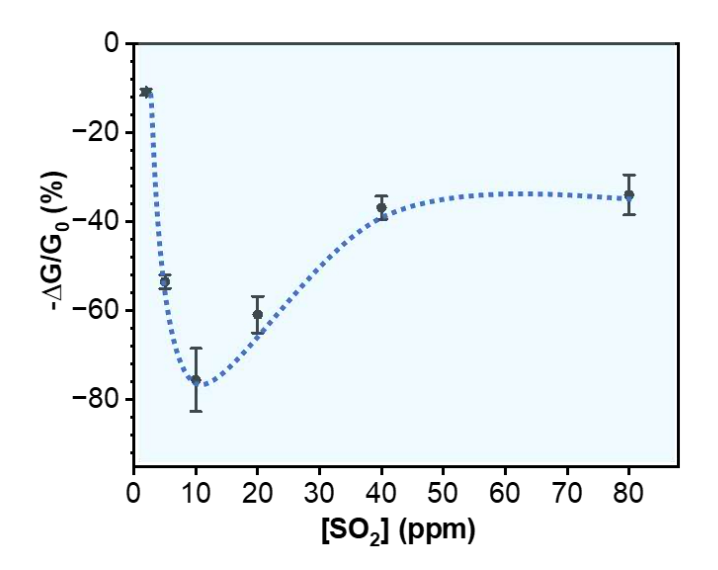


Figure S29. Non-linear range of maximum change in normalized conductance $(-\Delta G/G_0)$ versus SO_2 concentration (2-80 ppm) for $Cu_3(HHTP)_2$ @textile devices in humid N_2 (RH = 90%).

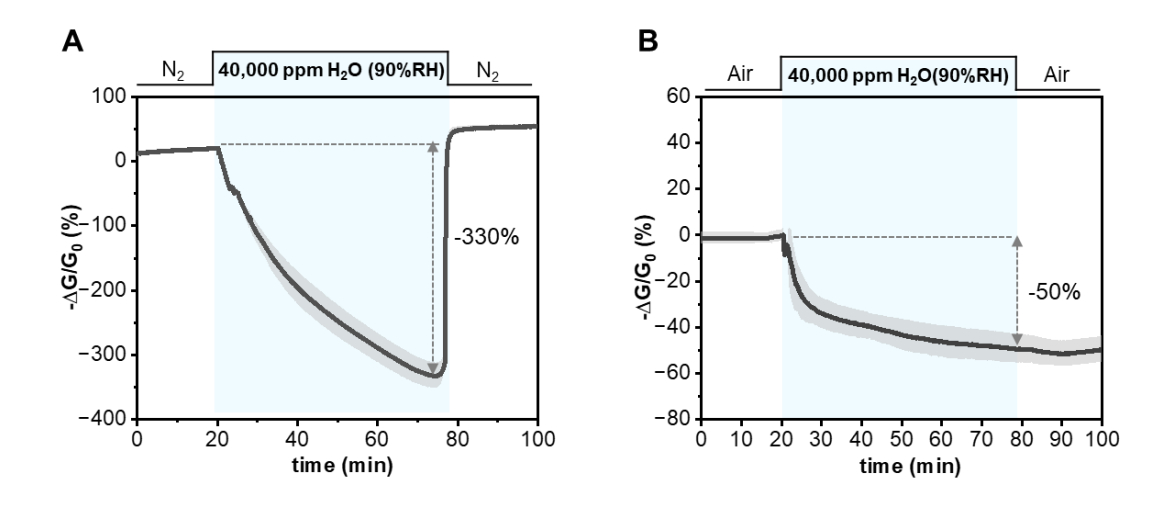


Figure S30. Chemiresistive sensing of $Cu_3(HHTP)_2$ @textile with H_2O vapor in N_2 and air. Chemiresistive sensing responses of $Cu_3(HHTP)_2$ @textile devices sensing (A) 40,000 H_2O vapor (RH = 90%) in N_2 and (B) 40,000 ppm H_2O vapor (RH = 90%) in air.

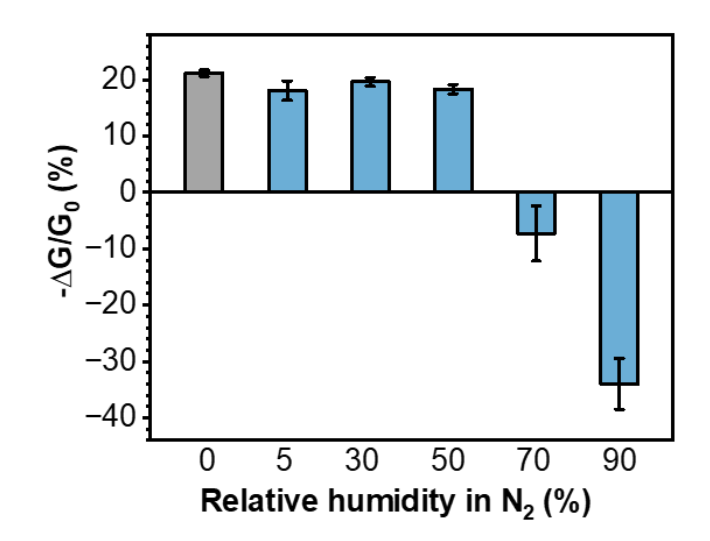


Figure S31. The sensing responses of $Cu_3(HHTP)_2$ @textile devices to 80 ppm SO_2 in N_2 with relative humidity levels ranging from 0% to 90%.

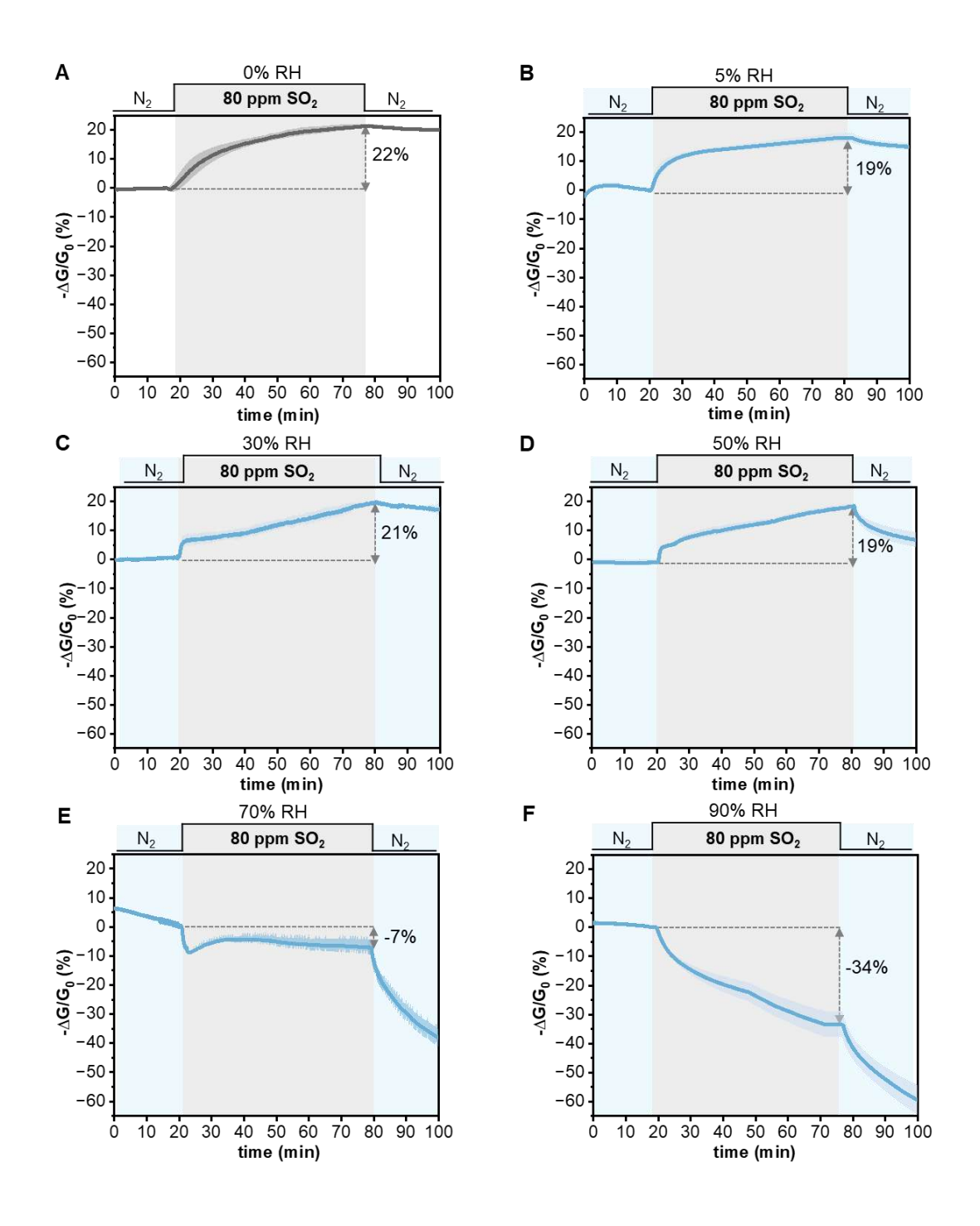


Figure S32. Chemiresistive sensing of $Cu_3(HHTP)_2$ @textile with 80 ppm SO_2 in humid N_2 . Chemiresistive sensing responses of $Cu_3(HHTP)_2$ @textile devices to 80 ppm SO_2 in N_2 with relative humidity at (A) 0%, (B) 5%, (C) 30%, (D) 50%, (E) 70%, (F) 90%.

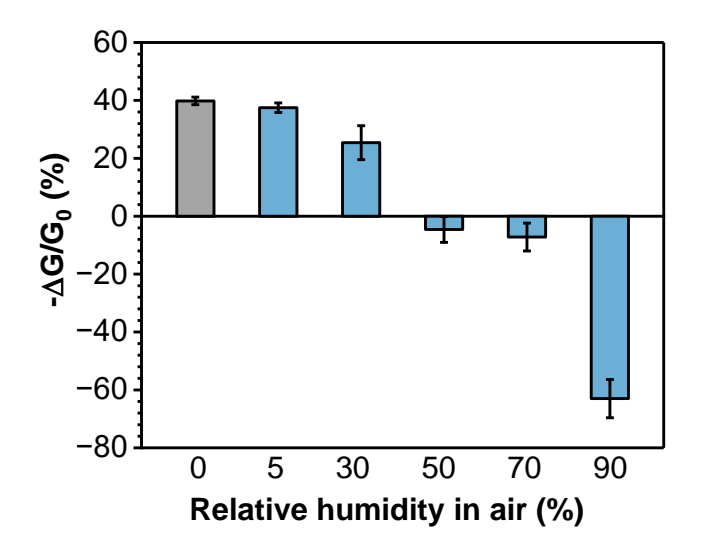


Figure S33. The sensing responses of $Cu_3(HHTP)_2$ @textile devices to 80 ppm SO_2 in air with relative humidity levels ranging from 0% to 90%.

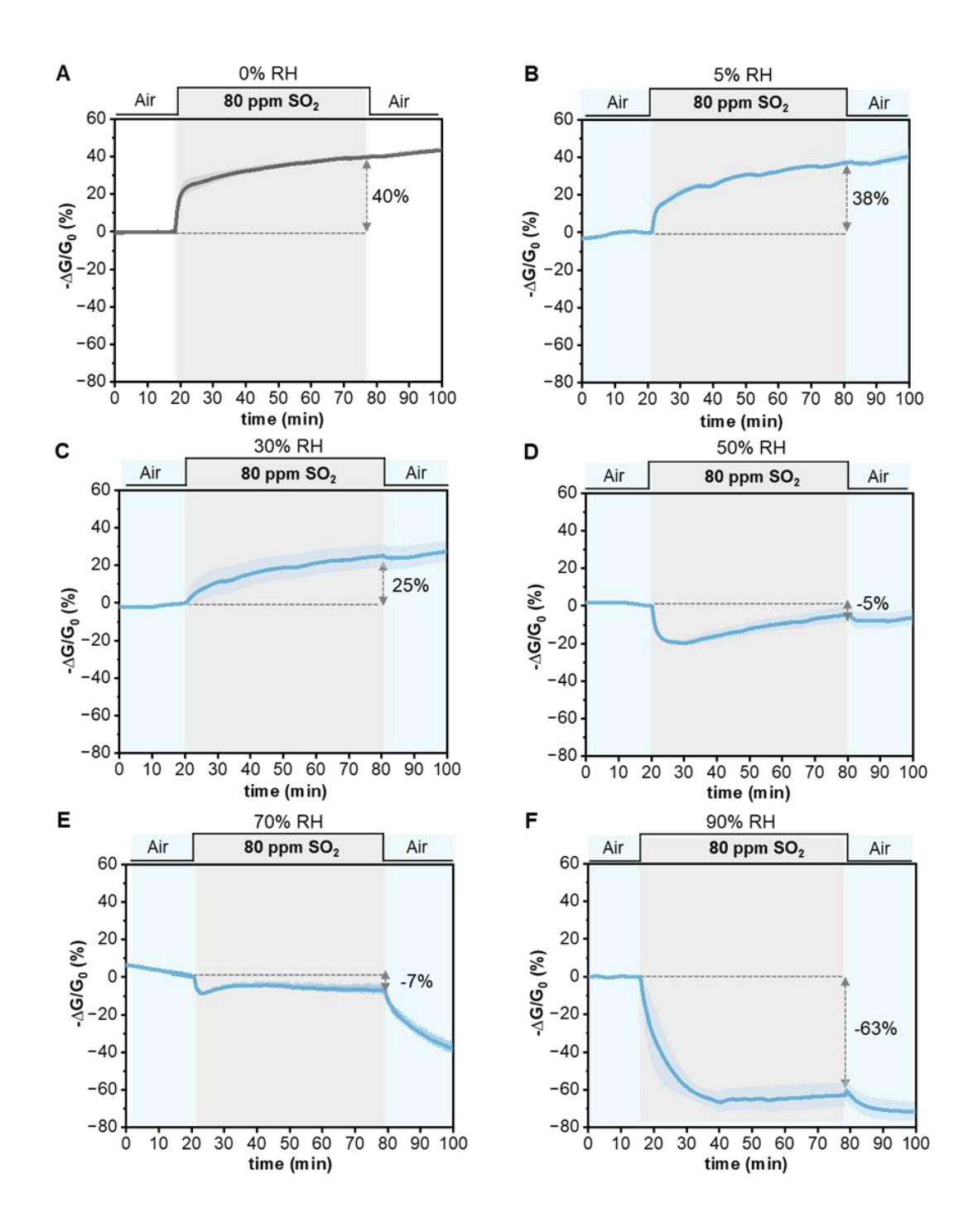


Figure S34. Chemiresistive sensing of Cu₃(HHTP)₂@textile with 80 ppm SO₂ in humid air. Chemiresistive sensing responses of Cu₃(HHTP)₂@textile devices to 80 ppm SO₂ in air with relative humidity at (A) 0%, (B) 5%, (C) 30%, (D) 50%, (E) 70%, (F) 90%.

3.3. Preparation, characterization, and sensing of Cu₃(HHTP)₂@textile-F

We adopted the low-pressure silanization method to deposit trichloro(1H,1H,2H,2H-perfluorooctyl)silane onto the surface of Cu₃(HHTP)₂@textile.⁴ The substrates were exposed to the silane vapor at a reduced pressure of 10 Pa and room temperature for 5 min to render hydrophobic properties. The modified Cu₃(HHTP)₂@textile (Cu₃(HHTP)₂@textile-F) was then left in air at 40 °C for 1 h to remove any physisorbed and unreacted silane before characterizations and tests.

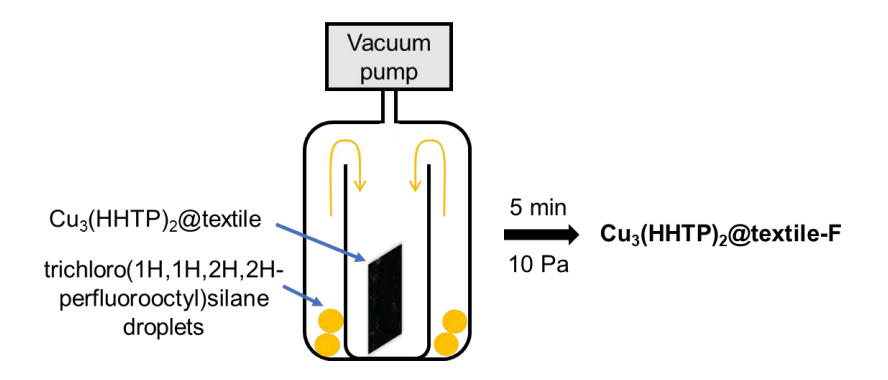


Figure S35. Low-pressure vapor deposition of trichloro(1H,1H,2H,2H-perfluorooctyl)silane onto Cu₃(HHTP)₂@textile to prepare Cu₃(HHTP)₂@textile-F.

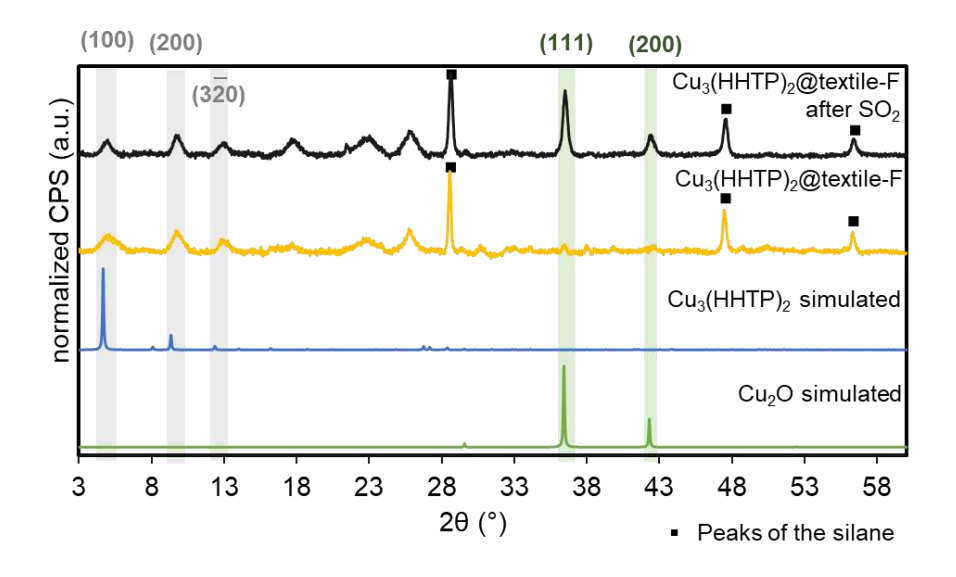


Figure S36. PXRD of Cu₃(HHTP)₂@textile-F before and after 80 ppm SO₂ sensing in N₂. The peaks at 29°, 47°, 56° correspond to the deposited silane nanostructures.⁵ New peaks at 36°, 42° after sensing SO₂ suggest the transformation from Cu₃(HHTP)₂ to Cu₂O.

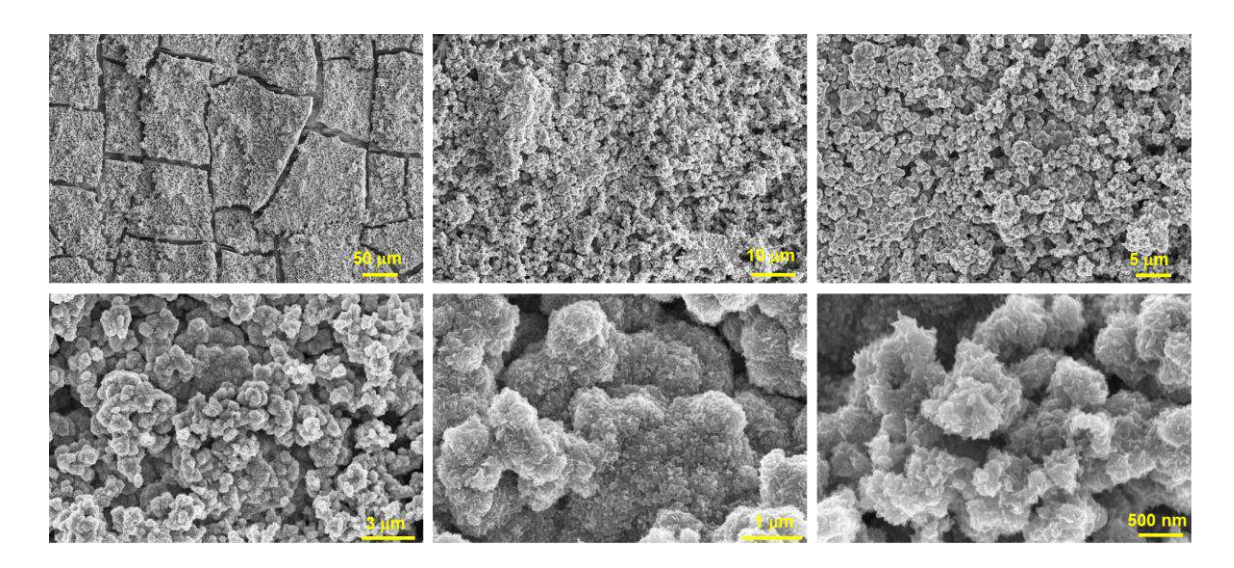


Figure S37. Scanning electron micrographs of Cu₃(HHTP)₂@textile-F.

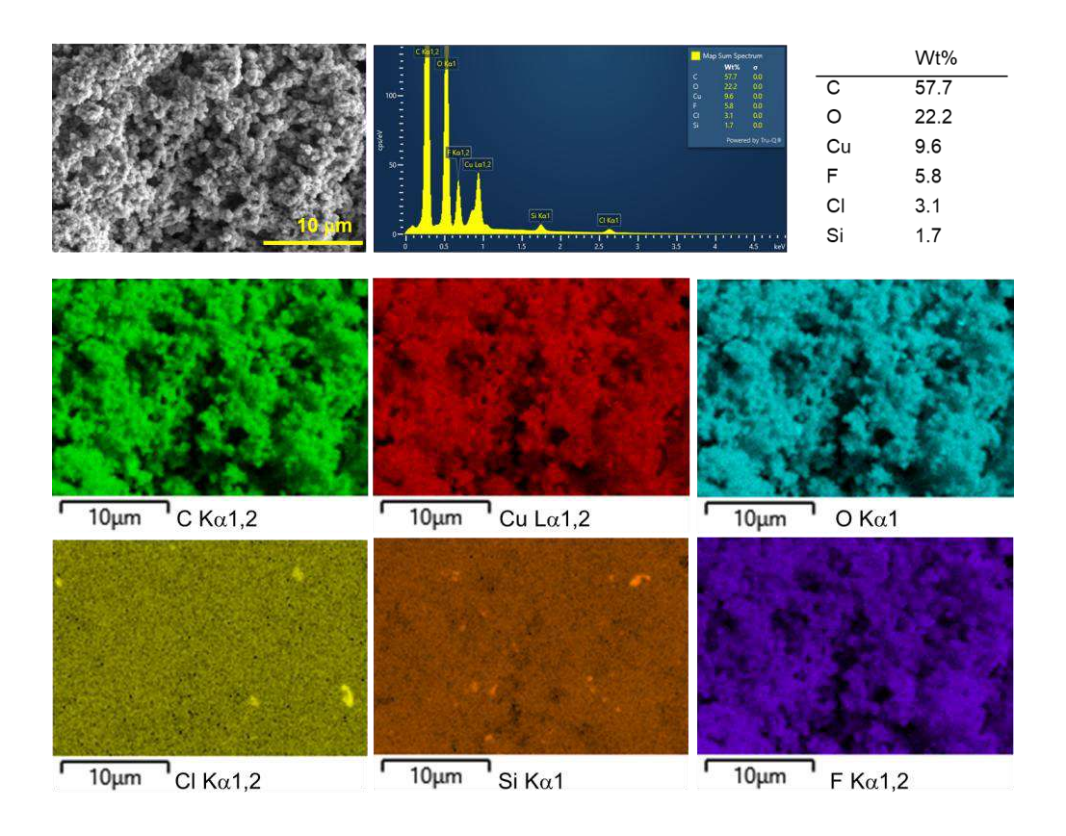


Figure S38. EDX spectrum and elemental mapping of Cu₃(HHTP)₂@textile-F with characteristic X-rays for C, O, Cu, Cl, Si, F. Elemental mapping confirms the deposition of trichloro(1H,1H,2H,2H-perfluorooctyl)silane.

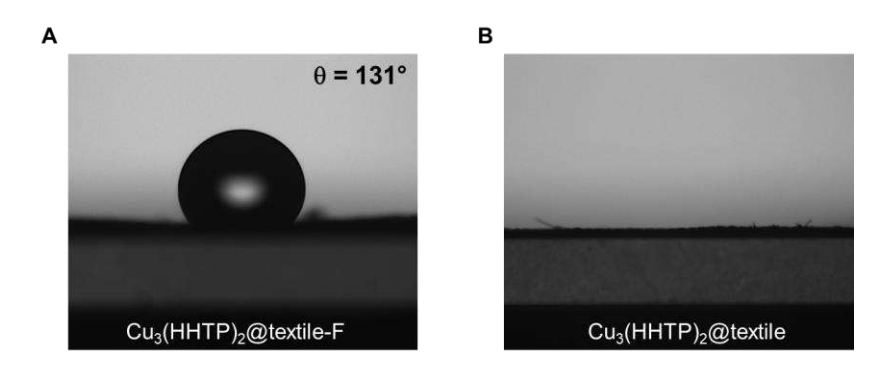


Figure S39. Surface contact angle measurement using 2uL of DI water. (A) Image of water contact angle on the surface of Cu₃(HHTP)₂@textile-F. (B) Image of the surface of Cu₃(HHTP)₂@textile where water was immediately absorbed.

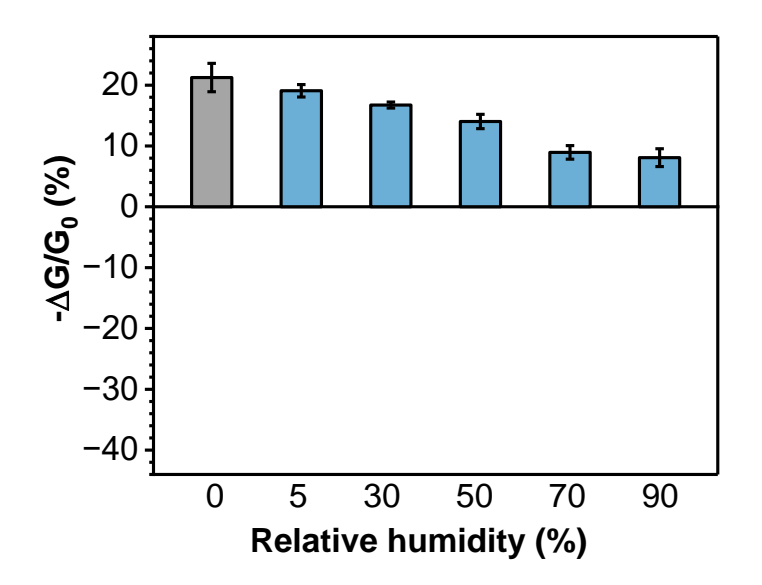


Figure S40. The sensing responses of $Cu_3(HHTP)_2$ @textile-F devices to 80 ppm SO_2 in N_2 with relative humidity levels ranging from 0% to 90%.

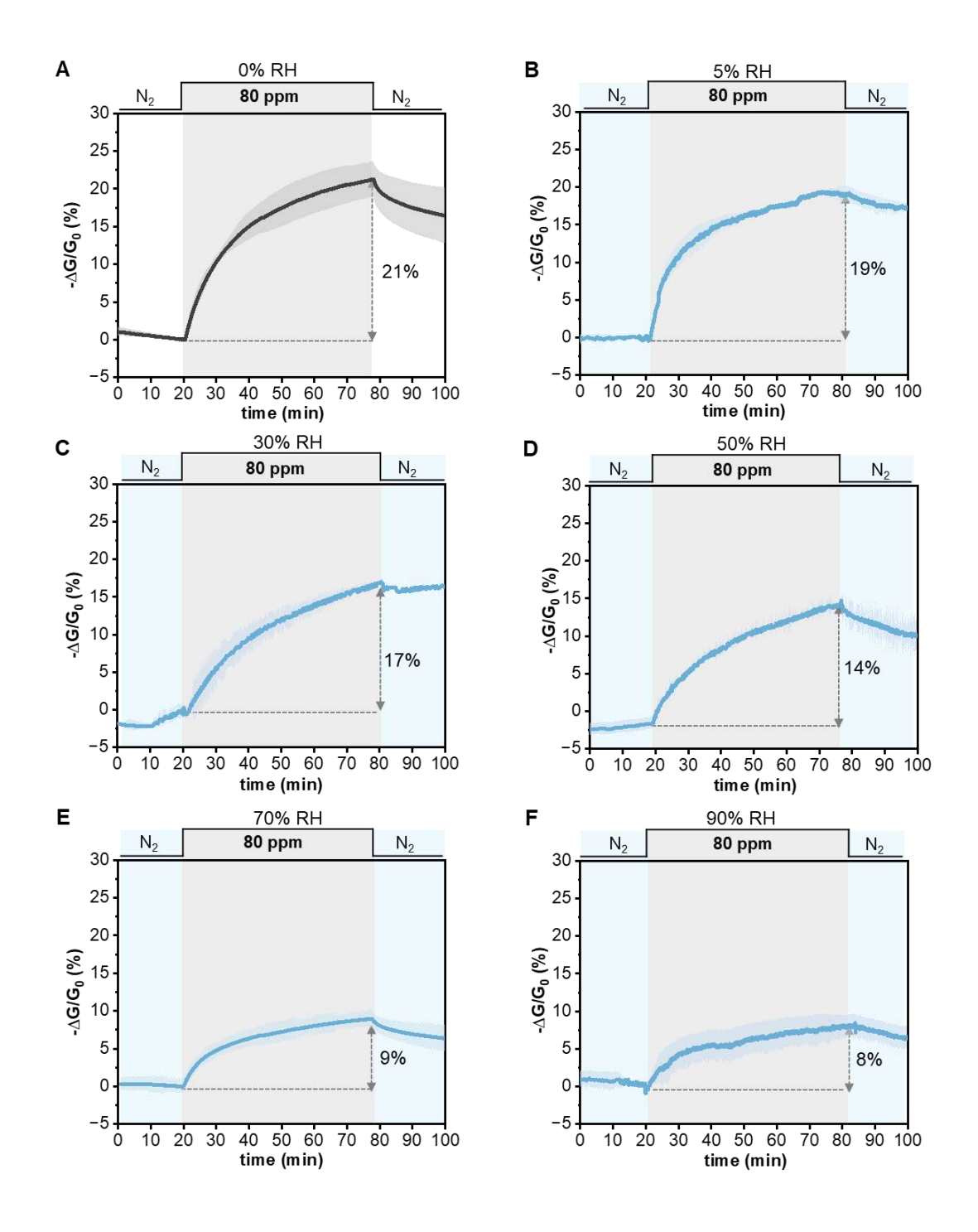


Figure S41. Chemiresistive sensing of $Cu_3(HHTP)_2$ @textile-F with 80 ppm SO_2 in humid N_2 . Chemiresistive sensing responses of $Cu_3(HHTP)_2$ @textile-F devices to 80 ppm SO_2 in N_2 with relative humidity at (A) 0%, (B) 5%, (C) 30%, (D) 50%, (E) 70%, (F) 90%.

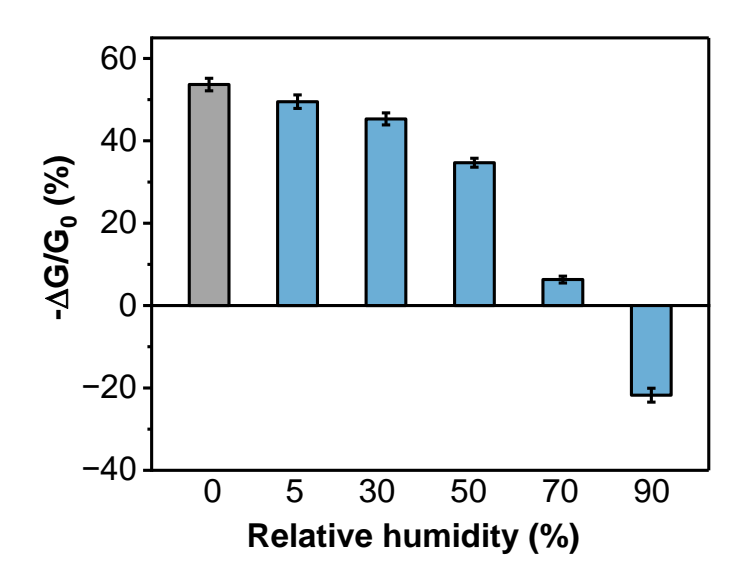


Figure S42. The sensing responses of Cu₃(HHTP)₂@textile-F devices to 80 ppm SO₂ in air with relative humidity levels ranging from 0% to 90%.

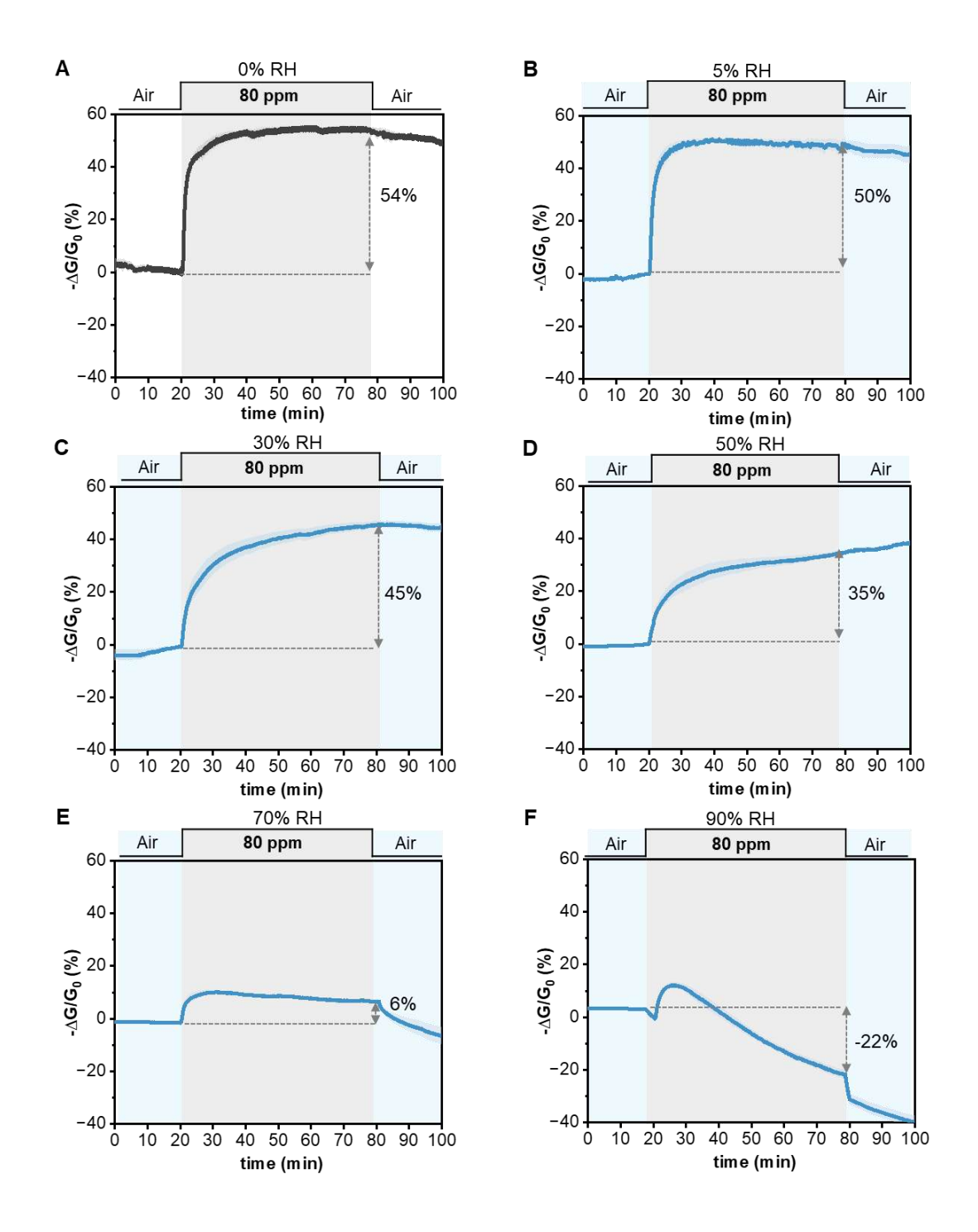


Figure S43. Chemiresistive sensing of Cu₃(HHTP)₂@textile-F with 80 ppm SO₂ in humid air. Chemiresistive sensing responses of Cu₃(HHTP)₂@textile-F devices to 80 ppm SO₂ in air with relative humidity at (A) 0%, (B) 5%, (C) 30%, (D) 50%, (E) 70%, (F) 90%.

3.4. Regenerability evaluation of Cu₃(HHTP)₂@textile

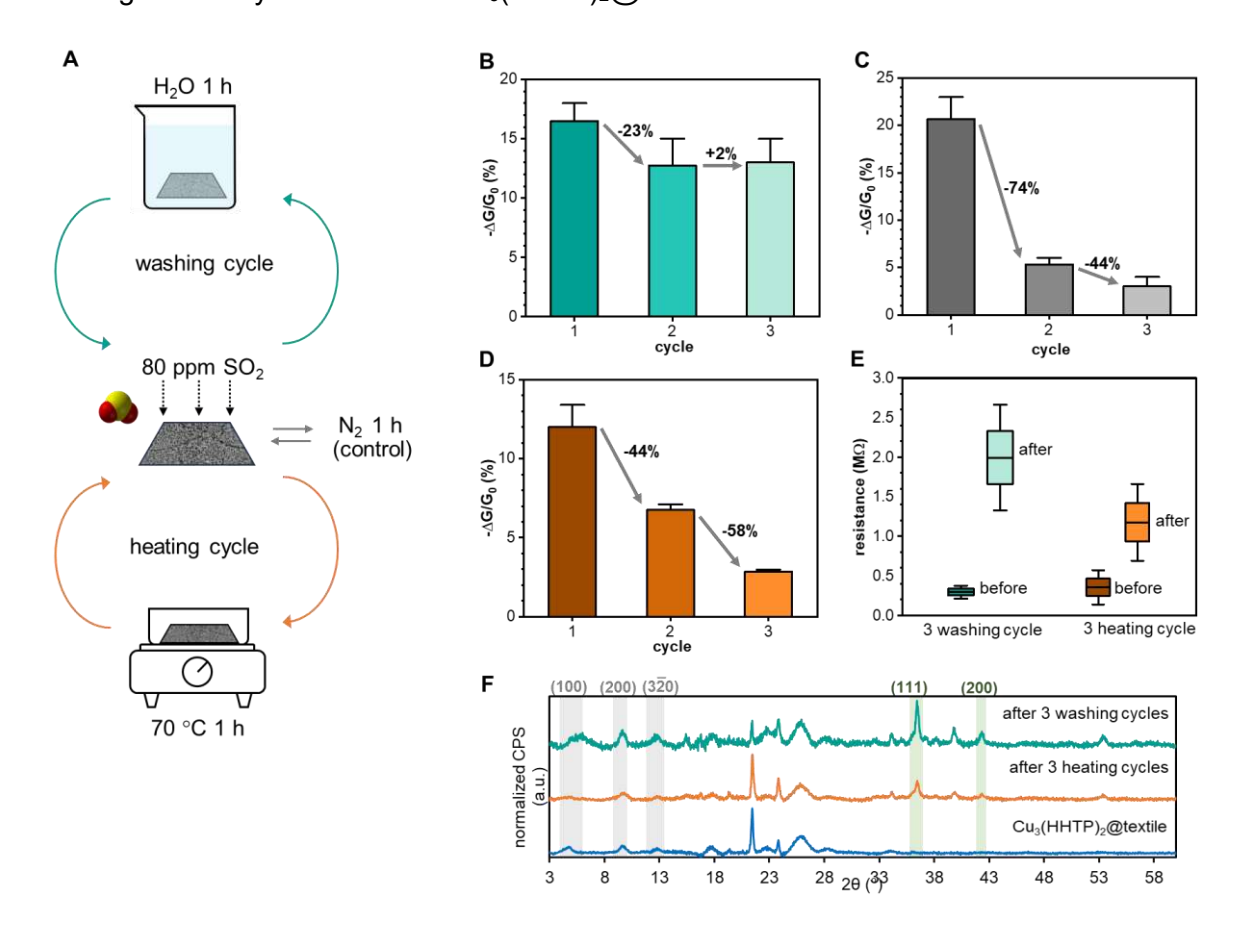


Figure S44. Regenerability of Cu₃(HHTP)₂@textile assessed through washing or heating treatments. (A) Scheme of the cyclic washing and heating treatments on the Cu₃(HHTP)₂@textile device. Cyclic sensing performances of Cu₃(HHTP)₂@textile towards 80 ppm SO₂ for 1 hour after (B) 1-hour washing with DI water, (C) 1-hour N₂ exposure, and (D) 1-hour heating at 70 °C. (E) Resistances of Cu₃(HHTP)₂@textile before and after the recovery processes of washing or heating. (F) PXRD comparison of Cu₃(HHTP)₂@textile before and after the recovery processes of washing or heating.

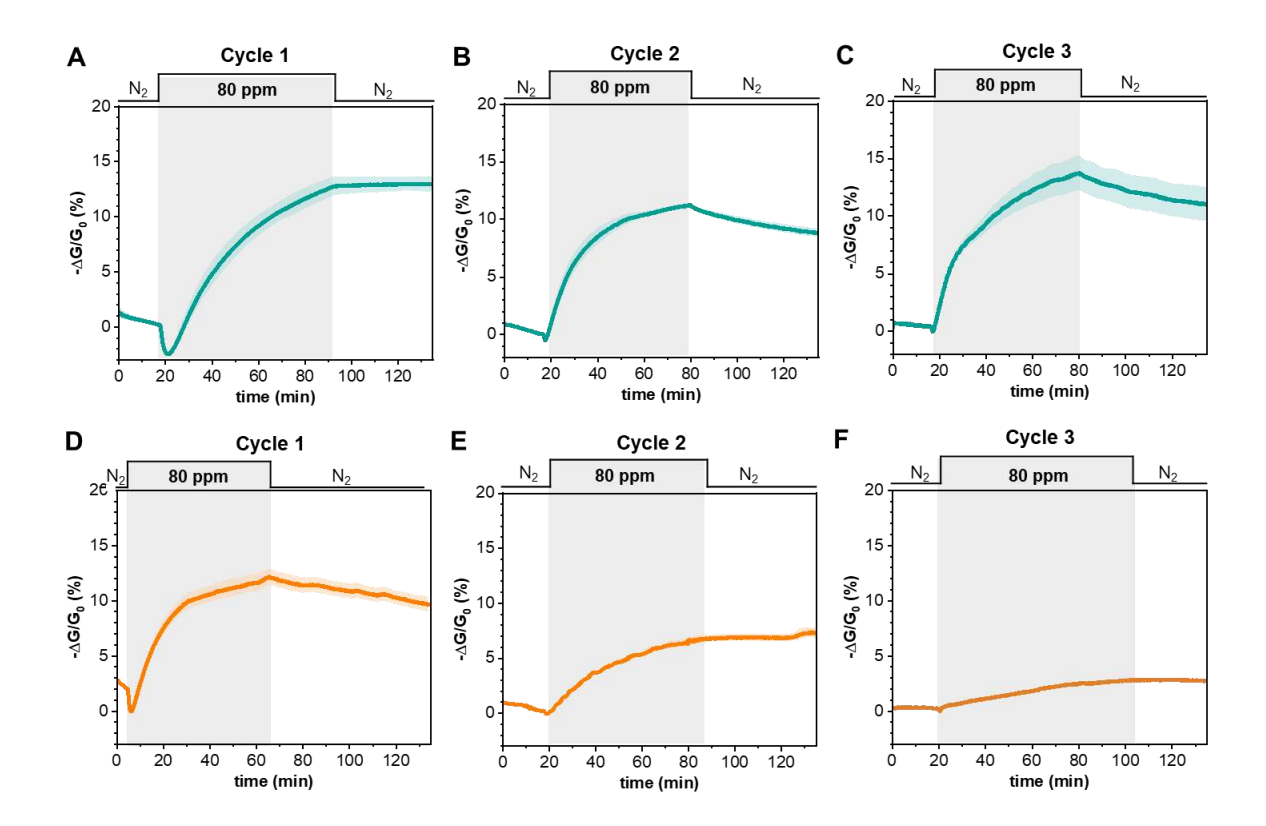


Figure S45. Chemiresistive sensing of Cu₃(HHTP)₂@textile with 80 ppm SO₂ under regenerability analysis. Sensing response diagrams of Cu₃(HHTP)₂@textile devices underwent the (A) first, (B) second, and (C) third sensing of 80 ppm SO₂ after washing treatments. Sensing response diagrams of Cu₃(HHTP)₂@textile devices underwent the (C) first, (D) second, and (E) third sensing of 80 ppm SO₂ after heating treatments.

4. Spectroscopic investigation

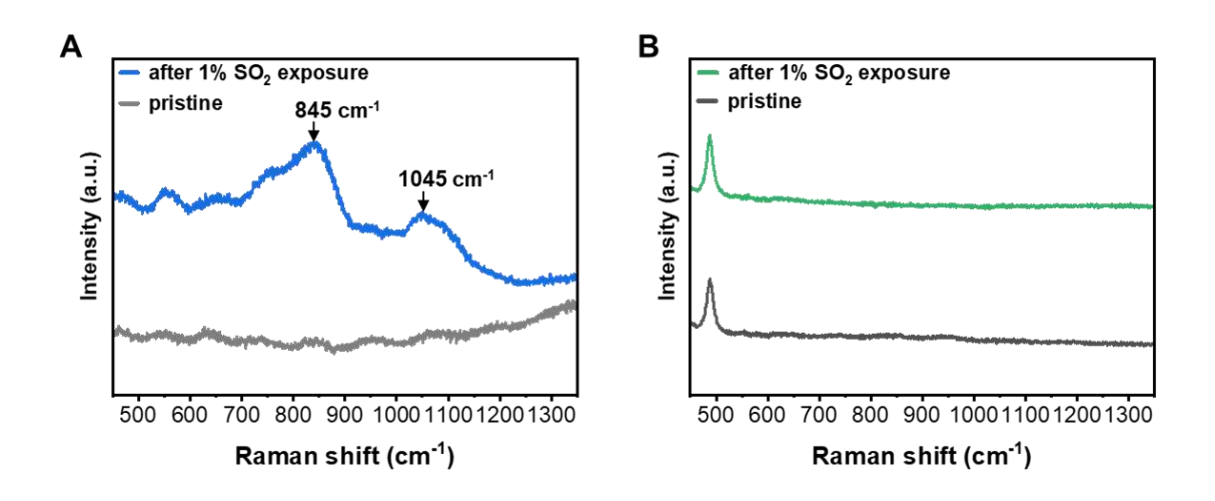


Figure S46. Raman spectroscopic comparison. Raman spectra of (A) Cu₃(HHTP)₂ powder and (B) Cu(OH)₂@textile devices before and after 1% SO₂ treatment for 0.5 h. Cu₃(HHTP)₂ powder showed characteristic Raman bands at 1045 cm⁻¹, 856 cm⁻¹, corresponding to the symmetric stretch (v1) of the solid-state sulfate and the O-H bending of hydrated sulfate due to the aqua ligand in Cu₃(HHTP)₂. No Raman band change was observed for Cu(OH)₂@textile devices before and after 1% SO₂ treatment for 0.5 h.

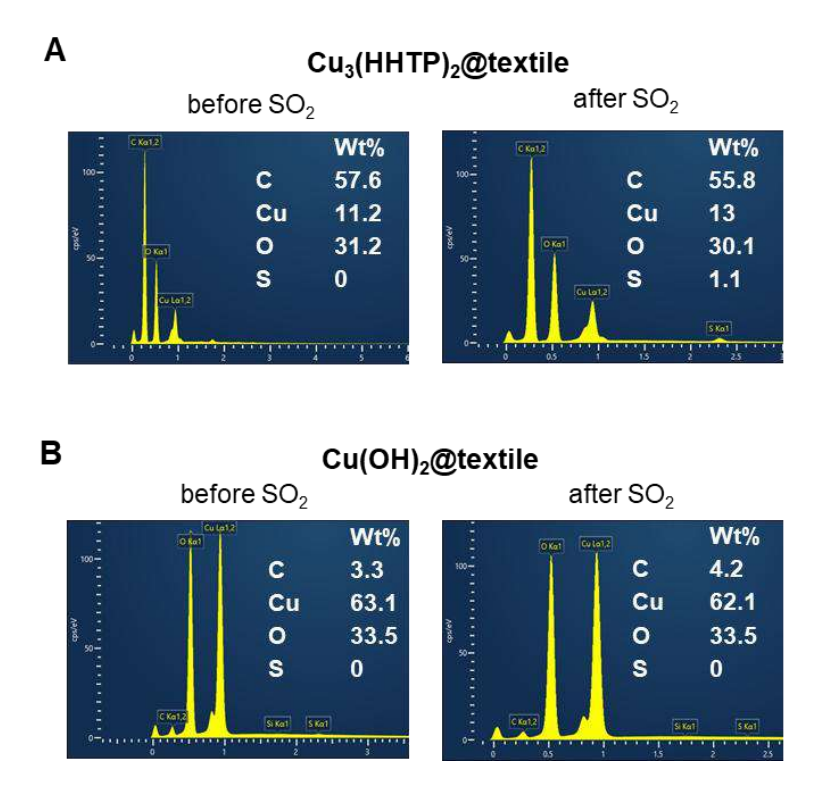


Figure S47. EDX-SEM comparison before and after SO₂ exposure. EDX-SEM of (A) $Cu_3(HHTP)_2$ @textile and (B) $Cu(OH)_2$ @textile devices before and after three-cycle 80 ppm SO_2 sensing experiment in N_2 .

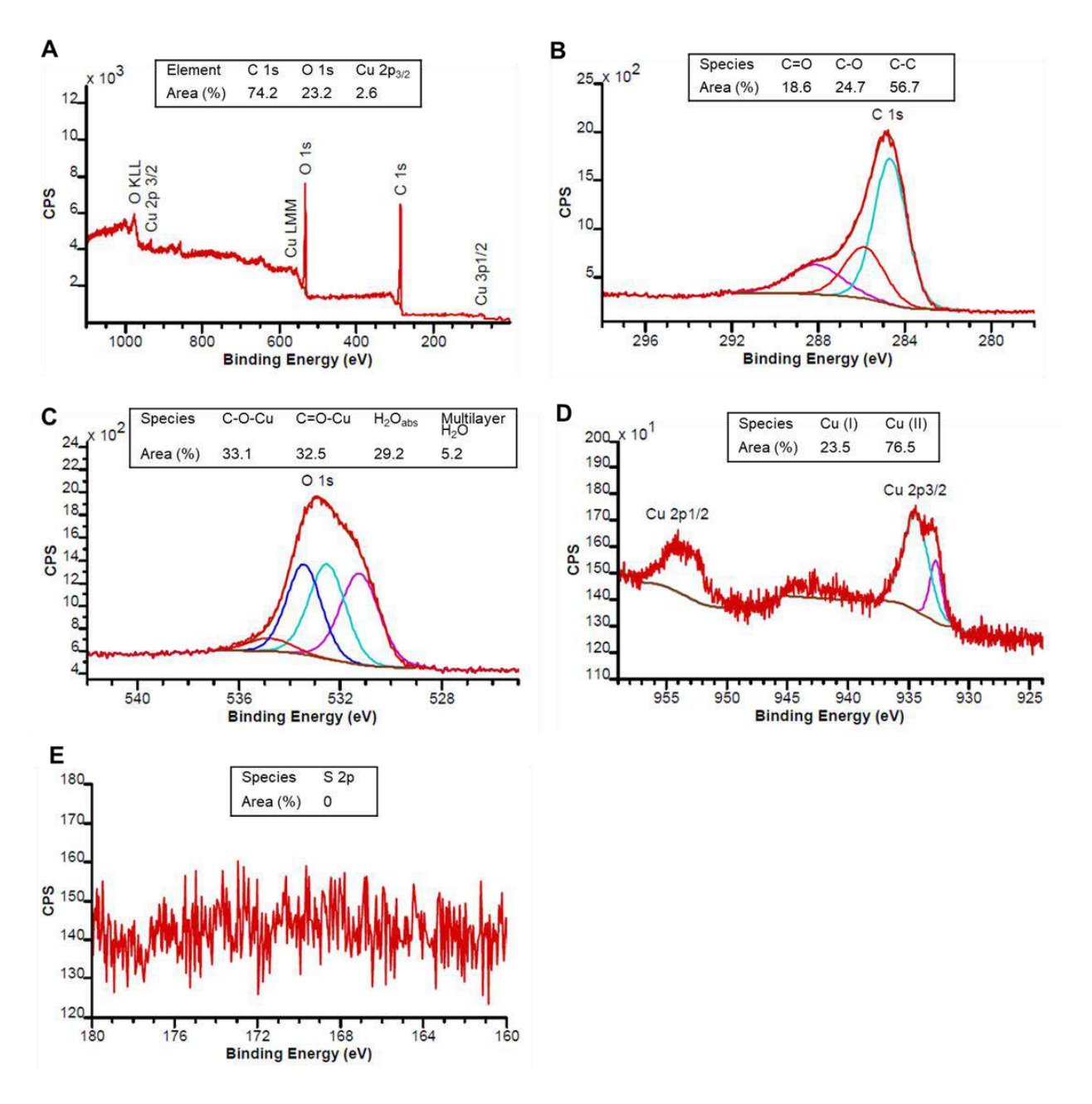


Figure S48. XPS spectra of Cu₃(HHTP)₂@textile. (A) Wide energy survey scan and high resolution (B) C 1s, (C) O 1s, (D) Cu2p3/2 (E) S 2p spectrum of the pristine Cu₃(HHTP)₂@textile device.

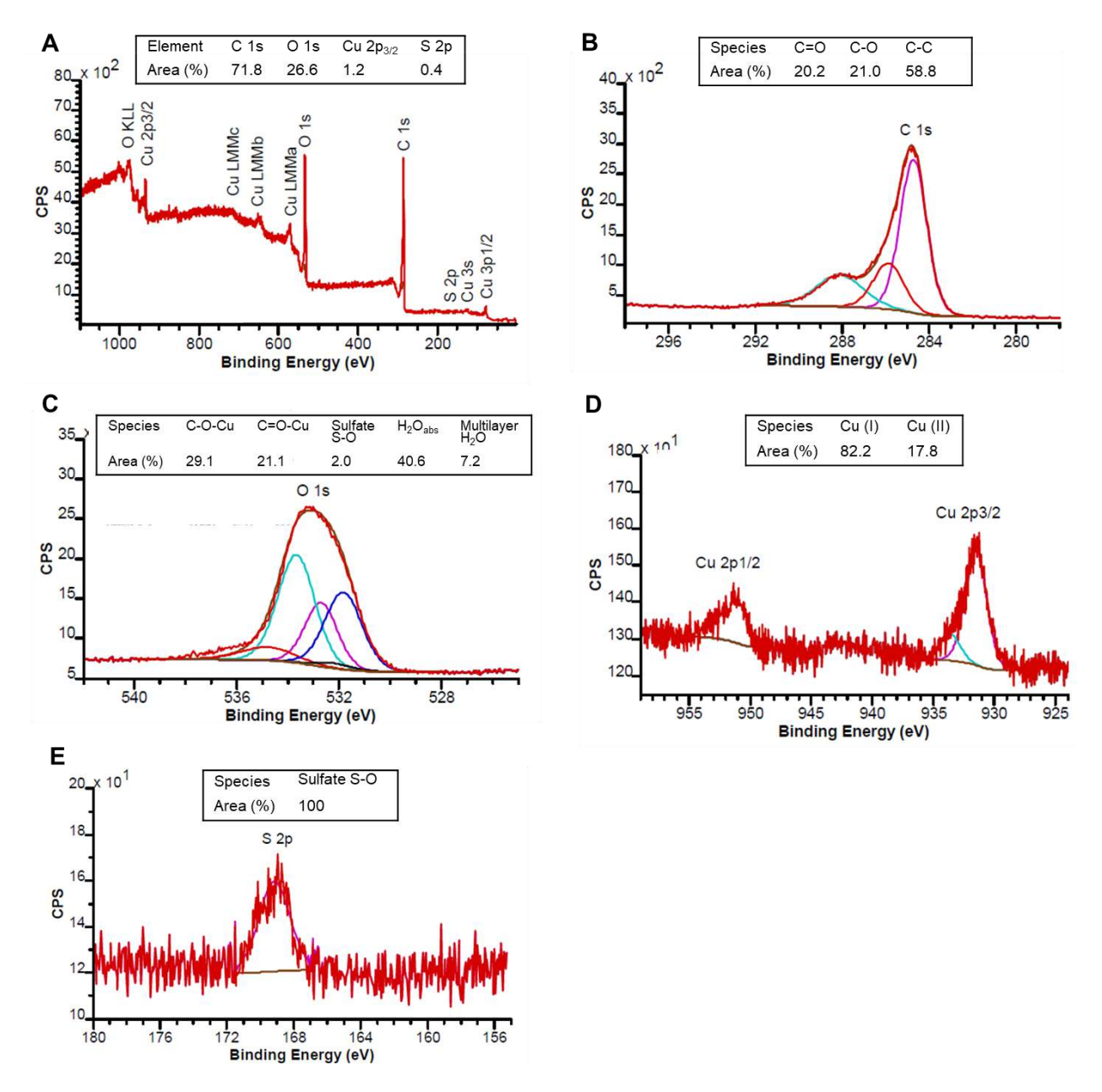


Figure S49. XPS spectra of $Cu_3(HHTP)_2$ @textile after SO_2 exposure. (A) Wide energy survey scan and high resolution (B) C 1s, (C) O 1s, (D) $Cu_2p_3/2$ (E) S 2p spectra of the $Cu_3(HHTP)_2$ @textile device after 1% SO_2 exposure for 0.5 hour.

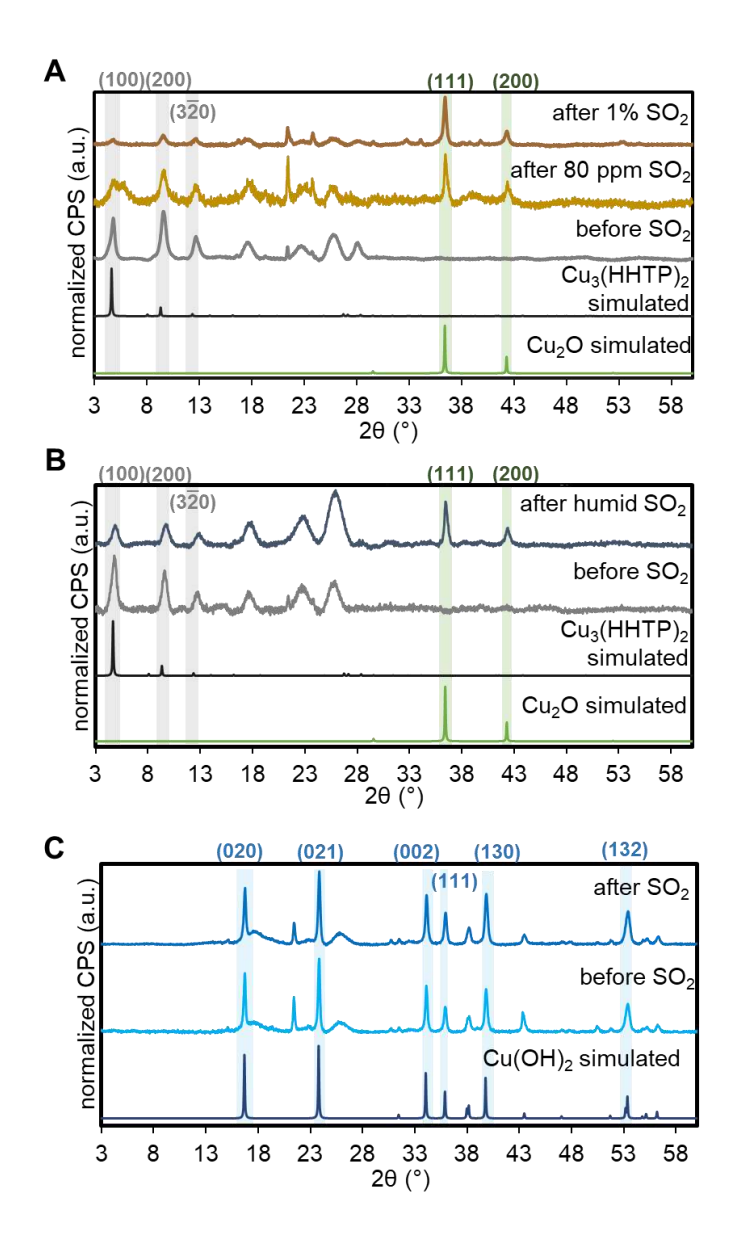


Figure S50. PXRD comparison before and after SO_2 exposure. PXRD spectra of (A) $Cu_3(HHTP)_2$ @textile before and after three-cycle 80 ppm SO_2 sensing experiment and after a 30-minute exposure to 1% SO_2 in N_2 , (B) $Cu_3(HHTP)_2$ @textile before and after 80 ppm SO_2 sensing experiment in humid N_2 (RH=90%), and (C) $Cu(OH)_2$ @textile before and after 80 ppm SO_2 sensing experiment in N_2 .

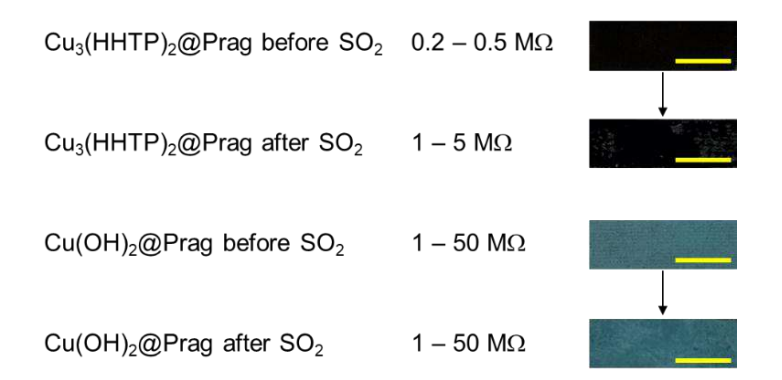


Figure S51. Optical and resistance comparison of $Cu_3(HHTP)_2$ @textile and $Cu(OH)_2$ @textile devices before and after three-cycle 80 ppm SO_2 sensing experiment in N_2 . Scale bar = 1 cm.

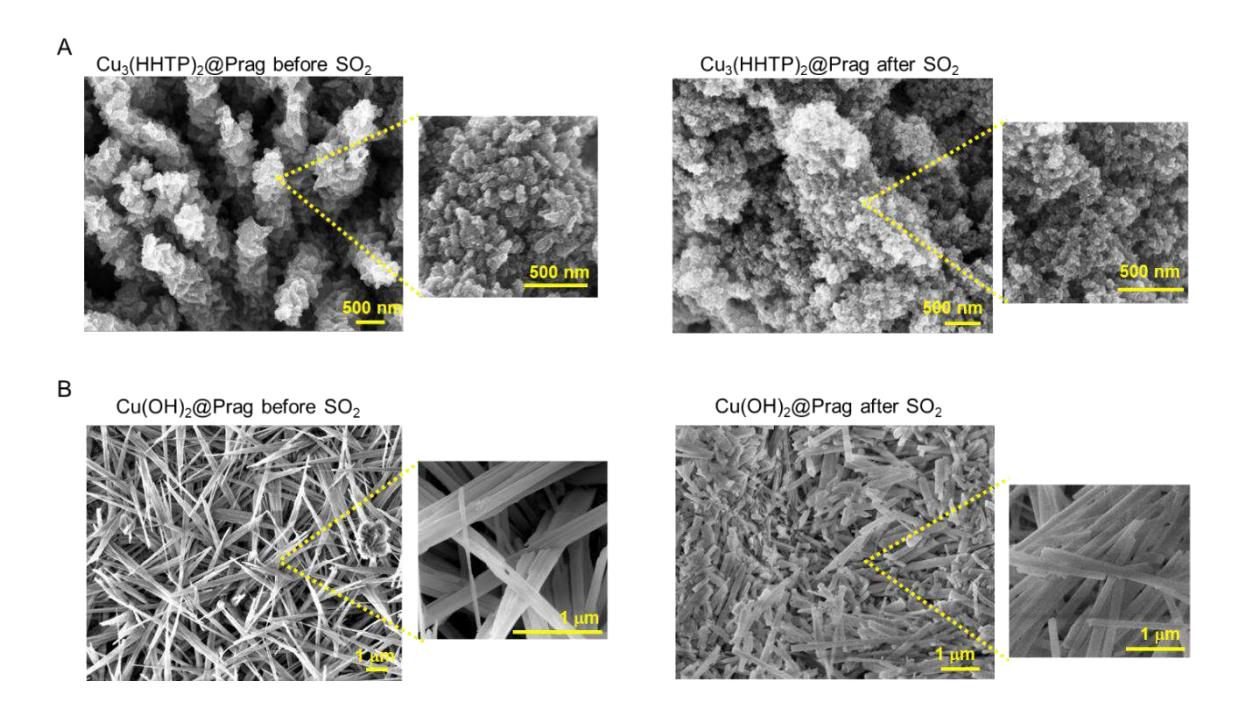


Figure S52. SEM comparison before and after SO_2 exposure. SEM images of (A) $Cu_3(HHTP)_2$ @textile and (B) $Cu(OH)_2$ @textile devices before and after three-cycle 80 ppm SO_2 sensing experiment in N_2 .

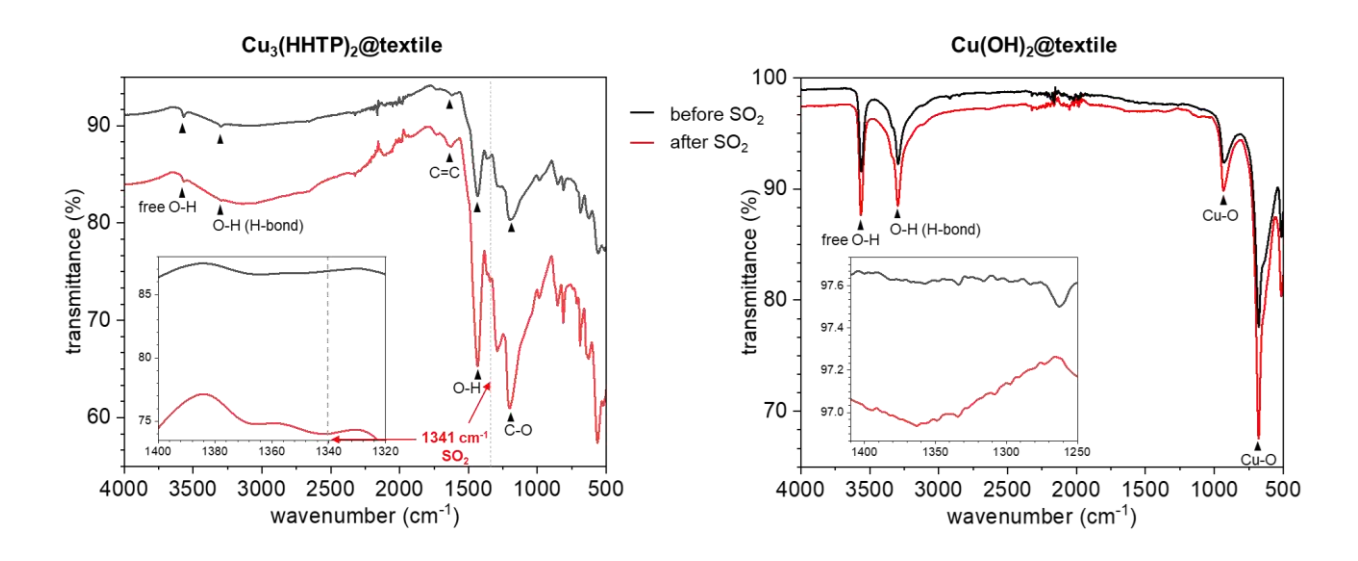


Figure S53. Attenuated Total Reflectance (ATR)-IR spectra of Cu₃(HHTP)₂@textile and Cu(OH)₂@textile devices before (black trace) and after (red trace) three-cycle 80 ppm SO₂ sensing experiment in N₂. The band at 1341 cm⁻¹ were assigned to the asymmetric stretching mode of absorbed SO₂.

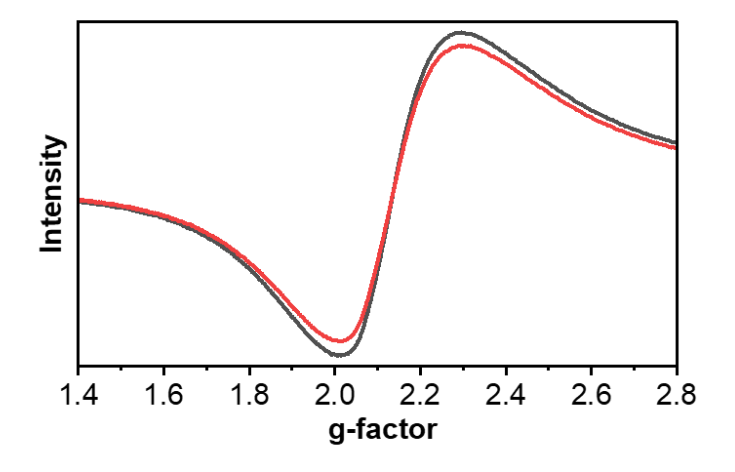


Figure S54. EPR spectra of Cu₃(HHTP)₂ powder before and after a 30-minute exposure to 1% SO₂ in N₂. The first derivative of the absorbance spectra is shown for pristine Cu₃(HHTP)₂ stored under N₂ (black trace) and for Cu₃(HHTP)₂ after 30 minutes of exposure to 1% SO₂ in N₂, followed by 1-minute N₂ flow to remove any unabsorbed SO₂ from the tube (red trace). The unpaired spin density changes decreased slightly after 30 minutes of exposure of SO₂, suggesting the conversion of EPR-active Cu²⁺ to inactive Cu⁺ species.

5. Theoretical Activity

5.1. Periodic quantum chemistry calculations at the DFT level

The atomic coordinates of the Cu₃(HHTP)₂ 2D-MOF were obtained from the CIF file of corresponding to "Eclipsed Structure" in a previous work.⁶ To study alternative stackings along the *c* axis, the Cu₃(HHTP)₂ unit cell was doubled along the *c* axis, and also extended in the (*xy*) plane considering several (2x2) stacking sequences. All the structures were optimized at the density functional theory level (DFT) using the Quantum Espresso (QE) package,⁷ projector Augmented-Wave (PAW) pseudopotentials⁸ and the generalized gradient approximation (GGA) with the Perdew–Burke–Ernzerhof (PBE) functional. Dispersion corrections were added according to the Grimme-D3 parametrization implemented in the QE package.⁹ Wave function and charge density cutoffs for the plane-wave basis sets of 60 and 600 Ry were employed, respectively. Single-particle wave functions were calculated spin-unrestricted by applying smearing of the one-particle levels of 0.002 Ry. Periodic boundary conditions were used in all directions.

In the case of the monolayer 1L-(1x1) cell, reciprocal space was sampled by using a (1x1x6) k-point grid, whereas in the case of the bilayer 2L-(1x1) cells, the reciprocal space was sampled by using a (1x1x3) k-point grid. Benchmark calculations employing finer (2x2x12) and (2x2x6) k-point grids for the monolayer and the bilayer cells, respectively, were conducted, and we verified that the coarser grids result in quantitative agreement with the finer grids. When considering the case of bilayer 2L-(2x2) or 4L-(1x1) cells, reciprocal space was sampled at the gamma point only due to the substantial computational effort of this series of simulations. If not differently specified, all the cells were optimized by applying variable-cell algorithms to optimize the structures at equilibrium lattice constants locally. Transition states along reaction coordinates were identified by employing the NEB algorithms implemented in the QE software.

MP2 calculations were carried out via the Gaussian16 software¹⁰ considering finite-size models systems. 6-31G(d,p), and def2-TZVPP for Cu basis sets were used. Charge analysis is performed with an NBO scheme, as implemented in the g16 software.

5.2. Preliminary considerations and RMD simulations set up

To simulate the properties of the Cu₃(HHTP)₂ material deposited on textile, we modeled the solid-state surface of the MOF/textile using classical reactive molecular dynamics (RMD) simulations. These simulations utilized a previously parametrized force field (MP), specifically designed to accurately reproduce the structure and dynamics of semiconducting materials adsorbed onto textile fibers.^{11, 12} The reliability and efficiency of the force field parameters were demonstrated, not only by the excellent results in agreement with the experiment, but also by the ability of the simulations to distinguish between the copper ions coordinated to the oxygen edges and copper atoms aggregated in metal nanoclusters. In the present study, before starting the simulations of the extended systems with dimensions comparable to the experiments, we tested the force field against the small models optimized at the DFT level. All the ReaxFF optimized geometries were in satisfactory agreement with the DFT data, having maximum coordinates of the Cu₃(HHTP)₂ 2D-MOF unit of all the atoms of about 0.08 Å and analogous energy differences.

We built a supercell model made of seven layered planes of several hexagonal complex units extended twelve times in a and b directions (supercell size: $262.32 \times 262.32 \times 23.31 \text{ Å}^3$ with angles 90° , 90° , 120° , total atoms: 63504, **Figure S55**). This representation, less biased by the small cell's periodic boundary conditions, can provide a more flexible/adaptable model of a 2D-MOF with 1D channels closer to the experimental conditions in the case of bulk material. Another model with 8x8 units in a and b directions and 20 layers (approximately 7 nm) was used to test the possible vertical arrangements and rotations of the molecules in the various planes (**Figure S56**). For the simulation of the textile-MOF interface, we employed the addition of a graphitic plane in place of the fabric fibers (cellulose fibers) parallel to the MOF layers and elongation of the cell size in the c direction to 90 nm. This choice was dictated by the need to reduce the computational cost, avoid constraints to the MOF, and preserve the

supposed parallel-layered structure. During the simulations, we froze only the coordinates of all the atoms of the graphitic plane.

Considering the MOF thickness, we maintained the extended seven-layer model used for the bulk calculations (with a thickness of approximately 2.5 nm). Besides, from preliminary tests on thicker models (12 layers), we noticed that beyond the sixth/seventh layer from the surface, the dynamical behavior of the structure was remarkably similar to that of the bulk. Therefore, we believe that this size we have chosen is sufficient to simulate the variability of the environment at the material/air interface and represent the experimental observations at an affordable computational cost. We prepared separate MOF models filled with water and SO_2 at the same concentration and ran bulk and MOF-on-textile RMD simulations at ambient temperature and pressure for about 250/300 ps (**Figure S55**). We inserted approximately 31 ± 2 molecules in each channel (average channel volume ≈ 5 nm³, 6.3 molecules/nm³), excluding the channels at the edges of the model to verify the possibility of migration of the molecules to these regions during their thermal motion. It shows the initial configuration after optimization, where all the added molecules are initially close to the channel walls.

As the experimental characterization suggested that moisture could be present inside the material even though it was air-dried, we tried to estimate a possible water presence by simulating the dynamics of the drying process. We started with the final structure sampled from the RMD of the MOF-on-textile filled with water and increased the temperature to 100°C. After about 100 ps, only 20% of the water remained trapped in the layers of structure closer to the textile. The stability of these molecules was tested by carrying out another 50 ps-RMD at ambient temperature. The result shows that most of the water molecules remain deep inside the framework. The final configuration, containing about five water per channel, was filled with SO₂ (about 13 per channel), and the RMD of the filled MOF-on-textile was performed for about 300 ps.

5.3. RMD simulations details and analysis tools

The dynamics of the supercell model was simulated by the ReaxFF MD code available in the LAMMPS program.¹³ All the calculations were based on published work with well-tested parameters. 11, 12 In the RMD simulations, reactivity was always on, and no constraints were applied to the MOF-filled systems (only the graphitic plane was frozen). All species could interact with each other and modify their conformation in response to the environment. The models were energy-minimized, gradually heated to 298 K, and equilibrated at that temperature. After the equilibration period, production RMDs were carried out in the NVT ensemble for about 250-300 ps. The time step was set to 0.2 fs. The Anderson thermostat controlled the temperature with a relaxation constant of 0.1 ps. The system configurations were collected every 0.02 ps. The analysis of the sampled data was focused on the last portions of the trajectories. The examined descriptors were mainly atom-atom radial distribution functions (RDFs) and 3D-atom-density contours, which were used to identify the position of the copper metal centers, water, and SO₂ inside the channels. The shape and volume of the channels were evaluated through the Caver software (Figures S55-S57).14 Visual inspection of the trajectories was fundamental to understanding the adsorption scenarios, the guests' coordination to the metal centers, their diffusion in the channels, and the evolution of the MOF structure.

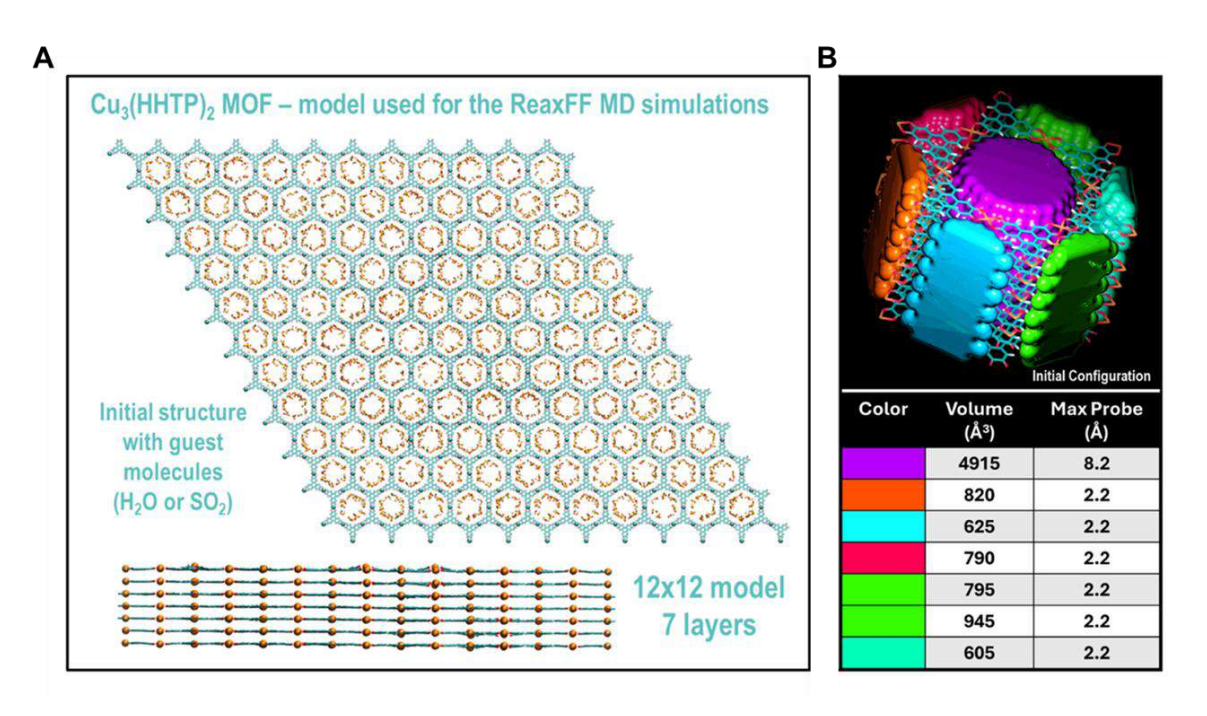


Figure S55. A seven-layer model of hexagonal Cu₃(HHTP)₂ complex for RMD simulations.

(A) The initial model of the $Cu_3(HHTP)_2$ MOF supramolecular system containing H_2O or SO_2 molecules, optimized at the classical ReaxFF level. (B) An evaluation of the volume of one of the channels through the Caver software.

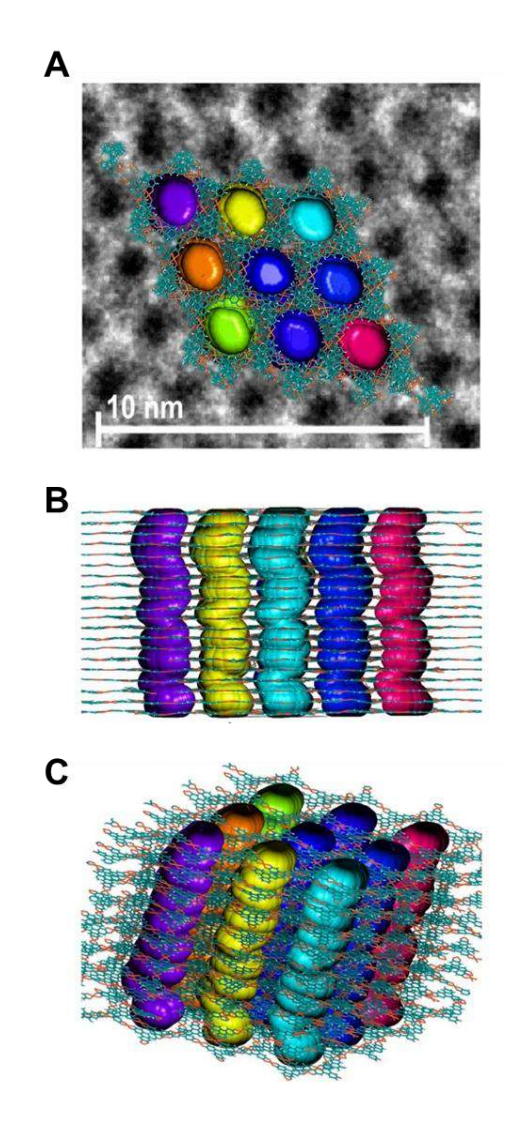


Figure S56. RMD images of hexagonal $Cu_3(HHTP)_2$ complex. RMD snapshots superimposed to an experimental SEM image of reference in (A) top, (B) front, and (C) isometric view.⁶ The snapshot of the channels was visualized through the Caver software.

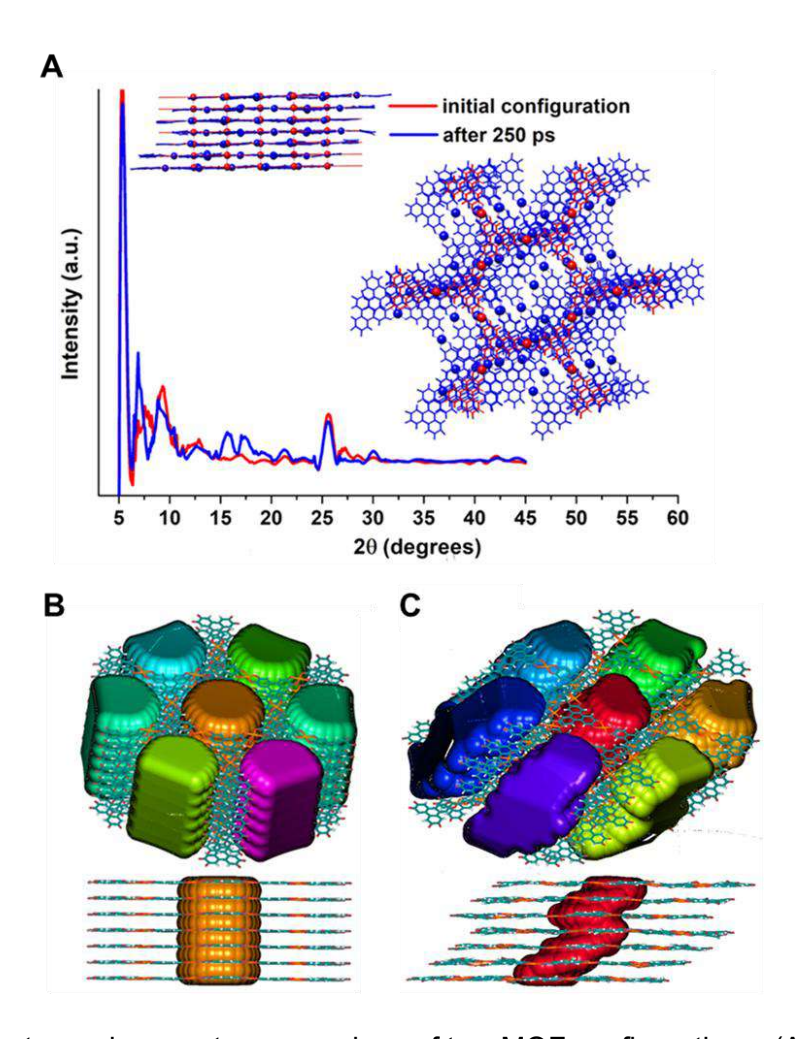


Figure S57. Spectra and geometry comparison of two MOF configurations. (A) The calculated XRD spectra of the initial (red lines) and final (blue lines) configurations of the empty model (central portion: reduced number of atoms). (B) The initial geometry that all the stacked planes are eclipsed; (C) The final configuration with significant distortion and contraction of the channels. After 300 ps MD at ambient temperature, the volume of the channels is reduced by approximately 27%. The volume of the channels was evaluated through the Caver software.

Indeed, even at the finest scale of the computational investigation (quantum chemistry calculations on smaller portions of the material) focused on structure optimization only, it is apparent that the MOF-assembled components are prone to rotations and translations. The results of the structural and electronic characterization of the monolayer cell, 1L-(1x1) (Eclipsed), are reported in **Table S6** and **Figure S58**. The optimized values of the unit cell

lattice constants agreed with the PXRD measurements, being slightly contracted by about 0.5% in the (xy) plane and dilatated by about 1% along the c-axis. The lowest-energy electronic potential energy surface (PES) is characterized by a metallic character and a finite spin polarization, which is mainly localized on the Cu and O atoms (**Figure S58B-C**). The Cu atoms are formally in a Cu²+ oxidation state, corresponding to a $3d^9$ electronic configuration with an empty d-band above the Fermi level in the minority spin PDOS. This is also reflected in the spin-density iso-surface, which has a $3d(xy/x^2-y^2)$ character with its lobes pointing in the direction of the O atoms, where a partial 2sp polarization is also localized (visible in the corresponding PDOS). These results agree with previous experimental characterization. ^{15, 16}

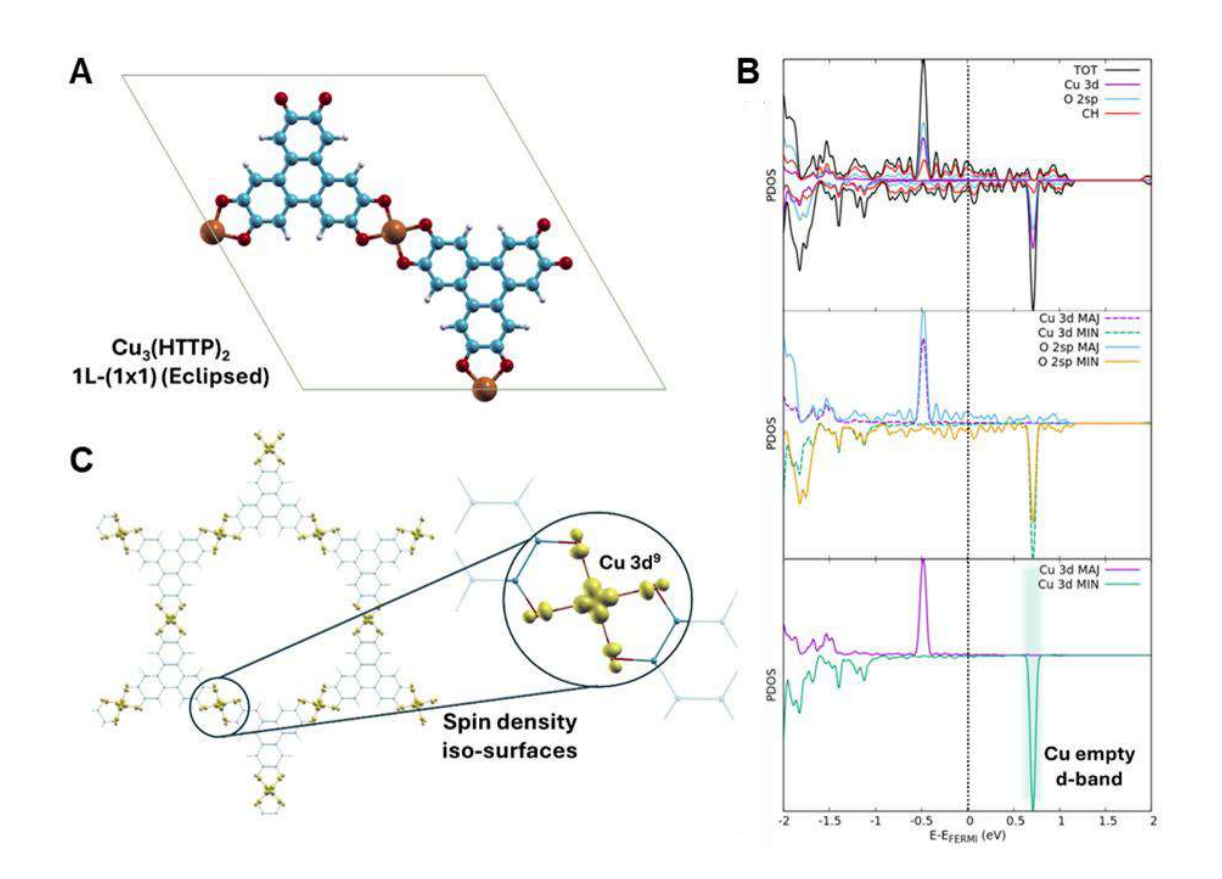


Figure S58. Electronic structure calculations of the monolayer $Cu_3(HHTP)_2$. (A) The structure of the 1L-(1x1) (Eclipsed) unit cell of the $Cu_3(HHTP)_2$ system. (B) PDOS of the structure where the main atomic contributions have been plotted for both majority and minority spin components. (C) Spin density iso-surface at a value of 0.02 a.u. corresponding to the lowest-

energy state of the structure of the 1L-(1x1) (Eclipsed) unit cell. Color coding: Cu orange, O red, C cyan, and H white.

Table S6. Simulation analysis of the multilayer unit cell structures.

	Optimized cell parameters: a, b, c	In-plane shift	Relative	
System	(Ang)	Da, Db (Ang)	Energy* (eV)	Figure
1L-(1x1) (Eclipsed)	21.75, 21.75, 3.36	0.00, 0.00	+0.00	S37
2L-(1x1) Eclipsed	21.75, 21.75, 3.36*	0.00, 0.00	+0.13	S38
2L-(1x1) Rotated	21.71, 21.71, 3.27*	,	+0.13	S38
2L-(1x1) Translated #1	21.76, 21.76, 3.26*	1.26, 1.26	+0.00	S38
2L-(1x1) Translated #2	21.75, 21.74, 3.26*	3.64, 2.93	+0.28	S38
4L-(1x1) Eclipsed	21.77, 21.77, 3.38*	0.00, 0.00	+0.13	Not shown
4L-(1x1) Rotated	21.72, 21.72, 3,30*	,	+0.13	Not shown
4L-(1x1) Translated #1	21.76, 21.76, 3.28*	1.26, 1.26	+0.00	Not shown
4L-(1x1) ABCB stack	21.52, 21.53, 2.36*	,	+0.03	S38

^{*} Structural parameters and energy differences normalized to (1x1) cell. All the angles of the unit cells were fixed to (90,90,120).

In Cu-based 2D MOF systems, the limited long-range order along the *c*-direction is ascribable to the slipped-parallel packing arrangement. ^{15, 17, 18} To investigate this phenomenon at the DFT level, we resorted to larger unit cells containing two layers. The corresponding structures are shown in **Figure S59A**. In the case of the 2L-(1x1) cell, we first checked the local stability of the Eclipsed stacking mode; then, we locally simulated the stability of three different stacking organizations, two slipped-parallel and one rotated. The latter was identified in a Co-based 2D MOF with HTTP linkers. ¹⁹ The translated motif 2L-(1x1) Translated #1 has the lowest energy, confirming the tendency towards slipped-parallel arrangements. The favorable arrangement is due to the hollow position of the aromatic carbon atoms of the layers. Interestingly, the 2L-(1x1) rotated structure is isoenergetic with the eclipsed one, and both are near in energy to the preferred slipped-parallel arrangement.

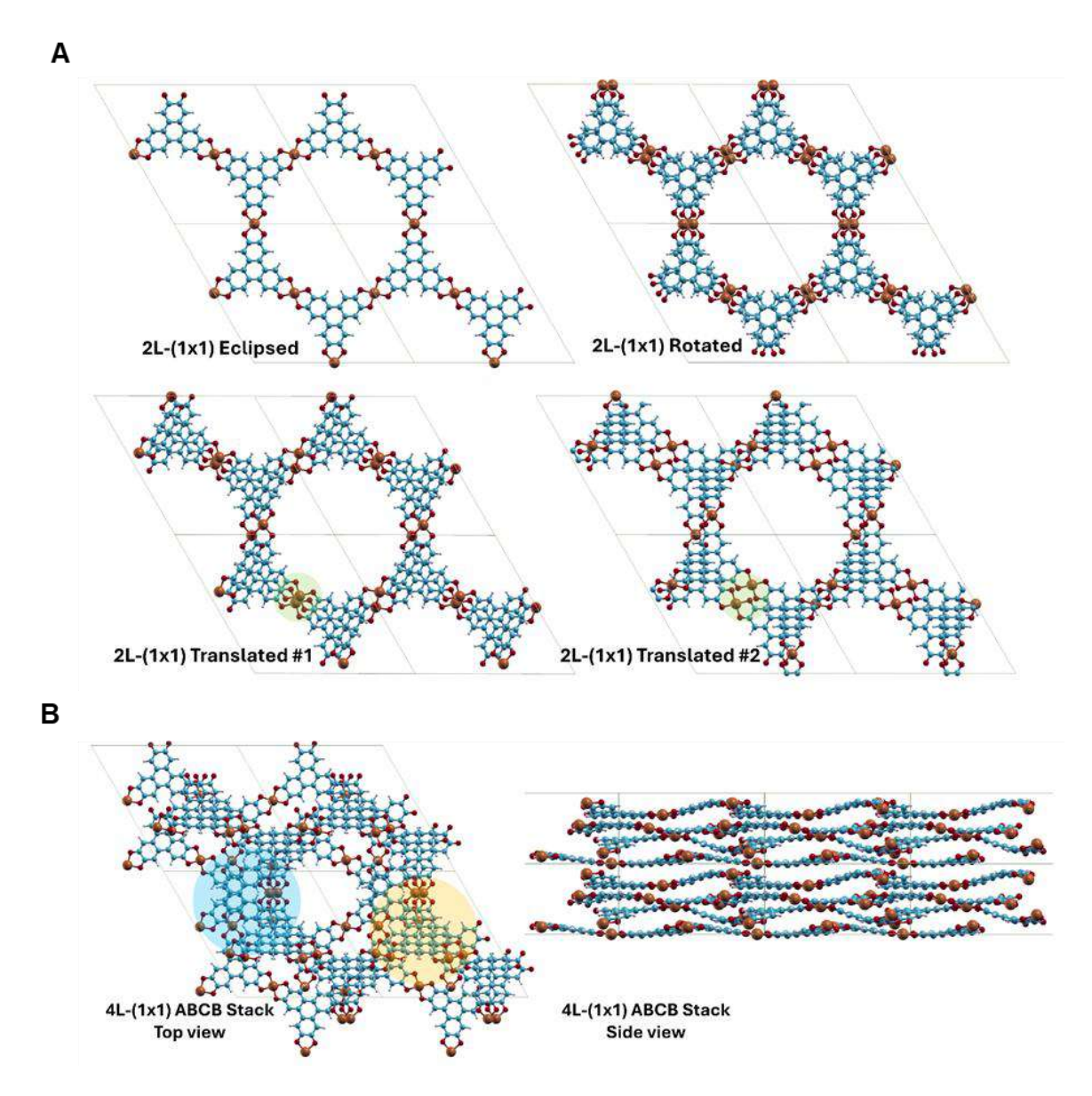


Figure S59. Stacking comparison of Cu₃(HHTP)₂ unit cells. Stacking sequences of different (1x1) structures with (A) 2 layers and (B) 4 layers, according to the terminology used in Table S6. The small green circles in the translated motifs indicate the two Cu atoms chosen for the translation vector. Color coding: Cu orange, O red, C cyan, and H white.

We disclosed the behavior of a larger portion of the material through RMD simulations. First, we examined the behavior of the empty MOF as a bulk material. We extracted a representative structure from the last portion of the production trajectory and compared the calculated XRD

spectra of the initial and final configurations (reduced set of atoms). The spectra and the corresponding geometries are shown in Figure S57. It is evident, from the widening of the XRD peaks (blue lines), that the ordered configuration, where all the stacked planes are eclipsed, thus HHTP molecules and copper atoms perfectly superimposed, is not maintained. Still, all the layers tended to reorganize their arrangements in response to the thermal perturbations and intermolecular interactions with the neighboring species. In agreement with the indications derived from the local optimizations at the quantum chemistry level on the small cells, these reorganizations include concerted translations and rotations of all the components that generated quite different types of patterns, as demonstrated by the inspection of the final stable assemblies sampled in the two examined cases. We compared the final models with configurations reported in the literature⁶ and found a satisfactory agreement with the pattern where similar shifts were observed. The inspection was extended to the bulk models filled with water and SO₂ and to the slab simulations. The same rearrangement took place in all the models, suggesting that thermal motion induces the displacement of the layers to improve the attractive interactions of the various species, including copper ions. All the final average equilibrium configurations preserved the shifted structures. A pictorial representation of this rearrangement is shown in **Figure S60A**, where only the copper atoms of the first three layers in contact with the graphitic plane of the 7L-(12x12) MOF cell are displayed. Starting from the first layer (blue), we recognize its characteristic Kagome pattern; the second layer (red), instead of being eclipsed or slightly shifted, is placed above the hollow positions of the first layer; the same for the third layer (green), giving rise to an ABC stacking sequence analogous to that of fcc crystals. An analysis of the successive layers reveals that this sequence is not perfectly regular, and some "stacking faults" are introduced. Examining the full 7L-(12x12) cell, the sequence resulted in ABCBABC; for the 20L-(4x4) cell, the sequence is shown in **Figure \$61**, exhibiting a quite homogeneous population distributed over the three different topological sites (A, B or C). In both cases, even though a long-range sequence ordering cannot be found, we never observe two eclipsed neighboring planes. Thanks to this reconstruction, in each MOF layer there exist areas, highlighted by using corresponding colors in Figure S60B, in

which the CuO₄ units are uncovered and much more exposed to interaction with the environment with respect to the eclipsed or slightly slipped-parallel patterns previously described.

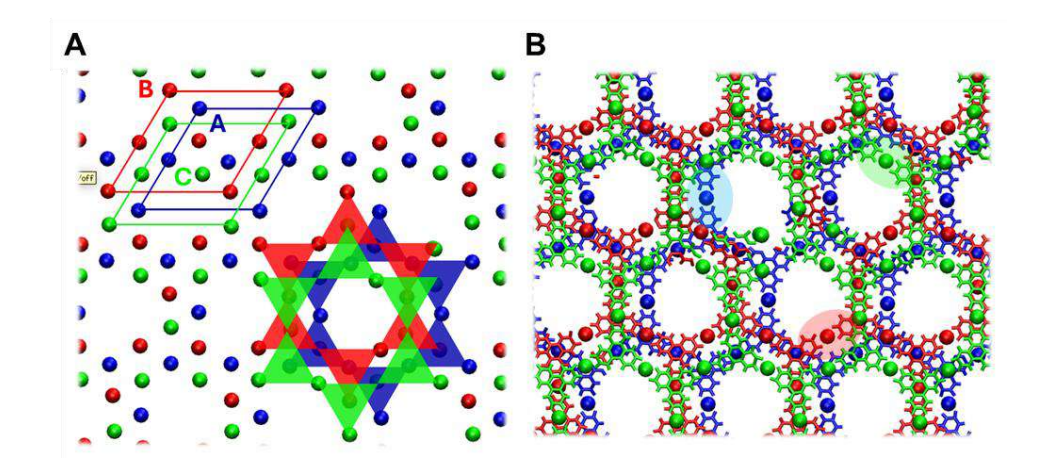


Figure S60. Illustration of the MOF rearranging layers. (A) Copper atoms belonging to the first three layers of the 7L-(24x24) MOF cell; the various layers are colored differently: the first layer is blue, the second is red, and the third is green. (B) The various layers where only C, H, and O atoms are displayed in bond and stick mode. The same color scheme is used.

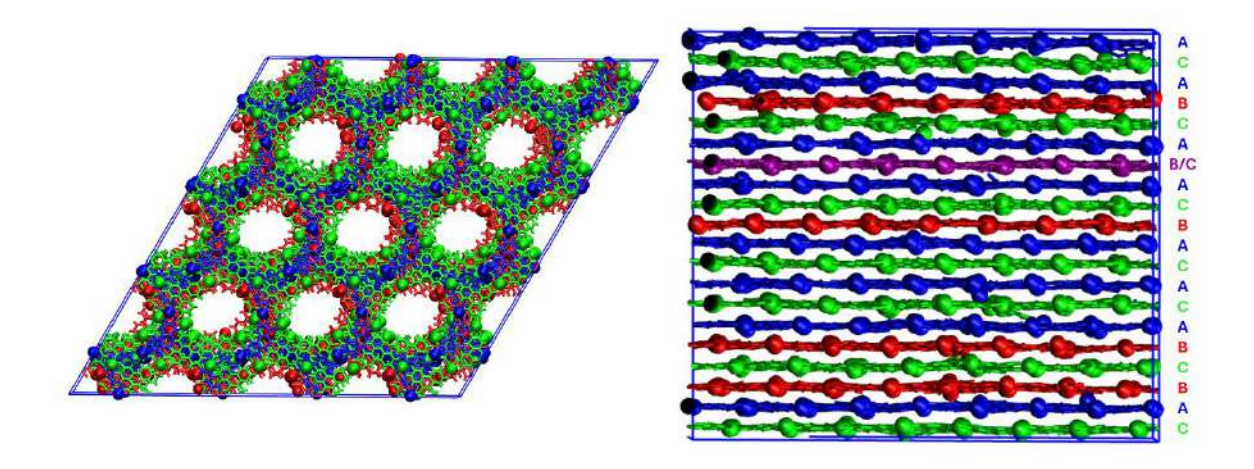


Figure S61. Illustration of the 20-L (8x8) cell structures. Different layers are colored with different colors: A layers in blue, B in red and C in green. Side view of the structure reports the layers stacking sequence.

We also proceeded to a DFT investigation of the new pattern, by choosing a 4L-(1x1) cell with a stacking sequence of the type ABCB, and performing a direct comparison with a 4L-(1x1)Translated #1 with a stacking sequence ABAB, achieved by doubling along z the 2L-(1x1) corresponding cell. Results are summarized in Table S6, and the relaxed structure of the new 4L-(1x1) ABCB stack is shown in Figure S59B. The relaxed structure of 4L-(1x1)Translated #1 is not reported as it qualitatively and semi-quantitatively agreed with that optimized in the smaller cell. As it can be observed in the top view, the DFT-relaxed structure of the 4L-(1x1) ABCB stack presents features that can also be found in the stacking sequences of the motifs previously investigated: the two B layers, thanks to the corrugation of the structure, manage to approach in some regions of the unit cell, highlighted with an orange circle, adopting a structure very similar to that observed in the 2L-(1x1) Rotated one; similarly, A and C layers slightly shift and manage to approach in the region highlighted with the blue circle, adopting a quasi-eclipsed configuration with an approximate distance of 3.3 Angstrom (close to the inter-layer distance in eclipsed stacking sequences). These features are probably due to the "tight" boundary conditions of the DFT unit cell; consistently, at the RMD level we observed a qualitative difference between 7L-(12x12) and 20L-(4x4) cells, with the larger cell behaving more regularly thanks to the possibility of relaxing the structure on a larger scale in response to structural rearrangement. We cannot directly verify this hypothesis, as larger cells were prohibitive due to their huge computational effort at the DFT level. Looking at the energy, we can see that the ABCB stack is in close competition with the Translated #1 structure. Overall, these results confirm a high fluxionality of the structure along the direction perpendicular to the planes, where, in fact, van der Waals forces dominate inter-layer interaction and can promote the competition between many possible stacking sequences, in agreement with the poor long-range order along the z direction which is experimentally observed.

The relative position of the copper ions in all the examined MOF situations, namely bulk and slab, empty and totally/partially filled with water and SO₂ molecules, was analyzed by

checking the trend of the radial distribution functions on the final 100 ps of the production trajectories (**Figure S62**). All the plots of the empty and filled with water bulk material show a high sharp peak at about 5.7 Å and lower broader peaks at about 7.3 ± 0.4 Å, suggesting that water molecules do not significantly perturb the metal centers and the surrounding species. The inactivity of water is also confirmed by the trend of the Cu-Cu RDF of the water-solvated MOF slab, which displays very similar peaks. Instead, the Cu-Cu RDFs of the MOF filled with SO_2 show only one high broader peak at approximately 6.8 Å, suggesting that these molecules could interact directly or indirectly with the metal sites and induce different relocations. After drying, only 20% of the initial water remained in the deposited material, and the adsorbed SO_2 content was dominant (more than twice the amount of water, coherently with the estimate of DFT interaction energy of the two guest species). This explains why, in the mixed case, the Cu-Cu RDF trend is dominated by the SO_2 species (**Figure S62**). Even though water molecules are mainly located within 6 Å of the frozen plane (**Figure S63**), they diffuse in the channels and interact with both the HHTP and SO_2 oxygens (**Figure S64**).

We estimated the diffusion coefficient of water and SO₂ in the case of mixed guests and when the MOF was filled with SO₂ molecules only at a double concentration and found values of approximately 7.4 x 10⁻⁸ m²/s, 2.2 x 10⁻⁸ m²/s, and 1.3 x 10⁻⁸ m²/s, respectively. The data and visual examination of the sampled configurations indicate that water molecules could act as mediators in the connections of the SO₂ molecules to the MOF structure. A typical arrangement is shown in Figure S45, where an SO₂ molecule seems coordinated to a copper atom at a relatively long separation and is kept there by hydrogen bonds with a water molecule and with the hydrogens of the HHTP units. The HHTP connections to the Cu metal centers seem quite stable, and no replacements were observed during the dynamics. As is apparent from the molecular surface representations in **Figures S65** and **S66**, most of the guests remained close to the walls of the channels. To estimate the extent of agreement between the predictions of ReaxFF and DFT in describing the sensing properties of the material after structural rearrangement, we performed local DFT optimizations of the 4L-(1x1) ABCB cell in the presence of water and/or SO₂ guest species.

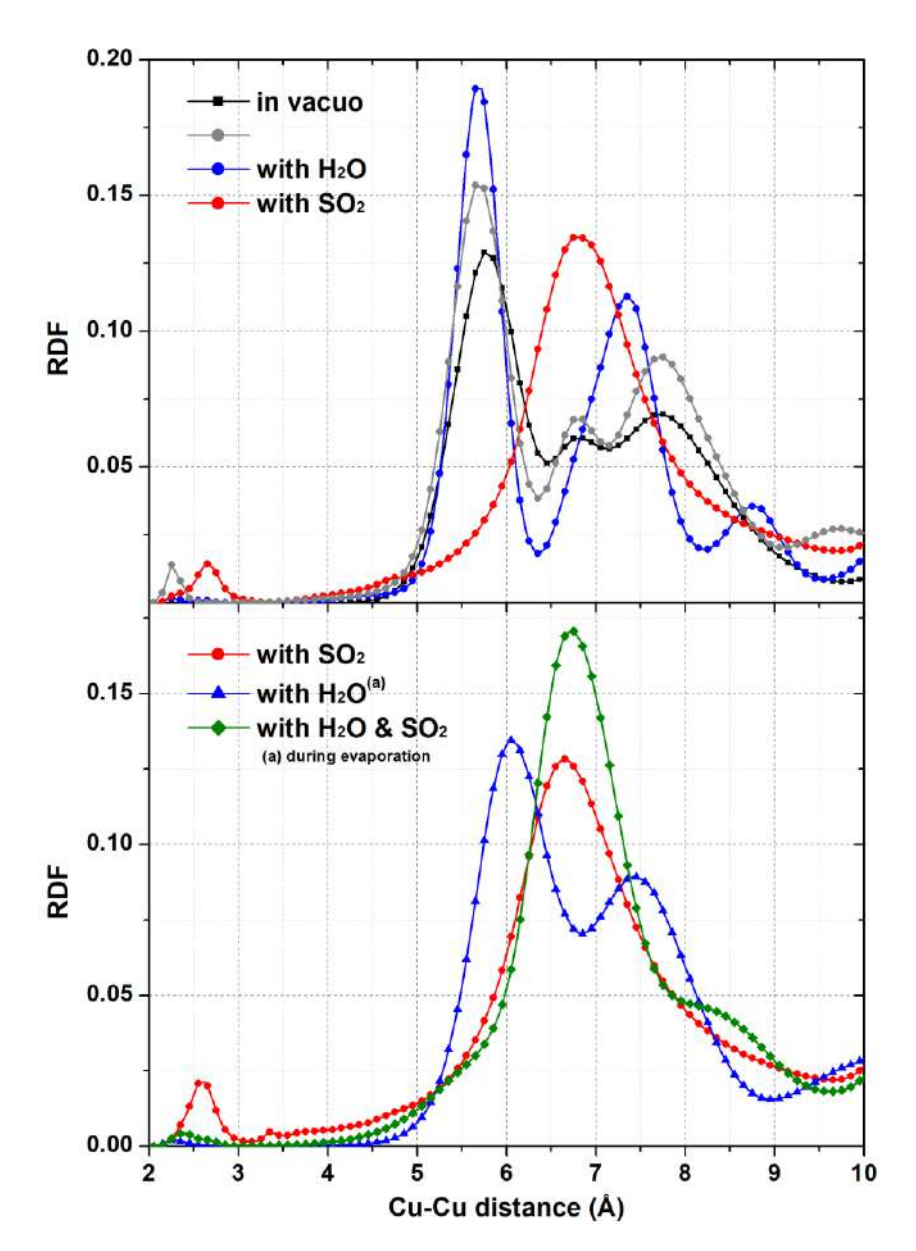


Figure S62. Atom-atom RDFs describing the relative positions of the copper atoms in different simulation conditions. Simulations of the bulk material with periodic boundary conditions in x, y, and z directions (top), and simulations of the material on the textile (graphitic plane – frozen) (bottom). Periodic boundary conditions are applied only in the x and y directions.

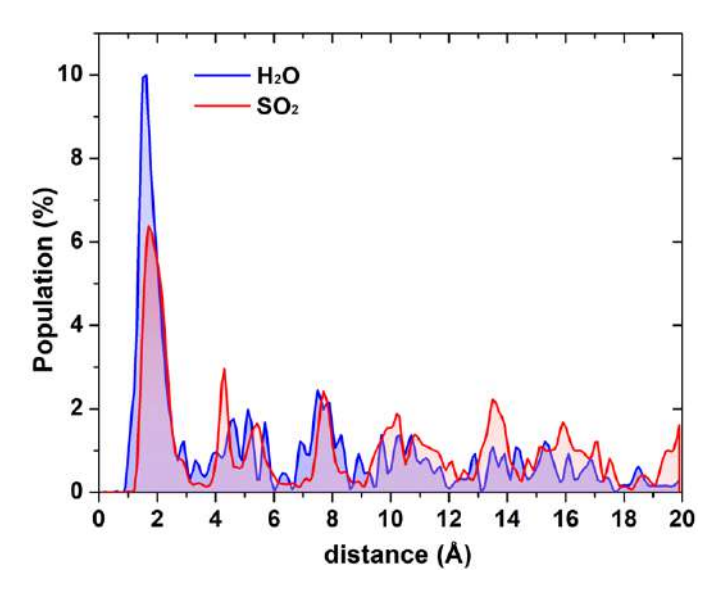


Figure S63. Distributions of water and SO₂ inside the channels as a function of the distance from the frozen plane.

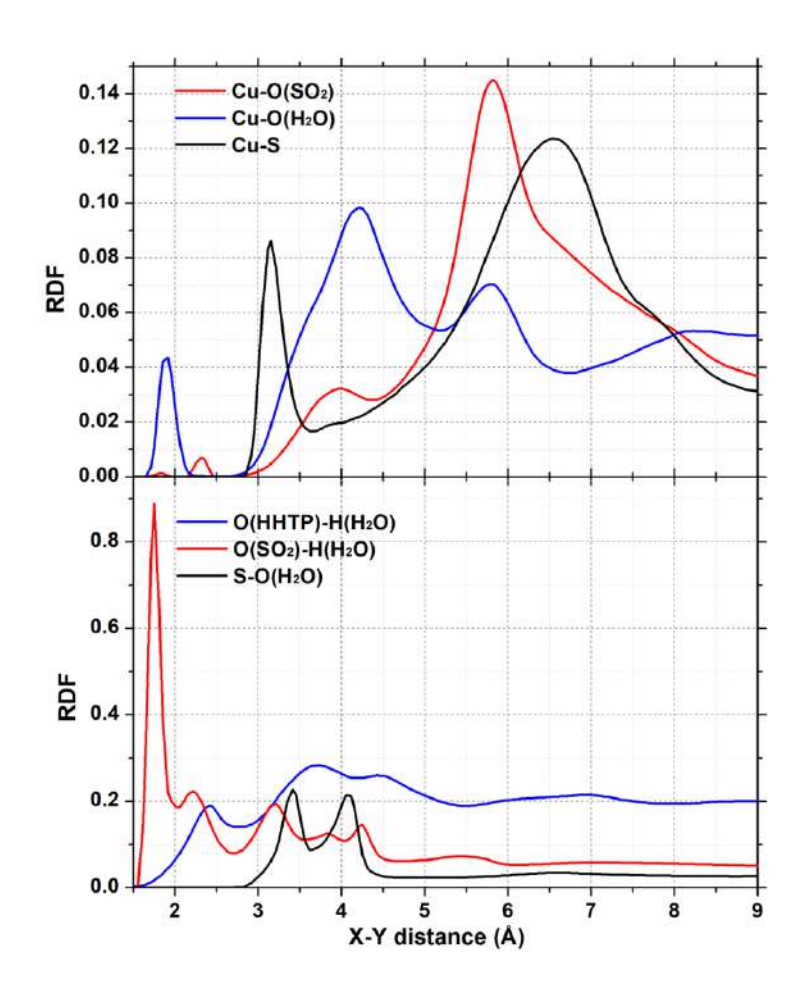


Figure S64. Atom-atom RDFs describing the relative positions of the various species in the mixed water-SO₂ simulation of the material absorbed on textile.

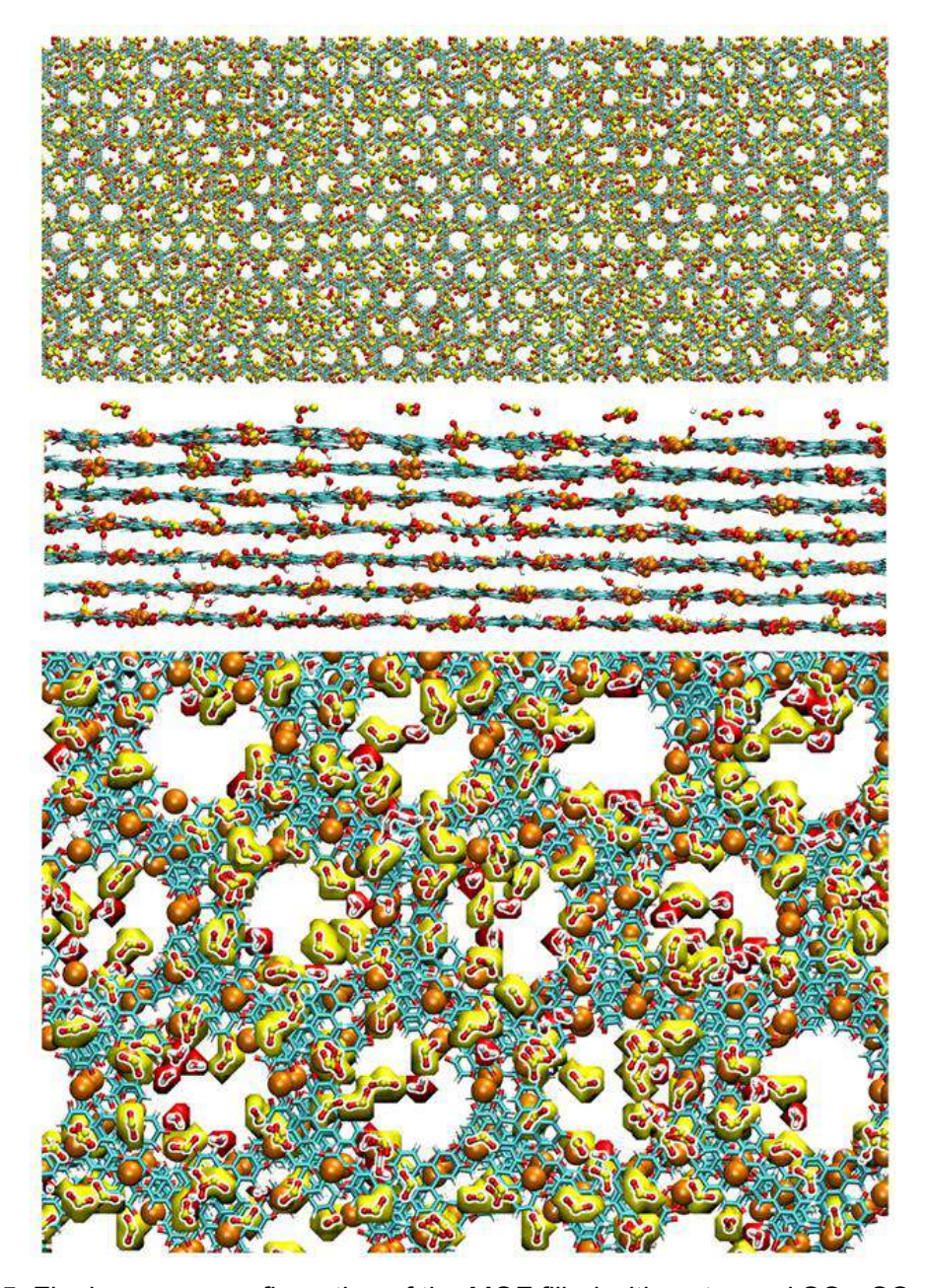


Figure S65. Final average configuration of the MOF filled with water and SO₂. SO₂ and water molecules are yellow and red contours.

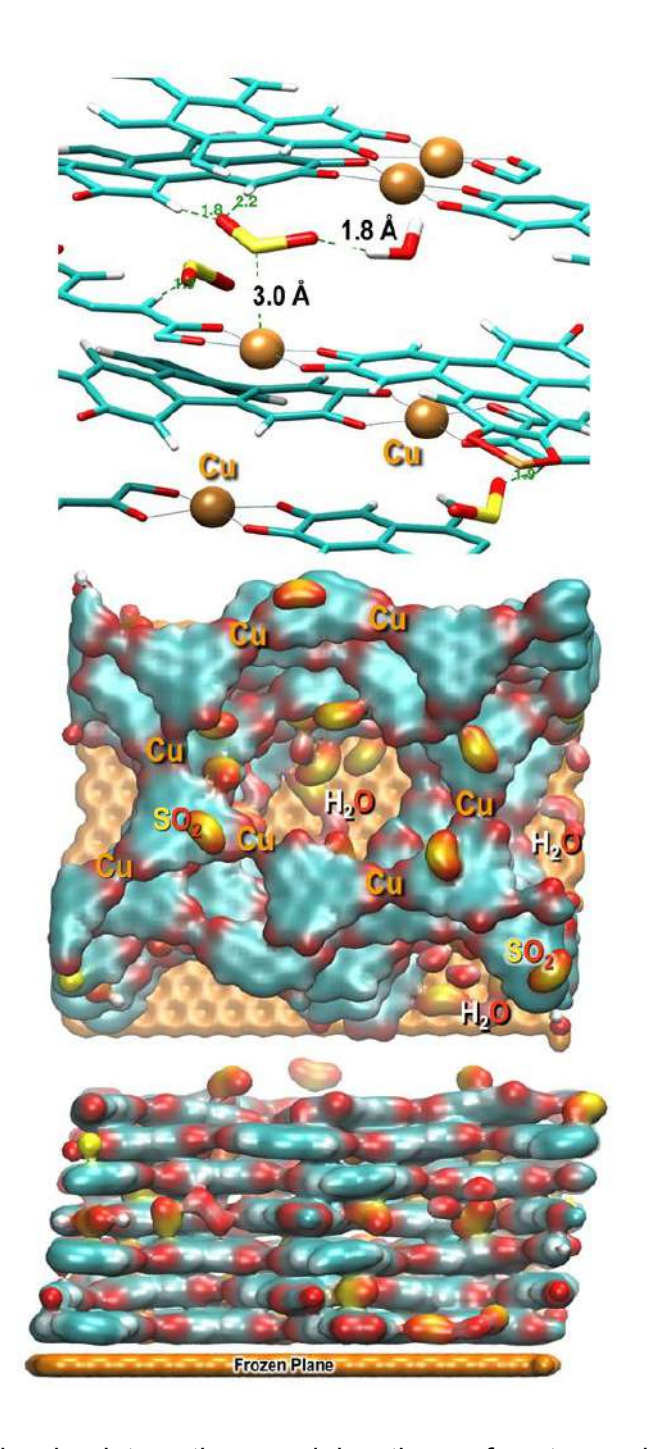


Figure S66. Intermolecular interactions and locations of water and SO₂ guests in the channels.

We selected the preferred slipped-parallel structure (2L-(1x1) Translated #1) to study the adsorption properties of H_2O and SO_2 at the QM level of theory. The two guest molecules were investigated separately via local DFT optimizations. We found that, in both cases, the guest species absorbed in the neighborhood of the metal core of the MOF structure. Several

configurations have a similar total energy, indicating different coexisting arrangements governed by both van der Waals and hydrogen bonding interactions. Two characteristic adsorption energies are reported together with the corresponding equilibrium structures (**Figure S67**). The energy values show a slightly stronger interaction of SO_2 with the MOF framework compared to the interaction of MOF and water. Water molecules could be found close to Cu atoms and hydrogen bonded to the oxygens of HHTP. The equilibrium distance between Cu and O_{wat} is 2.35 Å, whereas the H_{wat} - O_{MOF} distance is approximately 1.85 Å (**Figure S67A**). On the contrary, SO_2 is slightly farther from the MOF planes with characteristic S- O_{MOF} distances of roughly 2.95 Å and O_{SO2} – H_{MOF} distances of about 2.45Å (**Figure S59B**).

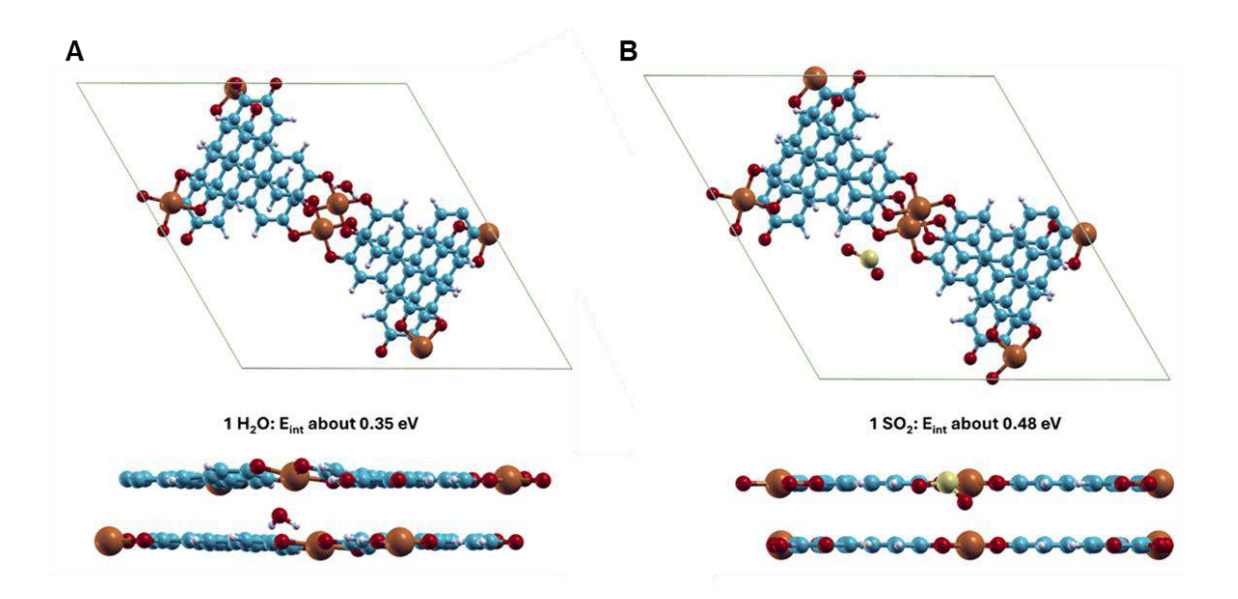


Figure S67. Equilibrium structures and adsorption energies of MOF with H₂O and SO₂. Top and side views of (A) one H₂O and (B) one SO₂ molecule in two characteristic adsorption geometries near the MOF structure. Color coding: Cu is orange, O red, C cyan, S yellow, and H white.

When both SO₂ and H₂O are present in the framework, they can interact favorably with each other even at low concentrations, and the resulting potential energy surface is relatively flat (Figure S68A). The generated configuration was found to follow a reaction path corresponding

to the oxidation of SO₂ promoted via reaction with H₂O. The reaction can be divided into two steps involving one water molecule in each step. In the first step, the first H₂O molecule is "adsorbed" on SO₂, forming H₂SO₃. The H₂SO₃ structure interacts with the MOF via two hydrogen bonds. The initial and final structures in the first step have similar energy and are separated by an energy barrier of around 1.4 eV. The transition state is governed by a hydrogen transfer from H₂O to SO₂. In the second step, the oxidation proceeds through a reaction with a second water molecule, and the final products consist of a charged HSO₄accompanied by the migration of two hydrogens, and a proton to the vicinal oxygens of the MOF structure. This second step is characterized by a lower energy barrier (about 0.7 eV). The transition state is governed by the transfer of hydrogens/protons between the HSO₄- and the MOF. The MOF plays both an indirect and direct role in this process. In the first step, it anchors the two reactant species to its walls, whereas in the second step, it links three extra hydrogens/protons of the reactions via the creation of three OH groups bound to the Cu atoms, two on one MOF layer and the third on a vicinal one. To visualize the electronic structure of the MOF, we examined the projected density of states (PDOS) for the 3d bands of Cu atoms bound to two or one OH groups. From the PDOS of the 3d bands of the Cu atoms bound to two OH groups (left panel of Figure S68B), it is evident that the Cu atom involved in this interaction is reduced compared to the Cu atoms not interacting with guest species. This is indicated by the shift of the empty Cu 3d band of the reduced atom toward lower energies, positioning it just above the Fermi level. On the other hand, this effect is less pronounced for the Cu atom bound to only one OH group (right panel of Figure S68B). The energy difference between the empty 3d band of the reduced Cu and that of the oxidized Cu is smaller in this case than when two OH groups are bound.

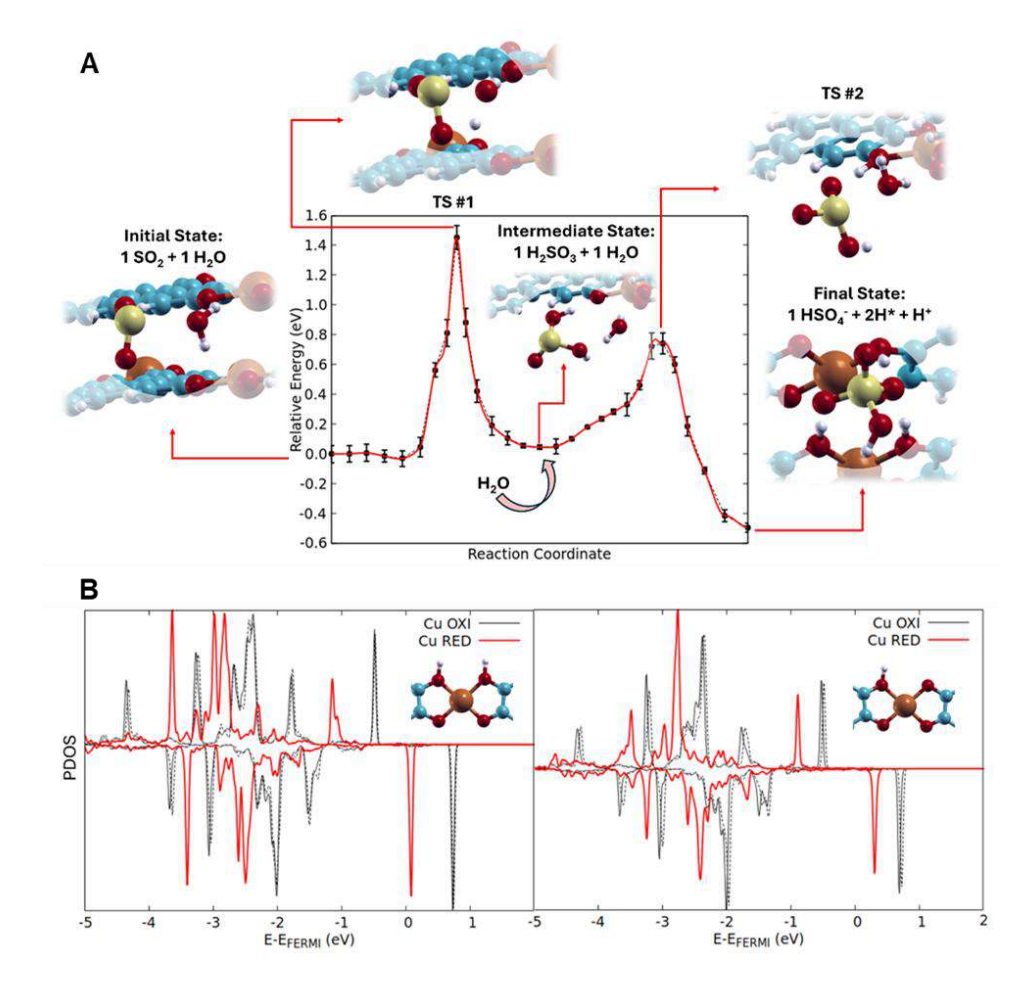


Figure S68. Simulation of the reaction pathway and products of Cu₃(HHTP)₂ MOF with SO₂ and H₂O. (A) Simulated potential energy profile corresponding to the reaction of one SO₂ molecule with a first H₂O molecule to provide H₂SO₃ and then to provide H₂SO₄ and 2 H atoms adsorbed (*) on the nearby MOF structure after adsorption of a second H₂O molecule. Color coding: Cu orange, O red, C cyan, S yellow, and H white. (B) Majority and minority PDOS of the Cu 3d bands of the two layers (left and right panels, respectively) of the MOF in the unit cell, corresponding to the final state of the reaction: black lines correspond to oxidized Cu atoms, where red lines to the Cu atoms bound to OH groups.

6. Adsorption study

6.1. Isotherm experiments

SO₂ adsorption isotherms were measured at 298 K on a gravimetric sorption analyzer (SMS, DVS Vacuum) using high-purity SO₂ gas (Infra, 99.5%). Before adsorption experiments, samples were activated at 373 K under a dynamic vacuum (10⁻³ bar) for 2 h. SO₂ adsorption/desorption cycles were conducted at 298 K. Before adsorption experiments began, the sample was activated at 373 K under a dynamic vacuum for 2 h. In between cycles, the regeneration step was thermal activation at 373 K under a dynamic vacuum for 1 h. The adsorption kinetics of SO₂ were evaluated on the Cu₃(HHTP)₂@textile sample by exposing a constant pressure of 100 and 1000 ppm SO₂ and collecting the gravimetric SO₂ adsorption over time. Before measurements, the samples were activated under a dynamic vacuum (1 x 10⁻⁶ Torr) at 373 K for 4 h.

Table S7. Selected data for SO₂ adsorption of textiles at 298 K.

SO₂ uptake (mmol g⁻¹)

Sample	0.01 bar	0.1 bar	1.0 bar
cotton textile	0.013	0.019	0.026
Cu(OH) ₂ @textile	0.029	0.073	0.269
Cu ₃ (HHTP) ₂ @textile	0.191	0.390	0.830
Cu ₃ (HHTP) ₂ powder	0.304	0.843	1.887

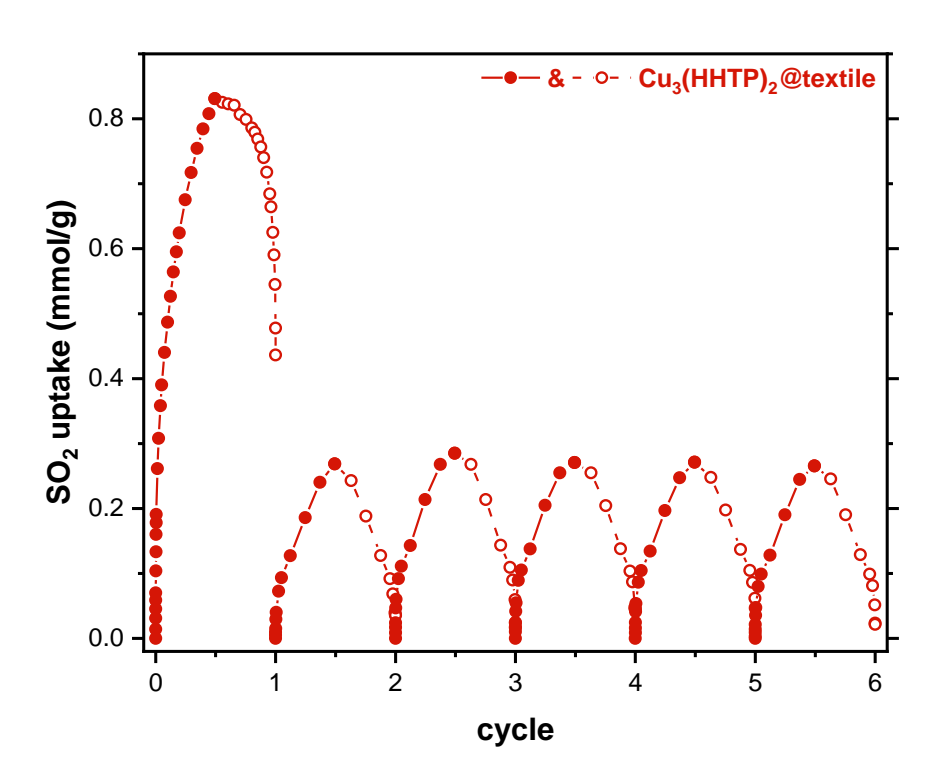


Figure S69. SO₂ adsorption cycles of Cu₃(HHTP)₂@textile at 298 K. Thermal activation step at 373 K under vacuum for 1 hour was applied to regenerate the sample between each adsorption cycle.

Table S8. Selected data for SO₂ adsorption cycles of Cu₃(HHTP)₂@textile at 298 K.

Cycle	SO₂ uptake (mmol g⁻¹)			
·	0.01 bar	0.1 bar	1.0 bar	
1 st	0.191	0.390	0.830	
2 nd	0.040	0.094	0.269	
3 rd	0.060	0.111	0.285	
4 th	0.055	0.105	0.271	
5 th	0.054	0.104	0.271	
6 th	0.047	0.099	0.266	

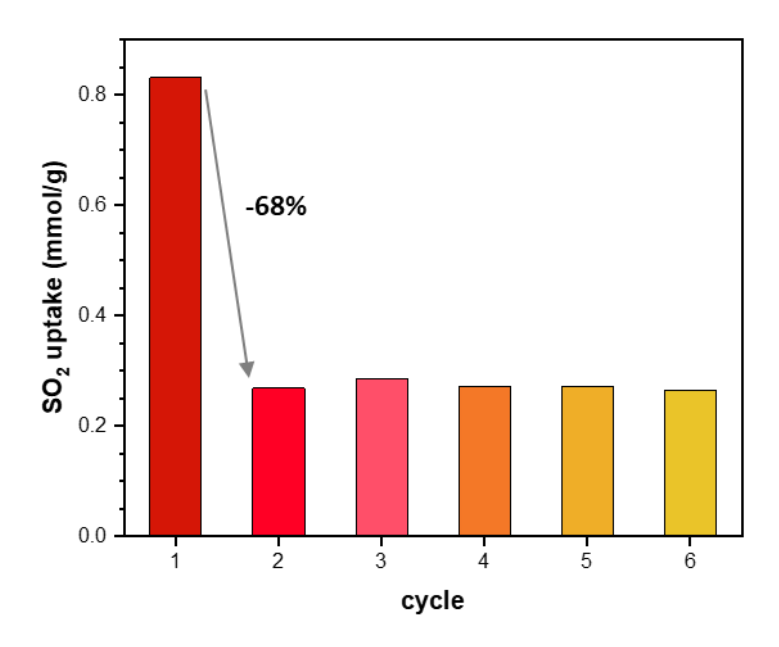


Figure S70. SO₂ adsorption cycles of Cu₃(HHTP)₂@textile. The sample was thermally regenerated between cycles.

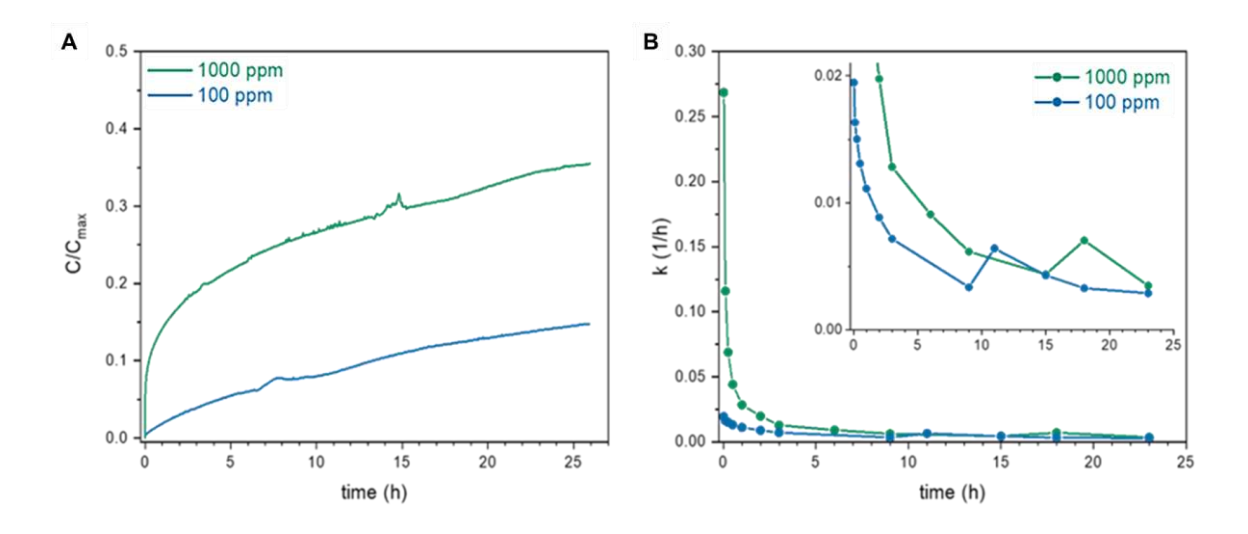


Figure S71. Kinetic analysis of Cu₃(HTTP)₂@textile absorbing SO₂. (A) Kinetic adsorption profile of Cu₃(HTTP)₂@textile with 100 and 1000 ppm SO₂. (B) Kinetic adsorption constants of Cu₃(HTTP)₂@textile with 100 and 1000 ppm SO₂ over time with an inset figure showing the pseudo-steady state beginning after around 10 h.

By evaluating the kinetic adsorption data with the zero, first, and second-order reactions, we found that the data followed the zero-order reaction model (Equation 9), where k

represents the kinetic constant (h^{-1}), and (C/C_{max})₀ represents the initial concentration normalized to the maximum uptake from the static isotherm data, 0.838 mmol g⁻¹ at 1 bar and 298 K.

$$C/C_{max} = k \cdot t + (C/C_{max})_0$$
 Equation 9

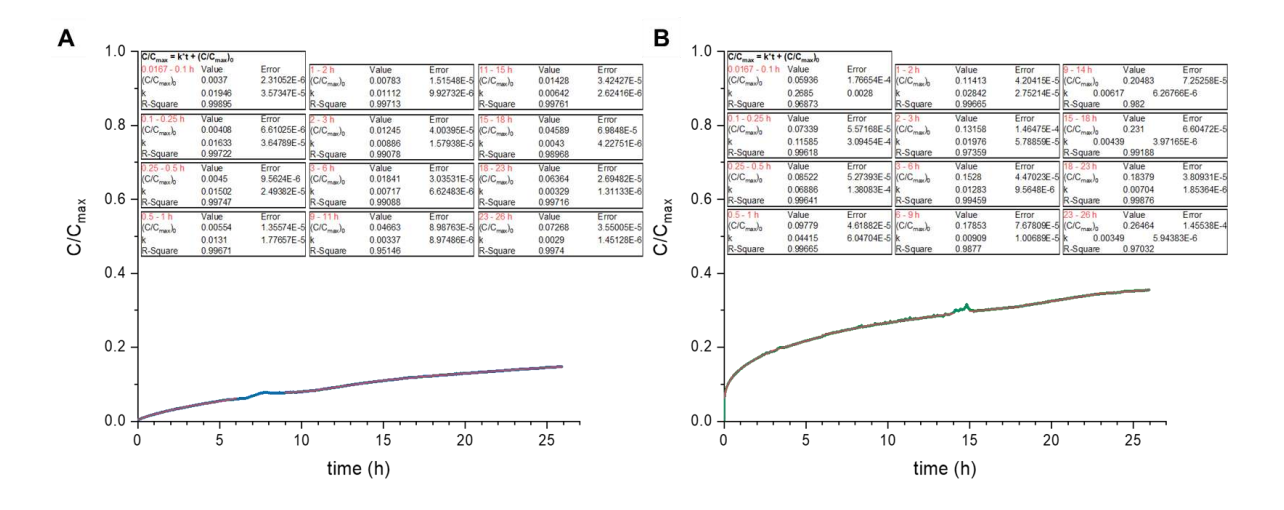


Figure S72. Fitting of kinetic profile. Kinetic adsorption profiles of Cu₃(HTTP)₂@textile with (A) 100 and (B) 1000 ppm SO₂ that fit into a zero-order model at different time intervals.

Table S9. Summary of the kinetic studies for SO₂ adsorption using Cu₃(HTTP)₂@textile with 100 and 1000 ppm SO₂.

	Static isotherm data		Ki	netic data∘		
\$O₂	SO ₂ uptake ^a	Saturation time	Initial state (0.0167 – 0.1 h)		Pseudo-steady state (23 – 26 h)	
concentration	[IIIIIIOI g ·]	[h]/[days]	k [h-1]	(C/C _{max}) ₀	k [h-1]	$(C/C_{max})_0$
100 ppm	0.028	319.7 / 13.3	0.019	0.0037	0.0029	0.073
1000 ppm	0.069	210.7 / 8.8	0.27	0.059	0.0035	0.26

^a Values calculated from collected experimental data at 298 K and fitted into the dual-site Freundlich-Langmuir model. ^b Values estimated from the kinetic constant at the pseudo-steady state. ^c Concentration values are normalized to the maximum SO_2 uptake of 0.838 mmol g^{-1} at 1 bar.

SO₂ isotherm data of Cu₃(HTTP)₂@textile was fitted into the dual-site Freundlich-Langmuir (DSFL) model using Equation 10, in order to obtain the maximum uptake at relevant low-pressure values: 0.028 and 0.069 mmol/g for 100 and 1000 ppm SO₂, respectively.

$$n = \frac{a \cdot b \cdot p^{c}}{1 + b \cdot p^{c}} + \frac{a_{1} \cdot b_{1} \cdot p^{c_{1}}}{1 + b_{1} \cdot p^{c_{1}}}$$
 Equation 10

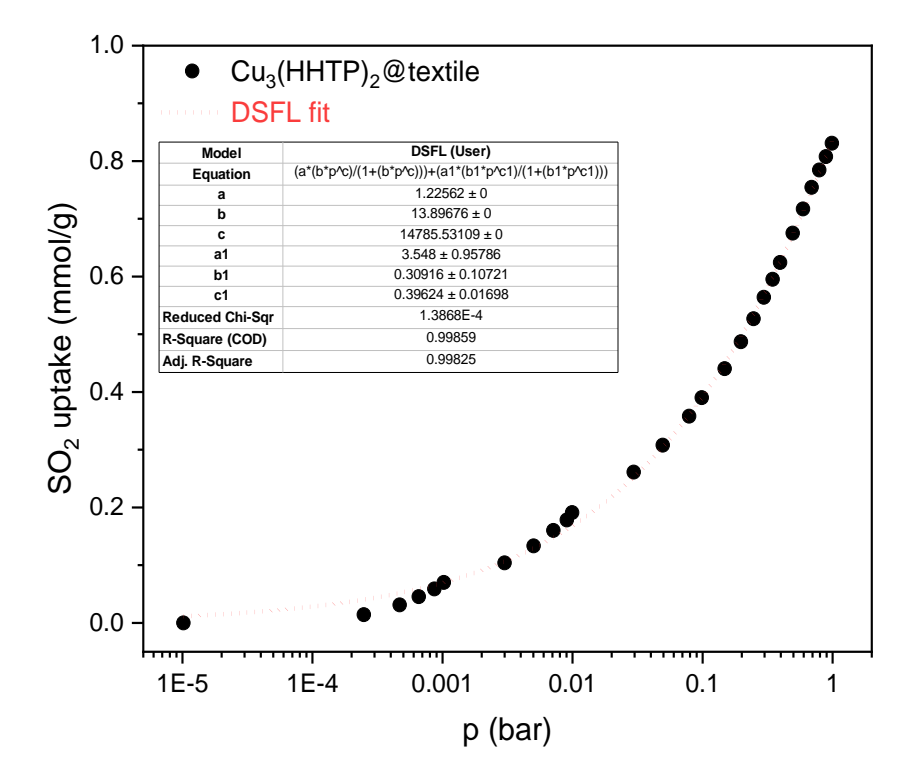


Figure S73. Dual-Site Freundlich-Langmuir fitted adsorption isotherm of Cu₃(HTTP)₂@textile at 298 K.

6.2. Micro-breakthrough experiments

MOF/textile composites and MOF powder samples were evaluated for SO₂ uptake in milligram scale quantities using a breakthrough apparatus as described thoroughly elsewhere.^{20, 21} To summarize, a 4 mm diameter fritted glass tube was fitted with ~10 mg of material. Samples were conditioned with dry air at 100 °C to remove any absorbed water. If

the sample required a humid test environment, the sample was then conditioned at 20 °C with humid air (RH = 80%). A gas stream of dry (or humid) house air and diluted SO₂ achieved a feed stream of 20 SCCM at 1000 mg m⁻³ of SO₂. The stream was fed to the textiles while the effluent was monitored continuously using a flame photometric detector until saturated. The chemical capacity of the textile was calculated by subtracting the effluent curve integral from the integral of the feed stream. The feed stream is assumed to be a square wave function.

Table S10. SO₂ uptake of Cu₃(HHTP)₂@textile and Cu₃(HHTP)₂ powder through microbreakthrough experiments.

Material	Sample type	SO₂ upta	SO₂ uptake (mmol/g)		
Material	Sample type	Dry	Humid (RH=80%)		
Cu ₃ (HHTP) ₂ @textile	MOF/textile	0.15 ± 0.07	0.26 ± 0.11		
Cu ₃ (HHTP) ₂ powder	MOF powder	0.62 ± 0.04	0.87 ± 0.05		

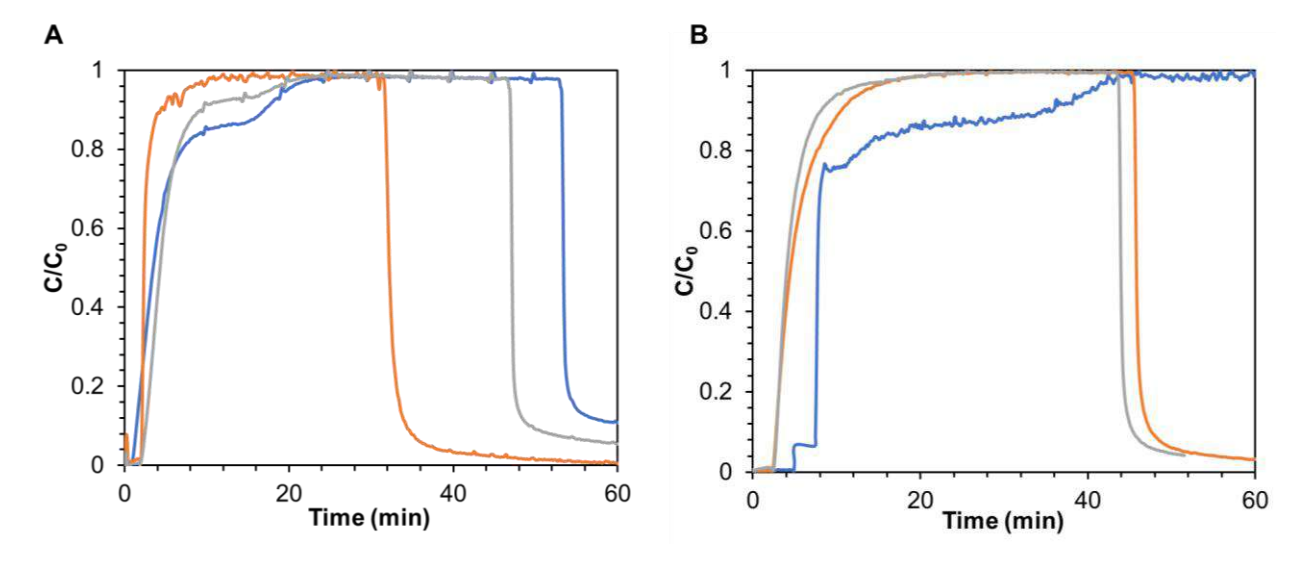


Figure S74. Micro-breakthrough results of Cu₃(HHTP)₂@textile. (A) Micro-breakthrough curves of Cu₃(HHTP)₂@textile for SO₂ uptake in dry air with three independent trials. (B) Micro-

breakthrough curves of $Cu_3(HHTP)_2$ @textile for SO_2 uptake in humid air (RH = 80%) with three independent trials. The observed variations in curve shape and uptake values are due to (1) the inherent associated error of the breakthrough testing method, and (2) partial flake-off of MOF powder during the measurements.

7. Mask demonstration

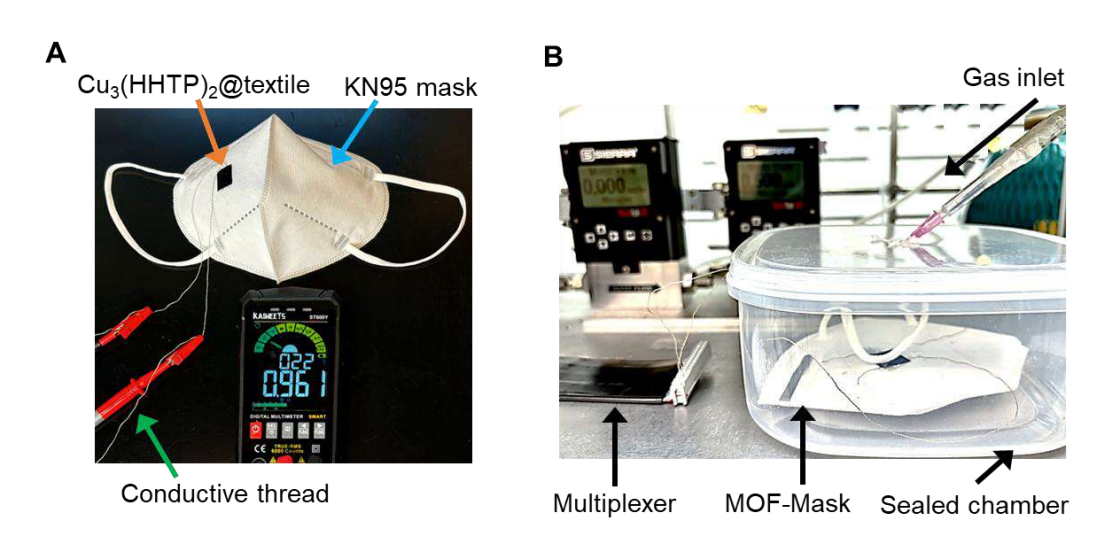


Figure S75. The MOF-mask prototype for SO₂ sensing. Photographic illustration of the (A) MOF-mask prototype and (B) sensing set-up. A 1.5 cm ×1.5 cm piece of Cu₃(HHTP)₂@textile was glued onto the outer surface of a KN95 mask using silver paste. Two conductive silver-coated polyamide/nylon6,6 threads were also glued between the Cu₃(HHTP)₂@textile and the mask fabric. The MOF-Mask was placed and sealed in a plastic chamber connected to the gas mass flow controller through tubing and syringe to allow gas to flow into the chamber. The MOF-Mask was connected to a potentiostat by inserting the conductive threads into the pins of a multiplexer to collect the raw current data under 1.0 V applied voltage.

Table S11. Summary of scalable fabrication for MOF/textile composites

	MOF layer composition	Fabrication technique	Textile type and area	MOF loading	Application
This work	Cu ₃ (HHTP) ₂	Templated synthesis	10 cm x 10 cm polyester	38 wt.% 5.05 mg/cm ²	Gas sensing and filtration
ref ²²	ZIF-8/ polyacrylonitrile	Electrospinning method	20 cm x 20 cm polyethylene terephthalate	60 wt.%	Particulate matter (PM) filtration
ref ²³	ZIF-8	Layer-by-layer hot pressing	50 cm x 10 cm glass cloth	9.76 g/m²	As(V) filtration
ref ²⁴	MOF-808/ polyethylenimine	Dip-coating method	30 cm x 30 cm cotton	12 wt.%	Nerve agent hydrolysis
ref ²⁵	MOF-808	Solvothermal synthesis	10 cm × 120 cm polyethylene terephthalate	22 wt.%	Chemical warfare agent hydrolysis
ref ²⁶	Ni ₃ (HHTP) ₂	Electrospinning method	100 cm² polyacrylonitrile	N/A	PM filtration and humidity monitor

References

- 1. Espejo, E. M. A., Balela, M. D. L. (2017). Facile synthesis of cupric hydroxide and cupric oxide on copper foil for potential electrochemical applications. lop Conf Ser-Mat Sci 201. 012050. 10.1088/1757-899x/201/1/012050.
- 2. Eagleton, A. M., Ko, M., Stolz, R. M., Vereshchuk, N., Meng, Z., Mendecki, L., Levenson, A. M., Huang, C., MacVeagh, K. C., Mahdavi-Shakib, A.; et al. (2022). Fabrication of Multifunctional Electronic Textiles Using Oxidative Restructuring of Copper into a Cu-Based Metal-Organic Framework. J. Am. Chem. Soc. 144, 23297-23312. 10.1021/jacs.2c05510.
- 3. Smith, M. K., Mirica, K. A. (2017). Self-Organized Frameworks on Textiles (SOFT): Conductive Fabrics for Simultaneous Sensing, Capture, and Filtration of Gases. J. Am. Chem. Soc. 139, 16759-16767. 10.1021/jacs.7b08840.
- 4. Mitchell, H. T., Smith, M. K., Blelloch, N. D., Van Citters, D. W., Mirica, K. A. (2017). Polycyclic Aromatic Hydrocarbons as Sublimable Adhesives. Chem. Mater. 29, 2788-2793. 10.1021/acs.chemmater.6b04641.
- 5. Kharin, A. Y., Assilbayeva, R. B., Kargina, Y. V., Timoshenko, V. Y. (2019). Comparative analysis of silicon nanostructures by x-ray diffraction technique. IOP Conf. Ser. Mater. Sci. Eng. 475. 10.1088/1757-899x/475/1/012010.
- 6. Gittins, J. W., Balhatchet, C. J., Fairclough, S. M., Forse, A. C. (2022). Enhancing the energy storage performances of metal-organic frameworks by controlling microstructure. Chem. Sci. 13, 9210-9219. 10.1039/d2sc03389e.
- 7. Giannozzi, P., Andreussi, O., Brumme, T., Bunau, O., Buongiorno Nardelli, M., Calandra, M., Car, R., Cavazzoni, C., Ceresoli, D., Cococcioni, M.; et al. (2017). Advanced capabilities for materials modelling with Quantum ESPRESSO. J. Phys. Condens. Matter 29, 465901. 10.1088/1361-648X/aa8f79.
- 8. Kresse, G., Joubert, D. (1999). From ultrasoft pseudopotentials to the projector augmented-wave method. Physical Review B 59, 1758-1775. 10.1103/PhysRevB.59.1758.
- 9. Grimme, S., Antony, J., Ehrlich, S., Krieg, H. (2010). A consistent and accurate ab initio parametrization of density functional dispersion correction (DFT-D) for the 94 elements H-Pu. J. Chem. Phys. 132, 154104. 10.1063/1.3382344.
- 10. Frisch, M. J. T., G. W.; Schlegel, H. B.; Scuseria, G. E.; Robb, M. A.; Cheeseman, J. R.; Scalmani, G.; Barone, V.; Petersson, G. A.; Nakatsuji, H.; Li, X.; Caricato, M.; Marenich, A. V.; Bloino, J.; Janesko, B. G.; Gomperts, R.; Mennucci, B.; Hratchian, H. P.; Ortiz, J. V.; Izmaylov, A. F.; Sonnenberg, J. L.; Williams-Young, D.; Ding, F.; Lipparini, F.; Egidi, F.; Goings, J.; Peng, B.; Petrone, A.; Henderson, T.; Rana-singhe, D.; Zakrzewski, V. G.; Gao, J.; Rega, N.; Zheng, G.; Liang, W.; Hada, M.; Ehara, M.; Toyota, K.; Fukuda, R.; Hasegawa, J.; Ishida, M.; Nakajima, T.; Honda, Y.; Kitao, O.; Nakai, H.; Vreven, T.; Throssell, K.; Montgom-ery, J. A., Jr.; Peralta, J. E.; Ogliaro, F.; Bearpark, M. J.; Heyd, J. J.; Brothers, E. N.; Kudin, K. N.; Staroverov, V. N.; Keith, T. A.; Kobayashi, R.; Normand, J.; Raghavachari, K.;
- Rendell, A. P.; Burant, J. C.; Iyengar, S. S.; Tomasi, J.; Cossi, M.; Millam, J. M.; Klene, M.; Adamo, C.; Cammi, R.; Ochterski, J. W.; Martin, R. L.; Morokuma, K.; Farkas, O.; Foresman, J. B.; Fox. D. J. Gaussian, Inc., 2016.
- 11. Zhu, C., Monti, S., Mathew, A. P. (2018). Cellulose Nanofiber-Graphene Oxide Biohybrids: Disclosing the Self-Assembly and Copper-Ion Adsorption Using Advanced Microscopy and ReaxFF Simulations. ACS Nano 12, 7028-7038. 10.1021/acsnano.8b02734.

- 12. Valencia, L., Monti, S., Kumar, S., Zhu, C., Liu, P., Yu, S., Mathew, A. P. (2019). Nanocellulose/graphene oxide layered membranes: elucidating their behaviour during filtration of water and metal ions in real time. Nanoscale 11, 22413-22422. 10.1039/c9nr07116d.
- 13. Thompson, A. P., Aktulga, H. M., Berger, R., Bolintineanu, D. S., Brown, W. M., Crozier, P. S., Veld, P. J. I., Kohlmeyer, A., Moore, S. G., Nguyen, T. D.; et al. (2022). LAMMPS-a flexible simulation tool for particle-based materials modeling at the atomic, meso, and continuum scales. Comput. Phys. Commun. 271. 108171. 10.1016/j.cpc.2021.108171.
- 14. Jurcik, A., Bednar, D., Byska, J., Marques, S. M., Furmanova, K., Daniel, L., Kokkonen, P., Brezovsky, J., Strnad, O., Stourac, J.; et al. (2018). CAVER Analyst 2.0: analysis and visualization of channels and tunnels in protein structures and molecular dynamics trajectories. Bioinformatics 34, 3586-3588. 10.1093/bioinformatics/bty386.
- 15. Meng, Z., Mirica, K. A. (2020). Two-dimensional d- π conjugated metal-organic framework based on hexahydroxytrinaphthylene. Nano Research 14, 369-375. 10.1007/s12274-020-2874-x.
- 16. Eagleton, A. M., Ambrogi, E. K., Miller, S. A., Vereshchuk, N., Mirica, K. A. (2023). Fiber Integrated Metal-Organic Frameworks as Functional Components in Smart Textiles. Angew. Chem. Int. Ed. Engl. 62, e202309078. 10.1002/anie.202309078.
- 17. Rubio-Gimenez, V., Galbiati, M., Castells-Gil, J., Almora-Barrios, N., Navarro-Sanchez, J., Escorcia-Ariza, G., Mattera, M., Arnold, T., Rawle, J., Tatay, S.; et al. (2018). Bottom-Up Fabrication of Semiconductive Metal-Organic Framework Ultrathin Films. Adv. Mater. 30. 10.1002/adma.201704291.
- 18. Park, J., Hinckley, A. C., Huang, Z., Feng, D., Yakovenko, A. A., Lee, M., Chen, S., Zou, X., Bao, Z. (2018). Synthetic Routes for a 2D Semiconductive Copper Hexahydroxybenzene Metal-Organic Framework. J. Am. Chem. Soc. 140, 14533-14537. 10.1021/jacs.8b06666.
- 19. Hmadeh, M., Lu, Z., Liu, Z., Gándara, F., Furukawa, H., Wan, S., Augustyn, V., Chang, R., Liao, L., Zhou, F.; et al. (2012). New Porous Crystals of Extended Metal-Catecholates. Chem. Mater. 24, 3511-3513. 10.1021/cm301194a.
- 20. Grant Glover, T., Peterson, G. W., Schindler, B. J., Britt, D., Yaghi, O. (2011). MOF-74 building unit has a direct impact on toxic gas adsorption. Chem. Eng. Sci. 66, 163-170. 10.1016/j.ces.2010.10.002.
- 21. DeCoste, J. B., Peterson, G. W. (2013). Preparation of hydrophobic metalorganic frameworks via plasma enhanced chemical vapor deposition of perfluoroalkanes for the removal of ammonia. J. Vis. Exp., e51175. 10.3791/51175.